Chemical Vapor Deposition of Permselective Oxide Membranes for Hydrogen Separation

Thesis by

Soojin Kim

In Partial Fulfillment of the Requirements

for the Degree of

Doctor of Philosophy

California Institute of Technology

Pasadena, California

1994

(Submitted December 8, 1993)

To my parents

Acknowledgements

I would like to thank my advisor, Professor George R. Gavalas for his guidance throughout the course of this work. His broad knowledge and creativity have provided me with much insight needed to carry out the work. His support and patience are deeply appreciated.

I am thankful to Dr. Suk Woo Nam for helping me to get started with experiments in the early stage of this work. I have had excellent co-workers, Dr. Theophilos Ioannides, Michael Tsapatsis, and Neil Fernandez who shared useful discussions and assistances. I also thank Ms. Donna Johnson for the typing, Mr. Chic Nakawatase for frequent assistance in setting up experimental apparatus, and Mr. Gabor Faludi for excellent glassblowing. I cannot thank enough Mr. Tom Dunn for finding an old part and fixing the TGA instrument at a critical moment.

I gratefully acknowledge the Department of Energy for financial support and Corning, Inc. for providing Vycor tubes.

Most importantly, I thank my parents for their constant support and encouragement. This thesis is dedicated to my parents. I am very fortunate to have the most loving husband. I thank him for his patience, understanding, and encouragement throughout the years. This work has been possible with God's grace.

Abstract

Membranes have recently emerged as energy-efficient means of gas separation. Oxide membranes that are effective for hydrogen separation at elevated temperatures (400–800°C) were developed. The membranes have high H_2 selectivities along with permeances that are comparable to those of conventional polymeric membranes operating at ambient temperature.

Hydrogen-permselective membranes were synthesized by chemical vapor deposition of SiO_2, TiO_2, Al_2O_3, and B_2O_3 layers within the pores of Vycor tubes. The deposition was carried out by continuous flow of $SiCl_4$, etc., and water in either the one-sided or the two-sided (opposing-reactants) geometry at 100–800°C. Permselective SiO_2 layers could be formed in both geometries, while deposition of TiO_2 and Al_2O_3 layers was achieved only in the two-sided geometry. The permeation coefficients at 450°C were 0.3 and 0.1 $\frac{cm^3(STP)}{min \cdot cm^2 \cdot atm}$ for SiO_2 membranes produced in the one-sided geometry and two-sided geometries, respectively. The H_2:N_2 permeation ratios were 500–5000. The TiO_2 and Al_2O_3 membranes had somewhat lower permeation coefficients and H_2:N_2 ratios.

The TiO_2 membranes prepared in the opposing-reactants geometry were characterized by scanning electron microscopy, electron microprobe analysis, and transmission electron microscopy. Examining tube cross section containing TiO_2 deposit revealed that the membrane consisted of a thin region (approximately 1 μm thick) of totally plugged pores and a broad region (100 μm) of partially filled pores. The spatial density distribution of TiO_2 in the tube cross section showed an asymmetric profile located close to the side of chloride flow indicating heterogeneous mechanism of the deposition reaction. The H_2 permeance of the

membranes decreased by 50–75%, and the selectivity diminished upon prolonged hydrothermal treatment.

A mechanism of the deposition process is suggested involving heterogeneous reactions of gaseous chloride and surface hydroxyl groups and of water vapor with surface chloride groups on the growing deposit layer. The mechanism and kinetics of SiO_2 deposition were investigated by thermogravimetric analysis. The reactions were decoupled by alternating reactions of $SiCl_4$ and H_2O with the surface of Vycor glass. The results are interpreted by postulating two types of silanol groups Si-OH on the Vycor surface, paired and isolated. Reaction of $SiCl_4$ with paired silanols proceeds by competing steps which control the total extent of silylation. Upon reaction with H_2O, all surface Si-Cl groups are hydrolyzed regenerating Si-OH. Simultaneous silanol-silanol and silanol-surface chloride condensations eliminate H_2O or HCl to form new Si-O-Si bridges with final product silica. A kinetic model incorporating the silylation, hydrolysis and condensation steps describes well the TGA data.

The reaction of the chlorosilanes with surface hydroxyls occurs very rapidly at temperatures above 600°C and causes significant axial concentration gradients in the one-sided deposition, resulting in nonuniform deposit layer along the length of the tube. A new technique that eliminated the axial concentration gradients was used to deposit thin SiO_2 layers on the surface of porous Vycor glass. Alternating vapor phase reaction with $SiCl_4$ and H_2O was used to prepare membranes having H_2 permeance of 0.3–0.4 $\frac{cm^3(STP)}{min \cdot cm^2 \cdot atm}$ and H_2:N_2 selectivity of 500–1000 at 600°C. The $SiCl_4$ dosage at each silylation cycle, the concentration of initial surface -OH groups, and the reaction temperature influence significantly the deposit layer thickness. The membranes were stable to long hydrothermal treatments

with the H_2 permeance decreasing by about 20% and the selectivity increasing to more than 2000. The membrane properties after hydrothermal treatment are superior to those of membranes prepared by one-sided (steady flow) deposition due to thinner and more uniform deposit layers. A simple model incorporating diffusion and surface reaction was used to study the effect of various parameters on the formation of the deposit layer.

TABLE OF CONTENTS

Acknowledgements iii

Abstract iv

Table of Contents vii

List of Tables xi

List of Figures xiii

Chapter I Introduction 1

1.1 Overview of Membrane Technology for Gas Separation 2

1.2 H_2 Separation via Membranes 4

1.3 Inorganic Membranes 7

1.4 Objectives 9

References 13

Chapter II Synthesis of Hydrogen Permselective SiO_2, TiO_2, Al_2O_3, and B_2O_3 Membranes from Chloride Precursors 21

Abstract 22

2.1 Introduction 23

2.2 Experimental Techniques 25

2.2.1 Materials 25

2.2.2 Apparatus 26

2.2.3 Pretreatment 26

2.2.4 Deposition 26

2.2.5 Permeation Rate Measurements 27

2.2.6 SEM and EMA 28

2.3 Results and Discussion 28
2.3.1 SiO_2 Deposition 28
2.3.2 TiO_2 Deposition 29
2.3.3 Al_2O_3 Deposition 31
2.3.4 B_2O_3 Deposition 31
2.3.5 SEM and EMA 32
2.3.6 Reaction Mechanism 34
2.4 Conclusions 37
Acknowledgement 38
References 39

Chapter III Characterization of TiO_2 Membranes 55
Abstract 56
3.1 Introduction 57
3.2 Experimental Techniques 58
3.2.1 Preparation of Membranes 58
3.2.2 SEM and EMA 58
3.2.3 TEM 58
3.3 Results and Discussion 59
3.3.1 Permeance and Selectivity 59
3.3.2 Density Profiles and Reaction Mechanism 59
3.3.3 Activation Energy 62
3.3.4 Heat Treatment 62
3.3.5 TEM 62
3.4 Conclusions 63
References 65

Chapter IV Kinetic Study of the Reactions of Chlorosilanes with Porous Vycor Glass 77

Abstract 78

4.1 Introduction 79

4.2 Experimental Techniques 81

4.3 Experimental Results and Discussion 81

4.4 Kinetic Model Description 85

4.4.1 Silylation 87

4.4.2 Purge following Silylation 89

4.4.3 Hydrolysis 89

4.4.4 Purge following Hydrolysis 90

4.5 Numerical Results and Discussion 90

4.6 Conclusions 94

Nomenclature 95

Acknowledgement 96

References 97

Chapter V Atomic Layering of Permselective SiO_2 Films, Characterization and Modeling 116

Abstract 117

5.1 Introduction 118

5.2 Experimental Techniques 121

5.3 Experimental Results and Discussion 123

5.4 Model Description 129

5.5 Transformation of Equations 132

5.6 Discussion of Numerical Results 136

5.7 Conclusions 139

Nomenclature 141

Acknowledgement 142

References 143

Appendix 146

Chapter VI Conclusions 167

List of Tables

Table 1.1: Comparison of membranes with PSA and cryogenic processing . . 18

Table 1.2: Common industrial processes using synthesis gas 19

Table 2.1: Conditions of deposition and permeation coefficients of SiO_2, Al_2O_3, TiO_2, and B_2O_3 membranes 41

Table 2.2: One-sided deposition experiments that did not result in pore plugging within 2 hour of reaction 42

Table 3.1: Permeation coefficients of N_2 and H_2 in TiO_2 membranes prepared at various temperature 66

Table 3.2: Activation energy of H_2 permeation in TiO_2 membranes 67

Table 3.3: Permeation coefficients of N_2 and H_2 in TiO_2 membranes before and after heat treatments 68

Table 4.1: Weight change in various parts of reaction cycle for sample pretreated at different temperatures 99

Table 4.2: Constants and parameters used in the model calculation 100

Table 5.1: Membrane permeance to H_2 and N_2 after deposition and after hydrothermal treatment 149

Table 5.2: (a)Permeance of membranes deposited on the inner surface before and after hydrothermal treatments 150
(b)Permeance of membranes produced by one-sided (simultaneous flow) deposition before and after hydrothermal treatments 151

Table 5.3: The permeances of deposit layers excluding the resistance of Vycor tube 152

Table 5.4: Activation energy for H_2 permeance of Membranes 3 and 4 before and after hydrothermal treatments 153

Table 5.5: Parameters used in the calculations 154

List of Figures

Figure 1.1: A schematic diagram of membrane tube reactor for H_2S decomposition 20

Figure 2.1: (a) Schematic of the reactor system for opposing-reactants deposition and (b) schematics of reactant inlet for one-sided deposition 43

Figure 2.2: Permeation rate coefficients at deposition temperatures for hydrogen (- - -) and nitrogen (—) versus time of deposition by $SiCl_4$ and H_2O reaction 44

Figure 2.3: Schematic of concentration profiles in opposing-reactant deposition 45

Figure 2.4: Arrhenius plots for H_2 and N_2 permeation coefficients of SiO_2 membranes 46

Figure 2.5: N_2 (□, ■) and H_2 (○, ●) permeation coefficients of TiO_2 membranes during deposition at 450°C (—) and 600°C (- - -) . . 47

Figure 2.6: Permeation rate coefficients measured during deposition of Al_2O_3 for H_2 (- - -) and N_2 (—) at 450°C (○), 700°C (△), and 800°C (□) 48

Figure 2.7: H_2 and N_2 permeation coefficients at 150°C during deposition of B_2O_3 in opposing-reactants geometry 49

Figure 2.8: H_2 permeability coefficients of a B_2O_3 membrane deposition at 150°C and annealed under dry N_2 at 400°C overnight (▪), 300°C (▫), and 150°C overnight (•) and exposed to laboratory air at room temperature for 23 days (◦) 50

Figure 2.9: (a) Scanning electron micrographs of tube cross sections containing TiO_2 deposited at 600°C, (b) at higher magnification, and (c) TiO_2 deposited at 450°C 51

Figure 2.10: (a) EMA line scan of tube cross sections containing TiO_2 layers deposited at 600°C, and (b) 450°C 53

Figure 2.11: EMA line scan of a tube cross section containing Al_2O_3 layer deposited at 800°C 54

Figure 3.1: Optical microscope image of a tube cross section containing TiO_2 layer on 3mm TEM sample holder 69

Figure 3.2: Spatial density profiles of deposit from EMA line scan of tube cross sections containing TiO_2 layers 70

Figure 3.3: EMA line scan of a tube cross section containing TiO_2 layer deposited at 200°C 71

Figure 3.4: Scanning electron micrographs of a tube cross sections containing TiO_2 deposited at 200°C 72

Figure 3.5: Transmission electron micrograph of a largely untreated

section of Vycor tube: (a) bright field image and (b) dark field image 73

Figure 3.6: Transmission electron micrograph of a tube section containing TiO_2 deposited at 600°C and subsequently annealed at 800°C. (a) bright field image, (b) dark field image, and (c) dark field image at higher magnification 74

Figure 3.7: Electron diffraction pattern of the TiO_2 rich area shown in Figure 3.6 and corresponding crystal indices of anatase TiO_2 . . . 76

Figure 4.1: Schematic diagram of TGA system 101

Figure 4.2: Weight of sample V600 during first reaction with 9% $SiCl_4$-N_2 at 600°C and subsequent purge at the same temperature 102

Figure 4.3: Weight of sample V600 prereacted as in Figure 2 during reaction with 7% H_2O-N_2 and subsequent purge at 600°C . . . 103

Figure 4.4: Weight of sample V600 during two cycles of reaction with 9% $SiCl_4$-N_2 at 600°C and subsequent purge with N_2, and hydrolysis with 7% H_2O-N_2 at the same temperature 104

Figure 4.5: Comparison of two silylation experiments of V600 at 600°C with 9% $SiCl_4$-N_2. A: 30 min continuous silylation and B: 1.5 min silylation followed by 15 min purge followed by 30 min silylation 105

Figure 4.6: Weight of V600 during 20 consecutive cycles of silylation, purge, hydrolysis, and purge of 600°C 106

Figure 4.7: Weight change of V600 for each of the 20 consecutive cycles of silylation (□) and hydrolysis (•) of 600°C 107

Figure 4.8: Kinetic model of the reaction network during silylation 108

Figure 4.9: Kinetic model of the reaction network during hydrolysis 109

Figure 4.10: Experimental data points and model calculation (solid curve) for silylation of V600 for 30 min at 450°C 110

Figure 4.11: Experimental data points and model calculations (solid curve) for silylation at 400°C (□), 450°C (○), and 500°C (△) and subsequent purge at the same temperature 111

Figure 4.12: Experimental data points and model calculations (solid curve) for hydrolysis of prereacted samples as specified in Figure 4.11 at 400°C (□), 450°C (○), and 500°C (△) and subsequent purge at the same temperature 112

Figure 4.13: Arrhenius plots and activation energy values of the rate constants, k_1, k_{H1}, and k_3 113

Figure 4.14: (a) Effectiveness factor and (b) normalized surface concentration calculations for silylation 114

Figure 4.15: (a) Effectiveness factor and (b) normalized surface concentration calculations for hydrolysis 115

Figure 5.1: Schematic diagram of the reactor system 155

Figure 5.2: Permeances of H_2 and N_2 versus cycle number at 700°C for $SiCl_4$ dosage of 0.62μmol/cm^2 for Membrane 1 (▲) and 0.33μmol/cm^2 for Membrane 2 (■) 156

Figure 5.3: Permeance of H_2 and N_2 versus cycle number for the reaction at 700°C (Membrane 3, •) and 800°C (Membrane 4, ◆) for $SiCl_4$ dosage of 0.28μmol/cm^2 per cycle 157

Figure 5.4: EMA linescan of a tube cross section containing TiO_2 layers deposited at 700°C using $TiCl_4$ dosage of 0.37μmol/cm^2 per cycle 158

Figure 5.5: Calculated deposit density profiles after each cycle of deposition at 700°C. The $SiCl_4$ dosage was 0.33μmol/cm^2 per cycle 159

Figure 5.6: Calculated bulk $SiCl_4$ concentration, C_g/C_{bo}, versus reaction time in selected cycles for $SiCl_4$ dosage of 0.33 μmol/cm^2 (—) and 0.62 μmol/cm^2 (- - -) 160

Figure 5.7: Calculated final deposit density profiles for different $SiCl_4$ dosages 161

Figure 5.8: Calculated permeance versus cumulative dosage of $SiCl_4$ 162

Figure 5.9: Calculated permeance versus cycle number for different $SiCl_4$ dosages (—) 163

Figure 5.10: Calculated permeance versus cycle number for $SiCl_4$ dosage of 0.33 μmol/cm^2 and for different pore size distributions . . . 164

Figure 5.11: Calculated deposit density profiles for various initial surface concentrations of -OH groups 165

Figure 5.12: Cross section of Vycor tube wall containing a deposit layer (a) on the outside surface and (b) on the inside surface 166

Chapter I

Introduction

1.1 Overview of Membrane Technology for Gas Separation

The process of separation, enrichment, and purification of a species from a gaseous mixture is an important field of chemical process industry. Cryogenics and pressure swing adsorption (PSA) techniques are some of the conventional methods of gas separation. Recently, membrane technology has emerged as a high potential alternative to the traditional gas separation techniques. Membranes generally consist of thin films or layers of material through which one component of a gas mixture can selectively pass or permeate. Industrial membrane application in liquid and liquid-solid phase separation has been actively developed for many years; however, due to the lack of adequate material that provide high permeability and selectivity for gases, gas separation membranes have had limited industrial applications. Recent advances in material technology led to developments of new membrane materials that have high potential for practical applications.

The major benefits of using membrane separation process as compared to the traditional techniques are lower costs and convenience. There has been a number of economic analyses by industry on the use of membranes in various separation processes [1–3]. Although economic comparison of a membrane process versus other methods would be different for each specific application, the membrane processes in general were shown to be more economical than conventional methods such as cryogenics and PSA; a membrane process would have lower energy consumption and require less space, capital cost and maintenance costs. As an example, a cost and performance comparison of membrane process versus PSA and cryogenics in hydrogen recovery from a refinery off-gas is presented in Table 1.1.

One of the major potential advantages of employing membrane system in gas

separation is that species can be separated at the same time they are produced without disturbing the reaction process. For this reason, interests in membrane reactor configuration have increased recently [4]. The membrane-reactor configuration combines reaction and separation processes in a single unit operation by making the reactor wall out of membrane. One example of such membrane-reactor configuration is shown in Figure 1.1. Simultaneous reaction and product separation achieved through a membrane-reactor wall can drastically improve the conversion of many equilibrium-limited reactions. In some cases, membranes can also be used to selectively add a compound to suppress undesirable side reactions, thereby increasing the yield of a desirable reaction. Because of the increased conversion at a given temperature, lower operating temperature would be required for the same conversion which in turn could provide improved thermal efficiency of the overall operation. Because of this and other advantages, the effort to develop effective membrane reactors has become more active recently; several reports on the concept and experiments of membrane reactors for various catalytic reactions—such as dehydrogenation of hydrocarbons, decomposition of H_2S, etc.—have been published [4–9].

In general, for a membrane to be used as an effective gas separating tool, it must possess the following properties: selectivity, permeance (flux), and stability. Selectivity, often represented as a permeance ratio of two gases, is the ability of the membrane to separate a given gas mixture into its components. Permeance, which is the rate at which separation takes place, of the membrane is also important for the material to be considered as an economical separator. Since permeance of a membrane determines the surface area requirement of a membrane for a given application, a high permeance translates to a high efficiency. Permeance of a

membrane is expressed as

$$K = \frac{J}{A\Delta P}$$

where J is a flux of the permeating gas, A is the area of a membrane, and ΔP is the difference in hydrostatic pressure, partial pressure, or other potential (driving force) across the membrane. In order to achieve high permeance through the membrane, the membrane must be made thin, because the gas flux through a membrane is inversely proportional to the thickness of the membrane. In addition, the membrane must have required mechanical strength to be used in a practical equipment. Lastly, in order for a membrane to be a reliable and economical separation tool, the performance of the membrane should remain stable under prolonged application.

Polymeric membranes have been developed for many years and are being used commercially for the separation of H_2, O_2, and CO_2 at ambient temperature. However, polymeric membranes are unstable at high temperatures, and effective membrane materials for gas separation at high temperatures are still largely undeveloped. Although the concept (and requirements) of membrane separation has well been established and the economics and benefits of membranes are very attractive, large-scale industrial applications of membranes in gas separation are still relatively limited due to the lack of effective membrane materials with high selectivity and permeability.

1.2 Hydrogen Separation via Membranes

Hydrogen is one of the most important gaseous raw materials in chemical and petrochemical industries. The major usage of industrial hydrogen is in petroleum refinery and ammonia and methanol production, accounting for approximately

96% of total industrial hydrogen consumption [10]. Hydrogen is also widely used in industrial processes such as chemical synthesis, metallurgical processing, semiconductor and electronic materials manufacturing, and edible oil hydrogenation [11].

There are several methods of producing hydrogen, including steam reforming of hydrocarbons, electrolysis of water, thermal dissociation of natural gas, partial oxidation of hydrocarbons, and recovery from coke-oven gas. The hydrocarbon steam reforming process, which is the most common method, involves catalytic reaction of steam and hydrocarbons at an elevated temperature to form a mixture of H_2, CO and CO_2. The carbon monoxide produced in the process is, in turn, processed through water shift converter to produce additional H_2 as shown below:

$$C_nH_m + nH_2O \rightarrow nCO + (m/2 + n)\ H_2 \qquad \text{—Reforming}$$

$$CO + H_2O \rightarrow CO_2 + H_2 \qquad \text{—Shift}$$

After the reaction, extensive purification steps are required to obtain pure hydrogen suitable for industrial applications. Conventional H_2 purification techniques involve multiple stages of CO_2 and H_2S removal by chemical reactions and solvent extraction. Subsequently, absorption/adsorption processes to remove H_2O, CH_4, C_2H_6, CO, Ar, N_2, etc., and a cryogenic process to remove the remaining hydrocarbons must follow [11].

Membrane separation could be a convenient and economical replacement for the complicated conventional purification stage mentioned above. A H_2 permselective membrane could effectively separate H_2 in a single process, bypassing all individual steps involved in removing other gaseous species one after another from the mixture. As a result, elimination of the multiple absorption/adsorption processes and cryogenic process could lead to lower capital cost, space requirements,

and energy consumption.

Furthermore, a H_2 permselective membrane could be directly incorporated into the hydrocarbon steam reformer or water gas shift converter. Reactor walls made of H_2 permselective membranes can selectively remove H_2 from the mixture of reactants and products continuously during a reaction. As a result, the yield of H_2 will increase drastically due to the shift in equilibrium point. This could lead to elimination of the separation process as well as the purification process in H_2 production.

Other chemical reactions applicable for membrane-reactor configuration with H_2 permselective membranes include dehydrogenation of hydrocarbons (e.g., isobutane to isobutene and cyclohexane to benzene), decomposition of H_2S, decomposition of H_2I, and electrolysis of water. Several research papers reported that the conversions in many of these reactions have increased significantly by the use of membrane-reactors [12–14].

Applications for H_2 permselective membrane-reactors are not limited to production of H_2. In some hydrogenation reactions, H_2 can be introduced to a reactor through a H_2 permselective membrane for a controlled feed. In this application, some undesirable side reactions can be suppressed by limiting direct introduction of H_2 in the feed, hence improving reaction yield [15].

Hydrogen permselective membranes can also be used to effectively control feed gas ratios of synthesis gas (H_2-CO) for production of various chemicals used in petrochemical and metallurgical processes. Synthesis gas mixture is produced by hydrocarbon-steam reforming reaction described above; their stoichiometry can be adjusted according to the process requirements by selectively removing hydrogen through a membrane [16]. Some of the most common processes using synthesis gas mixture and their ratios are listed in Table 1.2.

In many industrial processes that consume hydrogen, plant off-gases or purge streams contain a large amount of unreacted hydrogen along with N_2, Ar, CO, CO_2, and various hydrocarbons. Traditionally, these purge streams have simply been burned because separation of H_2 would be very expensive [1]. Hydrogen permselective membranes would provide an inexpensive means for recovering valuable H_2 from the purge streams to be recycled back to the plant, thereby enhancing the overall economics by reducing the cost of expensive H_2 feed. Membrane systems can be used to recover H_2 at low cost from the purge streams of ammonia production, methanol production, hydrogenation reactions, or hydrocracking in petroleum refinery [17–21]. In these applications, since the membrane system is used to increase the efficiency, there is little risk to the overall operation even in the case of membrane failure in the purge stream. The economics of using membrane separations in the aforementioned and other industrial processes have been evaluated by industrial researchers, and were shown to be highly promising [1,19].

1.3 Inorganic Membranes

In the chemical process industry, high operating temperature of various processes is prevalent. Incorporating a membrane system directly at high temperature can increase thermal efficiency of the overall process. In recovery of H_2 from ammonia purge gas, for example, being able to separate H_2 at the operating temperature of the ammonia synthesis and to return the recovered H_2 to the reactor would relate to a lower energy consumption. Most of the catalytic reactions mentioned earlier as examples of membrane reactor applications take place at high temperatures (several hundred °C).

In order to integrate a membrane separation mechanism within a high tem-

perature reaction, the membrane material must be thermally stable. Traditional organic polymer membranes have limited applications in chemical process industry due to their lack of thermal resistance. Development of inorganic membranes has gained interest mainly because of their inherent thermal stability [6,22,23]. Inorganic membranes offer a number of other advantages over organic polymer membranes; i.e., high resistance against corrosive chemicals and microbiological attacks, and ability to be steam sterilized or autoclaved [22].

Inorganic membranes can largely be classified as porous or nonporous membranes, each providing different separation mechanisms. Porous membranes separate gases on the basis of a difference in their molecular weights. At sufficiently low pressures or in small pores (that range in diameter from 10Å to 1000Å), the mean free path of the diffusing molecule can be comparable or greater than the pore size, and collisions between gas molecules are less frequent than collisions with the wall. The transport process in this limit is Knudsen diffusion; the molecular velocity ratio of two gases is inversely proportional to the square root of their molecular weights. Therefore, porous membranes provide acceptable selectivity only when two gases in a mixture have significant differences in molecular weights. Currently, sol-gel, slipcasting, phase separation/leaching, and anodic oxidation are being studied as possible methods for the synthesis of porous inorganic membranes for gas separation [24–26]. Commercial porous inorganic membranes are most commonly made of alumina, zirconia or glass and have pore sizes ranging from 40Å to 1000Å [22,27]. However, the industrial application of porous membranes in gas separation process is narrowly bounded due to the limited range of selectivity.

Nonporous membranes, on the other hand, contain no pores of microscopic dimensions and separate gases by a transport process that is a continuous dis-

placement of vacant or interstitial sites by mobile atoms [28]. Some of the most common nonporous membranes are Pd membrane for H_2 separation and dense zirconia membranes for O_2 ionic conduction [13,29]. In the case of H_2 selective Pd and Pd alloy membranes, H_2 permeates through the membranes in the form of atomic hydrogen [30]. Molecular sieve membranes, such as carbon molecular sieve and zeolite membranes, contain small openings (less than 10Å in diameter) as part of their molecular structure that can be used to separate gases by size exclusion [31–33].

1.4 Objectives

Amorphous oxide materials are known to be highly selective to H_2 and He on the basis of their natural solubility and diffusivity [34–36]. Various theories and models have been offered to explain the transport mechanism in amorphous materials [35,37]. Since amorphous materials have more flexible atomic networks than crystalline materials, the diffusion of gas molecules is relatively high. Amorphous silica, in particular, is composed of a continuous network of silicon-oxygen tetrahedra which contains interstices or vacancies surrounded by silicon and oxygen atoms [38]. The gas atoms or molecules dissolved in silica glass lodge in these interstices, and diffusion is created when the gas molecules jump from one interstice to another. Small molecules such as hydrogen, helium and neon can diffuse faster than larger molecules because they experience lower activation energy in moving from one interstitial site to another in the glass network. Because the diffusion process in amorphous oxide materials is activated, gas separation can be achieved only at high temperatures. Because of their inherent thermal stability and high resistance to corrosive chemicals, oxides are attractive membrane material for high

temperature separation. Dense oxide materials have not been previously investigated for gas separations. They have high selectivity of H_2 among other gases, but the absolute permeability is too low to have any practical use. In order to fabricate an effective membrane device from this material, an ultrathin oxide layer must be used.

A practical method to produce membrane devices from the oxide materials is by forming a composite structure, because ultrathin oxide layers need stronger porous support material to provide mechanical strength. The support material must be highly porous to minimize its flow resistance and must be relatively thick to protect the oxide layer. This two tiered composite structure retains favorable properties of porous and nonporous materials for gas separation; high selectivity of the nonporous film and high permeability and mechanical strength of the thicker porous support. This type of composite structure has been extensively used in polymeric membranes [39].

One of the most effective methods to produce ultrathin oxide film on the surface of porous substrate is chemical vapor deposition (CVD). CVD is widely used for thin film processing in electronic materials and optical devices [40,41]. CVD offers a number of advantages over liquid-phase techniques such as sol-gel. The vapor phase deposition can take place at high temperature ensuring thermal stability of the resulting films and requires no separate drying and calcination afterwards, during which pores and cracks are often generated by removal of solvent or condensation products [42,43]. Thus films produced by CVD are generally denser and more uniform than those prepared by liquid-phase techniques. Easy control of the film thickness by controlling the deposition rate is another advantage of CVD.

Thin oxide layers can be deposited on mesoporous support tubes by the CVD

method. SiO_2 and TiO_2 layers can be produced using the hydrolysis of the corresponding chlorides as follows:

$$SiCl_4 + 2H_2O \rightarrow SiO_2 + 4HCl$$

$$TiCl_4 + 2H_2O \rightarrow TiO_2 + 4HCl$$

The hydrolysis of chlorides at high temperature (600–800°C) produces films with uniform density and thermal stability. Reaction with H_2O increases the stability of the oxide films in the moist environments encountered in potential applications such as water gas shift reaction.

The objective of this research was to develop chemical processes to produce oxide membranes permselective to H_2 for high temperature applications. The work involves the following aspects:

- development of experimental techniques to synthesize H_2 permselective membranes using chemical vapor deposition of oxide films,
- membrane synthesis using different deposition conditions and study of the physical and chemical properties of the oxide layers,
- study of the mechanism and kinetics of the reactions involved in the oxide layer deposition, and
- continued modification of the reaction system to enhance the membrane properties for separation.

This thesis is organized in four sections. In the next chapter, the synthesis of oxide membranes from hydrolysis of chloride precursors is described. The deposition characteristics of the oxide layers and the permselective properties of membranes are described, and a brief discussion of the reaction mechanism is included. Chapter III contains detailed characterization of the resulting oxide layer, particularly TiO_2. Studies of deposition characteristics at different temperatures are presented.

Physical properties such as spatial distribution and location of the oxide deposit are studied by SEM and electron microprobe x-ray analysis. TEM is used to investigate the crystal structure of TiO_2 layers. Chapter IV contains a detailed study of the reaction mechanism and the kinetics of SiO_2 deposition on the surfaces of porous glass. Thermogravimetric analysis (TGA) is employed to study the rates of the elementary surface reactions. Kinetic models of the reactions are compared with the experimental data from TGA. The kinetic study can provide essential information about the reaction and transport rates in the CVD process and can facilitate continued modifications of the reactor system to produce more effective membranes. Chapter V describes the design of a new synthesis system that provided improved transport and reaction processes. A novel technique of atomic layering of SiO_2 by repeated alternation of silylation and hydrolysis on porous glass is described. The chapter includes permeation measurements, hydrothermal stability tests of the resulting membranes, and a simple model that simulates the layering process, involving reactant diffusion and surface reaction kinetics.

References

1. Spillman, R. W., "Economics of Gas Separation Membranes," *Chem. Eng. Prog.*, **85 (1)**, 41 (1989).

2. Schendel, R. L., "Using Membranes for the Separation of Acid Gases and Hydrocarbons," *Chem. Eng. Prog.*, **80 (5)**, 39 (1984).

3. Schendel, R. L., C. L. Mariz, and J. Y. Mak, "Is Permeation Competitive?," *Hydrocarb. Proc.*, **62 (8)**, 58 (1983).

4. Hwang, S. T. and K. Kammermeyer, *Membranes in Separations*, Wiley-Interscience, New York (1975).

5. Sun, Y. M. and S. J. Khang, "Catalytic Membrane for Simultaneous Chemical Reaction and Separation Applied to a Dehydrogenation Reaction," *Ind. Eng. Chem. Res.*, **27**, 1136 (1988).

6. Armor, J. N., "Catalysis with Permselective Inorganic Membranes," *Applied Catalysis*, **49**, 1 (1989).

7. Kameyama, T., M. Dokiya, M. Fujushige, H. Yokokawa, and K. Fukuda, "Possibility for Effective Production of Hydrogen from Hydrogen Sulfide by Means of a Porous Vycor Glass Membrane," *Ind. Eng. Chem. Fundam.*, **20**, 97 (1981).

8. Mohan, K. and R. Govind, "Analysis of Equilibrium Shift in Isothermal Reactors with a Permselective Wall," *AIChE J.*, **34**, 1493 (1988).

9. Raymont, M. E. D., "Make Hydrogen from Hydrogen Sulfide," *Hydrocarb. Process.*, **54 (7)**, 139 (1975).

10. Bassett, L. C. and R. S. Natarajan, "Hydrogen - Buy it or make it?," *Chem. Eng. Prog.*, **76 (3)**, 93 (1980).

11. Shreve, R. N. and J. A. Brink, *Chemical Process Industries*, p. 98, McGraw Hill, New York (1977).

12. Shinji, O., M. Misono, and Y. Yoneda, "The Dehydrogenation of Cyclohexane by the Use of a Porous-glass Reactor," *Bull. Chem. Soc. Jpn.*, **55**, 2760 (1982).

13. Itoh, N., "A Membrane Reactor Using Palladium," *AIChE J.*, **33**, 1576 (1987).

14. Fukuda, K., M. Dokiya, T. Kameyama, and Y. Kotera, "Catalytic Decomposition of Hydrogen Sulfide," *Ind. Eng. Chem. Fundam.*, **17**, 243 (1978).

15. Hsieh, H. P., "Inorganic Membrane Reactors," *Catal. Rev.*, **33**, 1 (1991).

16. Schell, W. J. and C. D. Houston, "Process Gas with Selective Membranes," *Hydrocarb. Process.*, **61 (9)**, 249 (1982).

17. Glazer, J. L., M. E. Schott, and L. A. Stapf, "Hydrocracking? Upgrade Recycle," *Hydrocarb. Process.*, **67 (10)**, 61 (1988).

18. Cooley, T. E. and W. L. Dethloff, "Field Test Show Membrane Processing Attractive," *Chem. Eng. Prog.*, **81 (10)**, 45 (1985).

19. Bollinger, W. A., S. P. Long, and T. Metzger, "Optimizing Hydrocracker Hydrogen," *Chem. Eng. Prog.*, **80 (5)**, 51 (1984).

20. Bollinger, W. A., D. L. MacLean, and R. S. Narayan, "Separation System for Oil Refining and Production," *Chem. Eng. Prog.*, **78 (10)**, 27 (1982).

21. MacLean, L. I., C. E. Prince, and Y. C. Chae, "Energy-Saving Modifications in Ammonia Plants," *Chem. Eng. Prog.*, **76 (3)**, 98 (1980).

22. Hsieh, H. P., "Inorganic Membranes," *AIChE Symp. Ser.*, **84**, 1 (1988).

23. Goldsmith, R. L., "Special Issue on Ceramic Membranes," *J. Membr. Sci.*, **39**, 197 (1988).

24. Klein, L. C. and D. Gallagher, "Pore Structures of Sol-gel Silica Membranes," *J. Membr. Sci.*, **39**, 213 (1988).

25. Asada, S. L. and L. Dinh Du, "Separation of Alcohol/Water Gaseous Mixtures by Thin Ceramic Membrane," *J. Chem. Eng. Jpn.*, **19**, 72 (1986).

26. Rai, K. N. and E. Ruckenstein, "Alumina Substrates with Cylindrical Parallel Pores," *J. Catalysis*, **40**, 117 (1975).

27. Elmer, T. H., "Porous and Reconstructed Glass," *Ceramic and Glasses*, p. 427, Vol. 4, Engineered Materials Handbook, ASM International, Materials Park, Ohio (1992)

28. Borg, R. J. and G. J. Dienes, *An Introduction to Solid State Diffusion*, p. 53,

Academic Press Inc. (1988).

29. Cales, B. and J. F. Baumard, "Oxygen Semipermeability and Electronic Conductivity in Calcia-Stabilized Zirconia," *J. Material Sci.*, **17 (11)**, 3243 (1982).

30. Gryaznov, V. M., M. M. Ermilova, L. S. Morozova, N. V. Orekhova, V. P. Polyakova, N. R. Roshan, E. M. Savitsky, N. I. Parfenova, "Palladium Alloys as Hydrogen Permeable Catalysts in Hydrogenation and Dehydrogenation Reactions," *J. Less Common Metals*, **89 (2)**, 529 (1983).

31. Koresh, J. E. and A. Soffer, "Molecular Sieve Carbon Permselective Membrane. Part I. Presentation of a New Device for Gas Mixture Separation," *Sep. Sci. Technol.*, **18**, 723 (1983).

32. Bird, A. J. and D. L. Trimm, "Carbon Molecular Sieves Used in Gas Separation Membranes," *Carbon*, **21**, 177 (1983).

33. Suzuki, H., "Composite Membrane Having a Surface Layer of an Ultrathin Film of Cage-Shaped Zeolite and Processes for Production Thereof," *U. S. Patent* 4,699,892. (1987).

34. Boyd, D. C. and D. A. Thompson, "Glass," *Kirk-Othmer Encycl. Chem. Technol.* 3rd ed., Vol. 11, p. 807, John Wiley, New York (1980).

35. Shelby, J. E., Molecular Solubility and Diffusion, *Treatise of Materials Science and Technology* Vol. 17, Academic Press, New York (1979).

36. Altemose, V. O., "Permeation of Gases in Glass," *Seventh Symposium on the Art of Glassblowing*, The American Scientific Glassblowers Society, Wilmington, Del. (1962).

37. Doremus, R. H., *Modern Aspects of the Vitreous State*, p. 1, Butterworth & Co. (1962).

38. Willey, J. D., "Silica," *Kirk-Othmer Encycl. Chem. Technol.* 3rd ed., Vol. 20, p. 749, John Wiley, New York (1980).

39. Matson, S. L., J. Lopez, and J. A. Quinn, "Separation of Gases with Synthetic Membranes," *Chem. Eng. Sci.*, **38 (4)**, 503 (1983).

40. Kern, W. and R. C. Heim, "Chemical Vapor Deposition of Silicate Glasses for Use with Silicon Devices," *J. Electrochem. Soc.*, **117 (4)**, 568 (1970).

41. Pliskin, W. A., "Comparison of Properties of Dielectric Films Deposited by Various Methods," *J. Vac. Sci. Technol.*, **14 (5)**, 1064 (1977).

42. Brinker, C. J., "Structure of Sol-Gel-Derived Glasses," *Glass Science and Technology* Vol. 4A, p. 169, Academic Press, New York (1990).

43. Yoldas, B. E., "Alumina Gels that Form Porous Transparent Al_2O_3," *J. Mat. Sci.*, **10**, 1856 (1975).

Table 1.1 Cost comparison of membrane with PSA and cryogenic processing (hydrogen recovery from refinery off gas).[1]

	Membrane	PSA	Cryogenic
Hydrogen Recovery (%)	91	73	90
Recovery H2 Purity (%)	96	98	96
Product Gas Flow Rate (10^6 ft^3/day)	2.86	2.24	2.86
Power requirement (kW)	220	370	390
Steam requirement (kg/h)	400	-	60
Cooling Water requirement (t/h)	38	64	79
Capital Investment (Millions $)	0.91	2.03	2.66
Installation Area (ft^2)	52	651	1292

[1]Slightly modified version of a table from [1].

Table 1.2 Common industrial processes using synthesis gas[1]

	Volume ratios	
	H_2	CO
Methanol	2	1
Fischer-Tropsch	2	1
Oxo	1	1

[1]Slightly modified version of a table from [11].

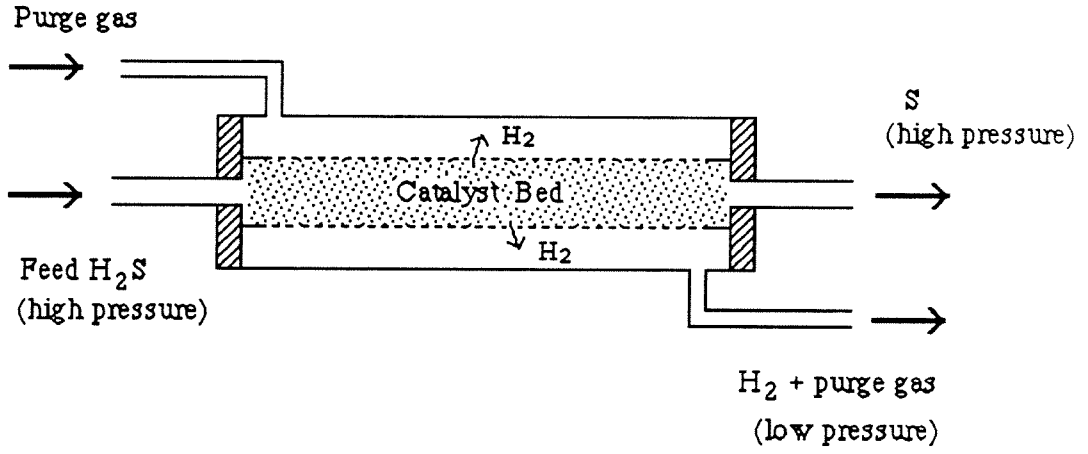

Figure 1.1 A schematic diagram of membrane tube reactor for H_2S decomposition.

Chapter II

Synthesis of Hydrogen Permselective SiO_2, TiO_2, Al_2O_3, and B_2O_3 Membranes from Chloride Precursors

Published in *I&EC Research*, **30**, 2152 (1991).

Abstract

Hydrogen-permselective membranes were synthesized by chemical vapor deposition of SiO_2, TiO_2, Al_2O_3, and B_2O_3 layers within the pores of Vycor tubes. The deposition involved reaction of $SiCl_4$, etc., with water at 100–800°C depending on the chloride and the reaction geometry. Permselective SiO_2 layers could be formed in either the one-sided or the two-sided (opposing-reactants) geometry, while deposition of TiO_2 and Al_2O_3 layers was achieved only in the two-sided geometry. The permeation coefficients at 450°C were 0.3 and 0.1 cm^3(STP)/(min·cm^2· atm) for SiO_2 membranes produced in the one-sided geometry and two-sided geometries, respectively. The H_2:N_2permeation ratios were 1000–5000. The TiO_2 and Al_2O_3 membranes had somewhat lower permeation coefficients and H_2:N_2 ratios. The membranes were characterized by scanning electron microscopy and electron microprobe analysis. A reaction mechanism is suggested involving heterogeneous reactions of chloride and water molecules with hydroxyl and chloride groups in the growing deposit layer.

2.1 Introduction

Inorganic membranes have recently attracted interest for use to high temperature gas separations coupled with reaction in a "membrane-reactor" configuration. The close coupling of reaction and product separation can greatly increase the yield or selectivity of equilibrium-limited reactions. Several classes of materials have attractive separation properties and have been investigated as membrane materials. Amorphous oxides such as SiO_2, B_2O_3, and GeO_2 have been known to be highly selective for permeation of helium and hydrogen [1–3]. But the absolute permeability of these oxides is low, therefore, a membrane would have to consist of a thin film of the selective oxide supported on a highly permeable material, preferably a slender tube or capillary.

During the last few years we have been developing hydrogen permselective membranes by chemical vapor deposition of an amorphous oxide layer within the walls of porous Vycor tubes, the latter serving as the support element. The amorphous oxides that we have worked with are SiO_2, TiO_2, Al_2O_3, and B_2O_3. Originally we carried out deposition of SiO_2 using silane oxidation

$$SiH_4 + O_2 \rightarrow SiO_2 + 2H_2 \quad (1)$$

In our most recent work we have used chloride hydrolysis to deposit SiO_2 and other oxides:

$$SiCl_4 + 2H_2O \rightarrow SiO_2 + 4HCl \quad (2)$$

$$TiCl_4 + 2H_2O \rightarrow TiO_2 + 4HCl \quad (3)$$

$$2AlCl_3 + 3H_2O \rightarrow 2Al_2O_3 + 6HCl \quad (4)$$

$$2BCl_3 + 3H_2O \rightarrow 2B_2O_3 + 6HCl \quad (5)$$

Our initial experiments employed low pressure silane (SiH_4) oxidation to deposit films on porous Vycor tubes. The films produced under these standard CVD conditions were porous, consisting of partially fused SiO_2 particles 0.5–1 μm in diameter. After one hour of deposition there was no measurable change in the permeation rates of H_2 or N_2, and no change was observed by sintering at 800°C. Sintering of the porous film at temperatures above 800°C was not attempted, for along with the porosity of the deposited film it would have eliminated the porosity of the Vycor support.

At that point we changed the reaction geometry introducing the two reactants, at ordinary pressures, from opposite sides of the tube wall. The reactants diffuse towards each other and react within the porous matrix. Once the pores are plugged, the reaction ceases and the resulting nonporous layer, imbedded within the porous wall, constitutes the H_2 permselective barrier. The results of our work with SiH_4 oxidation have been reported [4–6].

The temperature of 450°C used in the opposing-reactants oxidation of silane could not be varied significantly without adversely affecting the nature of deposition. If the temperature was decreased below 400°C, the reaction rate became too low, producing a thick film with low permeation rates. At temperatures above 500°C, pyrolysis of silane to elemental silicon became significant plugging the pores of the support tube over a broad region and eliminating the permeability altogether. When the films produced at 450°C were subjected to higher temperatures, e.g., 600°C, especially in the presence of water vapor, they suffered densification accompanied by decrease of permeation rates and sometimes decrease of selectivity as well. However, when the film deposition had taken place with water vapor added to the silane and oxygen reactants, subsequent thermal exposure to higher temperatures and water vapor caused a decrease of permeability but left

the selectivity unchanged.

If deposition could be carried out at higher temperatures, e.g., 700°C, the film produced would be denser and, therefore, more stable to temperatures at least as high as 600°C, at which the films produced by silane oxidation suffered significant densification. The reaction between $SiCl_4$ and H_2O is suitable for this purpose. The chloride is also safe from the standpoint of explosion, but is highly corrosive in the presence of humidity. In this paper we report our membrane synthesis work using the hydrolysis of $SiCl_4$, $TiCl_4$, $AlCl_3$, and BCl_3.

Our experiments with $SiCl_4$ hydrolysis have shown that one-sided deposition and opposing-reactants deposition are both suitable for the formation of permselective layers. In fact, one-sided deposition produces thinner layers having higher permeation rates. However, permselective layers of TiO_2 and Al_2O_3 could only be made by opposing-reactants deposition.

The purpose of this paper is to present experimental results on the formation of SiO_2, TiO_2, Al_2O_3, and B_2O_3 layers by the hydrolysis of the respective chlorides and discuss qualitatively the structure of these layers and the differences between the opposing-reactants and the one-sided deposition.

2.2 Experimental Techniques

2.2.1 Materials

Porous Vycor (Code 7930) tubes of 5 mm outside diameter, 1.1 mm wall thickness, 0.28 void fraction, and 40 Å mean pore diameter were supplied by Corning, Inc. Nonporous quartz tubes were welded from either side of a 30 cm long porous Vycor tube to permit connection with metal fittings as shown in Figure 2.1.

Silicon tetrachloride (99.999%, Aldrich Chemical Co.), aluminum chloride (99.99%, Aldrich Chemical Co.), Boron trichloride (Matheson) and titanium chloride (99.9%, Aldrich Chemical Co.) were used throughout these studies. High purity N_2, O_2, H_2 gas supplied by Matheson were further purified by Alltech gas purifiers.

2.2.2 Apparatus

A schematic diagram of the apparatus for deposition and permeation rate measurement is shown in Figures 2.1a and 2.1b. The reactor, placed in a furnace, consists of a porous Vycor tube (substrate) concentric to an outer nonporous quartz tube of 12 mm inner diameter.

2.2.3 Pretreatment

Before reaction the tubes were heated at 100°C and 200°C under N_2 flow to remove adsorbed water and then at 600°C under oxygen flow for several hours in order to remove any adsorbed organic impurities.

2.2.4 Deposition

The reactants (liquid chloride and water) were introduced into the reactor, either separately to the inner and annulus region of the reactor for opposing-reactants deposition or both into the inner region for one-sided reactant deposition. In either case the reactants were carried by N_2 streams flowing through bubblers with a constant flowrate of 50 cm^3/min. For Al_2O_3 depositions, an $AlCl_3$ sublimator was used in place of the chloride bubbler.

The concentrations of the reactants were controlled by adjusting their vapor pressures by regulating the temperatures of the bubblers. Because the flowrates

of the N_2 streams through the bubbler were low, it was assumed that the carrier gases was in each case saturated with the reactants.

For B_2O_3 depositions a BCl_3 lecture bottle was used and the gaseous chloride stream was diluted with N_2 to the desired concentration.

The reaction took place at atmospheric pressure. A series of 10 to 15 minutes reactions each followed by purging with N_2 and permeation rate measurements was carried out for each experiment.

Typical concentrations used throughout this study for the opposing-reactants geometry were around 10% chloride in N_2 and 10% water in N_2. For one-sided depositions, concentrations were varied from 1 to 10%. Exact values are given later for each experiment.

2.2.5 Permeation Rate Measurements

The permeation rates to various gases were determined by a bubble flowmeter while the pressure difference between the compartments separated by the membrane was maintained at 30 psia. Permeation rates below the limit which can be measured by the bubble flowmeter were measured using a mass spectrometer and a sensitive pressure transducer connected to a computer. In the latter case, the inside of the membrane was maintained at 2 atm under flow while the outer annulus was initially evacuated. The annulus was then isolated from vacuum and its transient pressure measured by the pressure transducer or the mass spectrometer. The permeation rate coefficient was then determined from the following equations, assuming the validity of ideal gas law:

$$Q[\mathrm{cm}^3(\mathrm{STP})/(\mathrm{min}\cdot\ \mathrm{cm}^2\cdot\ \mathrm{atm})] = \frac{(dV/dt)}{A\Delta p}$$

$$dV/dt = K dp/dt$$

where A is the surface area of the membrane, Δp is the pressure difference across the membrane, dp/dt the pressure rise in the annulus, and K is the calibration factor established between the pressure transducer and the bubble flowmeter.

2.2.6 Scanning Electron Microscopy and Electron Microprobe Analysis

Scanning electron microscopy (SEM) was conducted using a *CamScan* electron microscope operating at 20 kV and with resolution of 500 Å. The samples were prepared by first casting small sections of the Vycor tube containing the deposited oxide and then polishing and coating with carbon or gold. Because of difficulties in sample preparation it was not attempted to use the instrument at its highest resolution. The cross section of the tube was also examined by a *JEOL 733 Superprobe* electron microprobe by wavelength dispersive spectroscopy.

2.3 Results and Discussion

2.3.1 SiO_2 Deposition

Table 2.1 presents deposition conditions and final permeation properties for several oxide membranes. Concentrating for the moment on the SiO_2 membranes we note that the membranes produced by one-sided deposition have significantly higher permeation coefficients than those produced in the opposing-reactants geometry. Opposing-reactants deposition at 600°C for as many as 5 hours was not sufficient for complete pore plugging and useful results were obtained only at 700 and 800°C. Figure 2.2a shows the evolution of H_2 and N_2 permeation rates during deposition at 700 and 800°C in the opposing-reactants geometry. At 700°C essentially complete pore plugging is attained within 3 hours, although continuing deposition after that time leads to further reduction in the permeation rates,

especially that of N_2, evidently due to densification and, possibly, slow thickening of the already formed layer. At 800°C the reaction is faster requiring about 1–1.5 hours for complete pore plugging. In one-sided deposition, by contrast, at 600°C pore plugging is complete in less than 10 minutes, and even at 400°C pore plugging takes less than 90 minutes. Figure 2.2b shows the evolution of H_2 and N_2 permeation rates during one-sided deposition at 600°C and 400°C.

The sharply different rates of the one-sided and opposing-reactants deposition is due to the different level of reactant concentrations at the location of maximum deposition rate. In one-sided deposition, pore plugging occurs at or near the external surface where the reactant concentrations are near their free-stream values. In the opposing reactant deposition the reactant concentrations at the location of maximum rate are small fractions of their boundary values as shown schematically in Figure 2.3. The faster the reaction, the lower these concentrations and, hence, the larger the difference between the one-sided and the opposing-reactants geometries.

Permeation rates of H_2 and N_2 through a SiO_2 film deposited at 800°C were measured at 450, 600, and 800°C, and the measurements plotted on an Arrhenius diagram (Figure 2.4) yielded activation energies of 37 kJ/mol for H_2 and 60 kJ/mol for N_2. In earlier experiments with SiO_2 films produced by silane oxidation we found that the activation energy for hydrogen permeation depends on the thermal history of the material, being as low as 6 kJ/mol for fresh films deposited in the absence of water vapor. The value of 37 kJ/mol for the film deposited at 800°C is very close to that measured for fused quartz [7].

2.3.2 TiO_2 Deposition

Table 2.1 includes several experiments of TiO_2 deposition and the perme-

ation properties of the resulting films. The evolution of hydrogen and nitrogen permeation rates during TiO_2 deposition at 450 and 600°C is shown in Figure 2.5. Note that the permeation rates were measured at the temperature of deposition. These rates are only slightly lower than those of the SiO_2 films produced in the opposing-reactants geometry. The H_2:N_2 permeation ratio varies from 200 to 1500 depending on the deposition time and temperature.

The TiO_2 films deposited at 800°C had much lower permeability and H_2:N_2 ratios. It is well known that in CVD of TiO_2 the deposition temperature strongly affects the crystallinity of the oxide deposited. There is also evidence from previous work that in TiO_2 supported on SiO_2 the transition from the amorphous phase to anatase and the transition from anatase to rutile occurs at much higher temperatures than in the case of bulk TiO_2. Reichmann and Bell [8] have found such evidence in their investigation of the chemistry by which small crystallites of TiO_2 are produced on a silica support. They reported that although there is no chemical interaction between TiO_2 and SiO_2, the silica support stabilizes the amorphous TiO_2 with respect to the phase transformation to anatase up to a calcination temperature above 550°C, whereas bulk material is converted to anatase well below that temperature. They also found that the transition temperature from anatase to rutile is much higher in the presence of the silica support. There is no previous literature on the permeation of H_2 and N_2 through TiO_2, but it is reasonable to assume that the amorphous oxide is more permeable than the crystalline material. The permeation measurements listed in Table 2.1 suggest that at some temperature between 600 and 800°C the deposited TiO_2 becomes crystalline resulting in lower hydrogen permeation. This possibility is consistent with some recent transmission electron microscopy observations we made on a TiO_2 layer deposited at 600°C and subsequently heated at 800°C. The diffraction

pattern of that layer was characteristic of the anatase structure.

The TiO_2 films listed in Table 2.1 and Figure 2.5 were all obtained in the opposing-reactants geometry. Deposition experiments were also carried out in the one-sided mode under the conditions listed in Table 2.2. None of these experiments resulted in a significant reduction of the N_2 or H_2 permeation, therefore, none produced a dense layer plugging the Vycor pores. The difference between SiO_2 and TiO_2 deposition is discussed in the section on deposition mechanism.

2.3.3 Al_2O_3 Deposition

Al_2O_3 films were deposited by means of $AlCl_3$ hydrolysis, reaction (3) in the opposing-reactants geometry. Depositions were carried out at 450, 700, and 800°C. The results are shown in Figure 2.6 and Table 2.1. As shown in Table 2.1, the permeation rate of hydrogen at 450°C of Al_2O_3 films deposited at 700 and 800°C is substantially below that of the SiO_2 films. The H_2:N_2 permeation ratio was at most 400, also lower than that of SiO_2. The best results were obtained for films deposited at 450°C and densified by annealing at 700°C. In these films the H_2:N_2 permeation ratio increased to 1000, but the permeation coefficient of hydrogen remained lower than that of SiO_2 films. A few experiments, listed in Table 2.2, conducted in one-sided geometry did not produce pore plugging.

2.3.4 B_2O_3 Deposition

B_2O_3 films were deposited by means of BCl_3 hydrolysis, reaction (2). It was found that the hydrolysis reaction takes place over a wide temperature range (50–800°C). However, the Vycor tubes containing B_2O_3 layers deposited or annealed at temperatures above 500°C have small H_2 permeation coefficients, smaller than 0.01 $cm^3(STP)/(min \cdot cm^2 \cdot atm)$ at 800°C. Films deposited between 100–450°C

have hydrogen permeation coefficients as high as 0.2 $cm^3(STP)/(min \cdot cm^2 \cdot atm)$ at 450°C and 0.03 $cm^3(STP)/(min \cdot cm^2 \cdot atm)$ at 150°C. At the latter temperature the hydrogen permeation through SiO_2 layers was negligible. Unfortunately, the permeation coefficients of the boria membranes decreased significantly upon heating these membranes at temperatures of 500°C or higher. Figure 2.7 shows the evolution of H_2 and N_2 permeation rates during B_2O_3 deposition at 150°C. When the B_2O_3 films were exposed to laboratory humid air for several weeks, they developed boric acid whiskers and subsequently cracked due to interaction of water with B_2O_3. Figure 2.8 shows the effect of densification due to the heat treatment of a film deposited at 150°C, as well as the dramatic increase in permeability after exposure to humid air for 23 days.

2.3.5 Scanning Electron Microscopy and Electron Microprobe Analysis

Scanning electron microscopy (SEM) of several sectioned tubes that had been treated by SiO_2 deposition did not give any indication of the deposited SiO_2 layer. Since the porous Vycor substrate is >96% SiO_2, and the deposited material pure SiO_2, the only effect of deposition is to increase the SiO_2 density by about 28% (the void fraction) at the region of complete pore plugging which could be less than 1 μm wide. A smaller increase in density would be distributed over a wider region of partial pore plugging. Evidently these differences are not discernible by SEM.

SEM and electron microprobe analysis (EMA) of tubes subjected to TiO_2 deposition gave clear indication of the location and width of the region of TiO_2 deposition. Figure 2.9a shows a typical electron backscattering micrograph of a polished cross section of a Vycor tube bearing an internal TiO_2 layer deposited at 600°C. The large fissure near the lower left is a crack generated by the cutting

or polishing. The TiO_2 deposit is the band of lines about 100 μm below the top which in this case is the inside of the tube. The band is about 30–40 μm thick and consists of a series of parallel lines. Figure 2.9b shows the TiO_2 band at higher magnification. Figure 2.9c shows a polished cross section of a Vycor tube carrying a TiO_2 layer deposited at 450°C. The layer in the middle is again about 100 μm from the internal tube surface at the bottom. This TiO_2 layer shows the same kind of uniformly striated structure observed for the film deposited at 600°C. At this time we have no explanation for the striation in the TiO_2 layer.

The scanning electron microscopy was supplemented by measurements of the elemental composition profile across the polished tube section shown in Figure 2.9 by electron probe microanalysis. Figure 2.10a and b show the relative density profiles of TiO_2 for the 600°C and 450°C deposition respectively. The main features of these figures is the gradual rise of the TiO_2 profile from the side of the $TiCl_4$ flow (inside of Vycor tube) and steep decline towards the side of the H_2O. Significant TiO_2 is present over about 100 μm region although the region of totally plugged pores is much thinner as evidenced by the sharp maximum in the profile. The profiles in Figure 2.10a and b do not show the striated structure of the TiO_2 layer, probably because of the lower resolution of EMA compared to that of SEM.

The SEM and EMA results show several unexpected features. First there is the location of the deposition region. The concentration of the reactants $TiCl_4$ and H_2O were chosen inversely proportional to their Knudsen diffusion coefficients, so that the reaction region may be located exactly at the midpoint of the tube wall, according to a simple model of diffusion limited reaction. Instead the reaction region was much closer to the $TiCl_4$ side. The same trend was observed for the Al_2O_3 films as shown in the Al/Si ratio profile given in Figure 2.11. A second unexpected feature is the asymmetric nature of Al and Ti profiles. In the case of

the TiO_2 films, one can also notice in the SEM micrographs the difference in the texture of the regions separated by the striation. The region extending from the $TiCl_4$ side to the location of the maximum deposit density is smooth, whereas at the opposite side of the layer the texture seems granular. As shown in the EMA profile, the smooth region is coated with TiO_2 all the way from the inside of the tube to the peak of the deposited layer.

2.3.6 Reaction Mechanism

The brief discussion that follows deals with some general features of the reaction mechanism and not with the detailed chemical mechanism which is outside the scope of this work and should be approached by different type of experiments. The main question addressed here is whether deposition occurs via a homogeneous precursor or is strictly heterogeneous. In the first case the gas-phase reaction between chloride and water molecules would produce oligomer molecules, or particles, which could then form a layer on the pore surface. In the second case the chloride molecule and water would react directly with sites on the solid surface. We shall consider the reactions of $SiCl_4$ and $TiCl_4$ separately, for as we have seen these two reactions have shown qualitatively different trends, especially in one-sided deposition.

There is a significant body of work concerning the reactions of gaseous $SiCl_4$ and other chlorosilanes with the surface hydroxyl groups of silica gels. Reaction of $SiCl_4$ or $Si(CH_3)_3Cl$ with isolated silica surface hydroxyl groups takes place with elimination of HCl to form a Si-O-Si bond, and at 280°C this reaction was complete within one hour [9]. Hydrogen bonded -OH groups on the other hand reacted much more slowly. When the surface treated by the chloride was exposed to water vapor at the reaction temperature, the -OH groups reappeared, i.e., the

Si-Cl groups hydrolyzed to Si-OH and HCl. Simultaneously with these reactions between $SiCl_4$ or H_2O in the gas and -OH and -Cl groups in the solid, condensation reactions between two -OH groups or a -OH and a -Cl group in the solid result in cross linking by formation of siloxane bonds. Thus exposure of the silica surface to a gaseous mixture containing $SiCl_4$ and H_2O at temperatures above 250°C is expected to result in the growth of a partially hydroxylated SiO_2 layer by the reactions:

$$\text{Si-OH} + SiCl_4 \rightarrow \text{Si-O-}SiCl_3 + \text{HCl}$$

$$\text{Si-Cl} + H_2O \rightarrow \text{Si-OH} + \text{HCl}$$

$$\text{Si-OH} + \text{Si-OH} \rightarrow \text{Si-O-Si} + H_2O$$

$$\text{Si-Cl} + \text{Si-OH} \rightarrow \text{Si-O-Si} + \text{HCl}$$

In contrast to the reaction of gaseous $SiCl_4$ with surface hydroxyl groups, the gas-phase reaction between $SiCl_4$ and H_2O at temperatures below 900°C is virtually uncharted territory. We know only one report [10] of kinetic experiments of gas-phase hydrolysis of $SiCl_4$, $TiCl_4$ and $SnCl_4$.

Titanium oxide deposition was shown earlier to have features distinct from those of SiO_2. In the opposing-reactants geometry, TiO_2 deposition is much faster, at 450°C requiring about 30 minutes for complete pore plugging compared to the 60 minutes required for pore plugging by SiO_2 at 800°C. However, in one-sided deposition, pore plugging by TiO_2 was not achieved. The literature provides some interesting information about the reactions of $TiCl_4$ with hydroxylated surfaces. Armistead et al. [11] found that $TiCl_4$ vapors react with surface hydroxyls of silica gel at room temperature to give Si-O-$TiCl_3$ and $(Si\text{-}O)_2$ $TiCl_2$ groups. Hair and Hertl [12] found that gaseous $TiCl_4$ reacts with hydroxyl groups on silica gel very rapidly even at room temperature. Tolmachev and Okatov [13] passed

alternatively $TiCl_4$ and H_2O over a powder of Vycor glass at 180 °C and observed a layer by layer growth of titanium oxide. Evidently the Ti-Cl groups hydrolyze to Ti-OH, which can once more react with $TiCl_4$. These reactions were not examined in the temperature range relevant to our experiments, 400–600°C, but the direct heterogeneous mechanism remains plausible for the opposing-reactants deposition.

The failure to achieve pore plugging in one-sided deposition of TiO_2 is rather puzzling. However, a tentative explanation can be found in the relatively high rate of the homogeneous reaction. The gas-phase reaction between $TiCl_4$ and H_2O is known to be much faster than the analogous reaction of $SiCl_4$ [10]. In the opposing-reactants geometry the heterogeneous mechanism is dominant because of the high surface area and the low concentration of reactants. Any oligomers formed homogeneously would diffuse away from the reaction zone rather slowly and would more likely become trapped by the surface contributing to the overall growth of the deposit layer. In one-sided deposition, however, the homogeneous reaction depletes the reactants thus suppressing the direct heterogeneous reactions. At the same time the oligomers and particles formed in the gas phase have relatively low diffusion coefficients and are much more likely to be advected away from the reaction zone than to diffuse and become attached on the internal surface.

The deposition of Al_2O_3 layers followed a pattern similar to that of TiO_2. The opposing-reactants geometry yielded complete pore plugging at temperatures as low as 450°C, but in one-sided deposition complete pore plugging was not achieved, at least in the experiments listed in Table 2.2. The same considerations regarding reaction mechanisms as in the TiO_2 case apply here too, since $AlCl_3$ is known to react rapidly with water in the gas phase [14]. Deposition of B_2O_3 has some distinct features. One is the high reactivity of BCl_3 with surface hydroxyls, the reaction proceeding even at room temperature [12]. Another is the ease of

hydrolysis of B_2O_3 to boric acid which may explain the formation of whiskers and cracks upon prolonged exposure to laboratory air.

2.4 Conclusions

Hydrogen permeable membranes were synthesized by depositing layers of amorphous SiO_2, TiO_2, Al_2O_3 and B_2O_3 within the pores of Vycor tubes using the reaction of the respective chloride vapors ($SiCl_4$, etc.) with water vapor. The membranes obtained by SiO_2 deposition have permeation coefficients of 0.1–0.3 $cm^3(STP)/(min \cdot cm^2 \cdot atm)$ and H_2:N_2 permeation ratios of 3000–5000 at 450°C. These permeation coefficients include the resistance of the Vycor tube wall as well as the resistance of the deposited layer. The membranes containing the other oxides have somewhat lower permeation coefficient.

Silica membranes can be synthesized by opposing-reactants deposition and by one-sided deposition, the latter resulting in thinner deposited layers and higher permeation coefficients. Within the range of conditions employed, titania and alumina membranes were obtained only in the opposing-reactants deposition, the one-sided deposition failing to produce pore plugging. A direct heterogeneous mechanism seems to be responsible for the opposing-reactants deposition of all four oxides. It also explains the one-sided deposition of SiO_2. However, the rapid homogeneous reaction between $TiCl_4$ and H_2O or $AlCl_3$ and H_2O seems to interfere with the one-sided deposition of TiO_2 and Al_2O_3.

Acknowledgement

Funding by the Department of Energy with UCR Grant DE-FG22-89PC89765 and Contract DE-AC21-90MC26365 is gratefully acknowledged.

References

1. Leiby, Jr., C. C. and C. L. Chen, "Diffusion Coefficients, Solubilities and Permeabilities for He, Ne, H_2, and N_2 in Vycor Glass," *J. Appl. Phys.*, **31(2)**, 268 (1960).

2. Shelby, J. E., "Molecular Solubility and Diffusion," *Treatise on Materials Science and Technology*, M. Tomozawa and R. H. Doremus (Eds.), Vol. 17, p. 1 (1979).

3. Boyd, D. C. and D. A. Thompson, "Glass," *Kirk-Othmer Encyclopedia of Chemical Technology*, Vol. 11, p. 807 (1980).

4. Gavalas, G. R., C. E. Megiris, and S. W. Nam, "Deposition of H_2-Permselective SiO_2 Films," *Chem. Eng. Sci.*, **44(9)**, 1829 (1989).

5. Nam, S. W. and G. R. Gavalas, "Stability of H_2-Permselective SiO_2 Films Formed by Chemical Vapor Deposition," *AIChE Symp. Ser.*, **85 (268)**, 68 (1989).

6. Gavalas, G. R. and C. E. Megiris, "Synthesis of SiO_2 Membrane on Porous Support and Method of Use of Same," *U.S. Patent* 4,902,307 (1990).

7. Lee, R. W., "Diffusion of Hydrogen in Natural and Synthetic Fused Quartz," *J. Chem. Phys.*, **38(2)**, 448 (1963).

8. Reichmann, M. G. and A. T. Bell, "Raman Study of the Preparation of SiO_2-Supported TiO_2 from $TiCl_4$ and HCl," *Langmuir*, **3(1)**, 111 (1987).

9. Armistead, C. G. and J. A. Hockey, "Reactions of Chloromethyl Silanes with Hydrated Aerosil Silicas," *Trans. Farad. Soc.*, **63**, 2549 (1967).

10. Hudson, R. F.,"The Vapor Phase Hydrolysis of Non-metallic Chlorides," *Proc. Int. Congr. of Pure and Appl. Chem.*, p. 297 (1947).

11. Armistead, C. G., A. T. Tyler, F. H Hambleton, S. A. Mitchell, and J. A. Hockey, "The Surface Hydroxylation of Silica," *J. Phys. Chem.*, **73(11)**, 3947 (1969).

12. Hair, M. L. and W. Hertl, "Chlorination of Silica Surfaces," *J. Phys. Chem.*, **77(17)**, 2070 (1973).

13. Tolmachev, V. A. and M. A. Okatov, "Investigation of Process for Synthesizing Ultrathin Titanium Oxide Layers in Porous Glass," *Sov. J. Opt. Technol.*, **51(2)**, 104 (1984).

14. Wong, P. and M. Robinson, "Chemical Vapor Deposition of Polycrystalline Al_2O_3," *J. Am. Ceram. Soc.*, **53(11)**, 617 (1970).

Table 2.1 Conditions of deposition and permeation coefficients of the resulting membranes.

Code	Oxide	Reaction Geometry	Reactants (atm) Chloride	Reactants (atm) H_2O	Reaction Temp (°C)	Reaction Time (min)	Gas Permeation Coefficients $\left(\frac{cm^3(STP)}{cm^2\text{-}min\text{-}atm}\right)$ at 450°C H_2	at 450°C N_2	at Deposition T H_2	at Deposition T N_2
S1	SiO_2	opposing	0.30	0.07	700	180	0.03	$2.5x10^{-5}$	0.09	$30x10^{-5}$
S2	SiO_2	opposing	0.30	0.07	800	90	0.02	0.65	0.11	7.5
S3	SiO_2	one-sided	0.15	0.04	800	25	0.09	8	0.29	150
S4	SiO_2	one-sided	0.15	0.04	600	10	0.28	7	0.43	70
S5	SiO_2	one-sided	0.15	0.04	400	95	0.08	500	0.07	400
S6	SiO_2	one-sided	0.02	0.025	600	55	0.35	50	0.53	250
A1	Al_2O_3	opposing	0.20	0.07	800	120	0.003	5.5	0.02	28
A2	Al_2O_3	opposing	0.20	0.07	450	60	0.004	2.4	0.01	2.4
A3	Al_2O_3	opposing	0.20	0.07	450	30	0.03	6.3	0.03	6.3
A4*	Al_2O_3	opposing	0.20	0.07	450	30	0.01	1.5	0.01	1.5
B1	B_2O_3	opposing	0.10	0.10	450	105	0.1	2.0	0.10	2
B2	B_2O_3	one-sided	0.10	0.10	500	10	-	-	0.30	40
B3	B_2O_3	opposing	0.10	0.10	150	90	-	-	0.03	5
T1	TiO_2	opposing	0.20	0.12	450	35	0.09	59	0.09	59
T2	TiO_2	opposing	0.20	0.12	450	60	0.06	3.8	0.06	3.8
T3	TiO_2	opposing	0.20	0.12	600	35	-	-	0.17	38
T4	TiO_2	opposing	0.20	0.12	600	60	-	-	0.08	5.9
T5	TiO_2	opposing	0.20	0.12	800	50	-	-	0.02	110
untreated	-	-	-	-	-	-	0.7	19,000	-	-

*same as A3 but annealed at 700°C overnight after deposition

Table 2.2 One-sided deposition experiments which did not result in pore plugging within two hours of reaction.

Code	Oxide	Reactants (atm) H_2O	Reactants (atm) chloride	Reaction temperature (°C)	Comment
A5*	Al_2O_3	0.10	0.04	200	
A6*	Al_2O_3	0.10	0.04	600	
A7*	Al_2O_3	0.10	0.04	800	
B4**	B_2O_3	0.10	0.10	150	
B3**	B_2O_3	0.10	0.10	400	
T6	TiO_2	0.12	0.20	450	substrate remains clear
T7	TiO_2	0.12	0.20	600	substrate remains clear
T8	TiO_2	0.12	0.20	200	substrate remains clear
T9	TiO_2	0.12	0.01	450	white film formed
T10	TiO_2	0.12	0.01	600	white film formed
T11	TiO_2	0.12	0.01	300	homogeneous reaction particles

* no permeation change

** slow permeation change

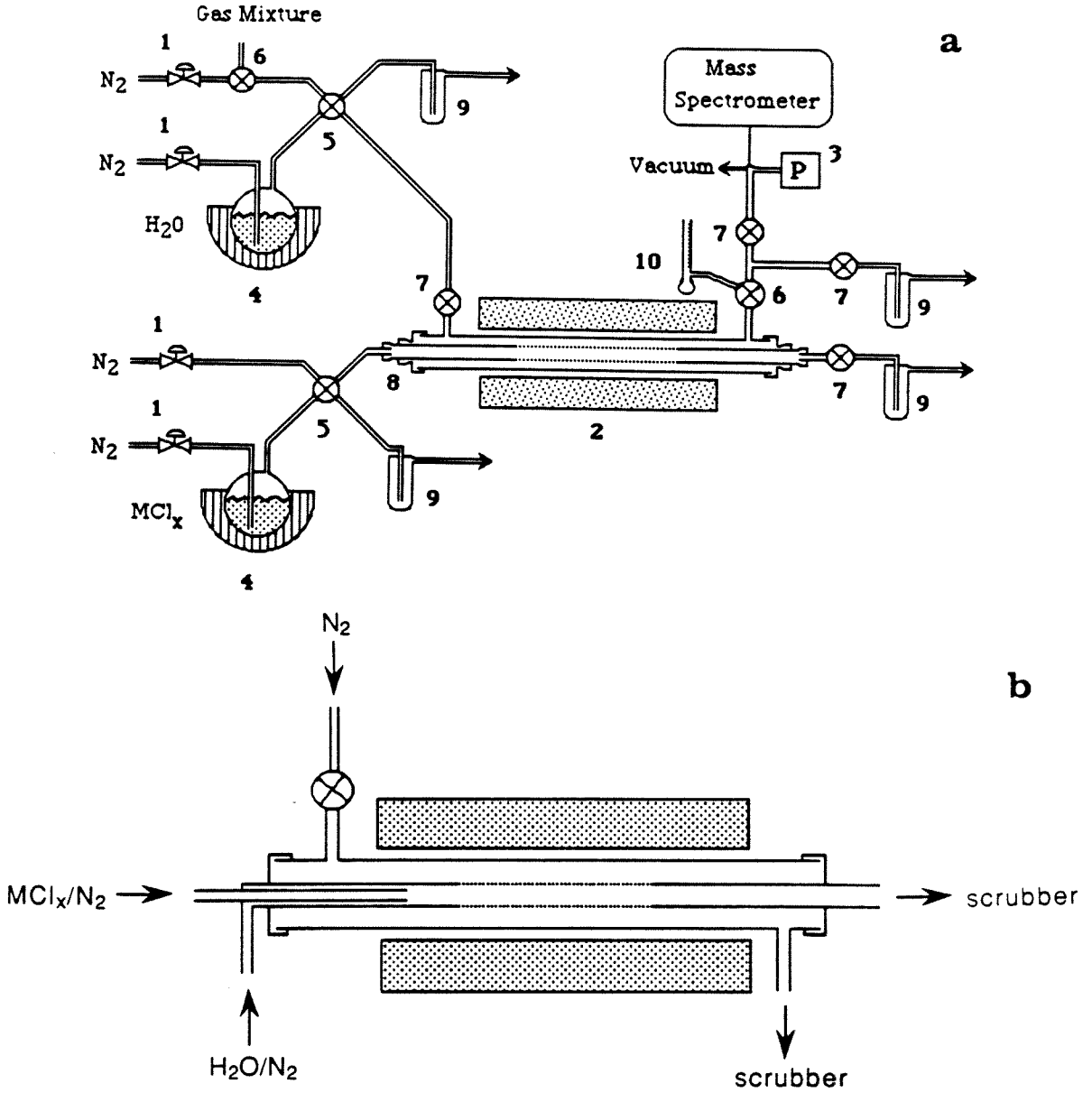

Figure 2.1 (a) Schematic of the reactor system for opposing-reactants deposition. 1, mass flowmeter with valve; 2, furnace with temperature controller; 3, pressure transducer; 4, bubbler with heating element and temperature controller; 5, four-way valve; 6, three-way valve; 7, on-off valve; 8, special fitting; 9, scrubber; 10, bubble flowmeter. (b) Schematics of reactant inlet for one-sided deposition.

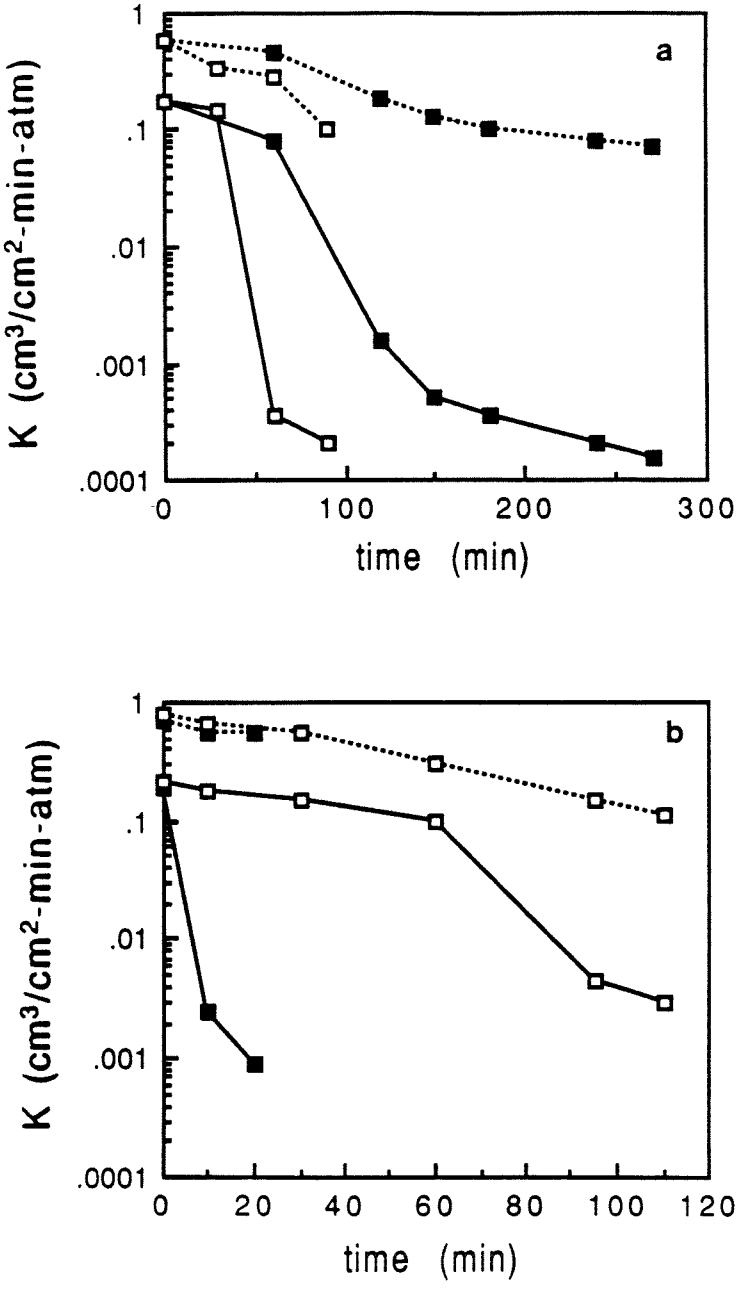

Figure 2.2 Permeation rate coefficients at deposition temperatures for hydrogen (- - -) and nitrogen (—) versus time of deposition by $SiCl_4$ and H_2O reaction. (a) opposing-reactants geometry at 700°C (▪) and 800°C (▫). (b) one-sided deposition at 600°C (▪) and 400°C (▫). Reactant stream was 4% H_2O and 15% $SiCl_4$ in N_2.

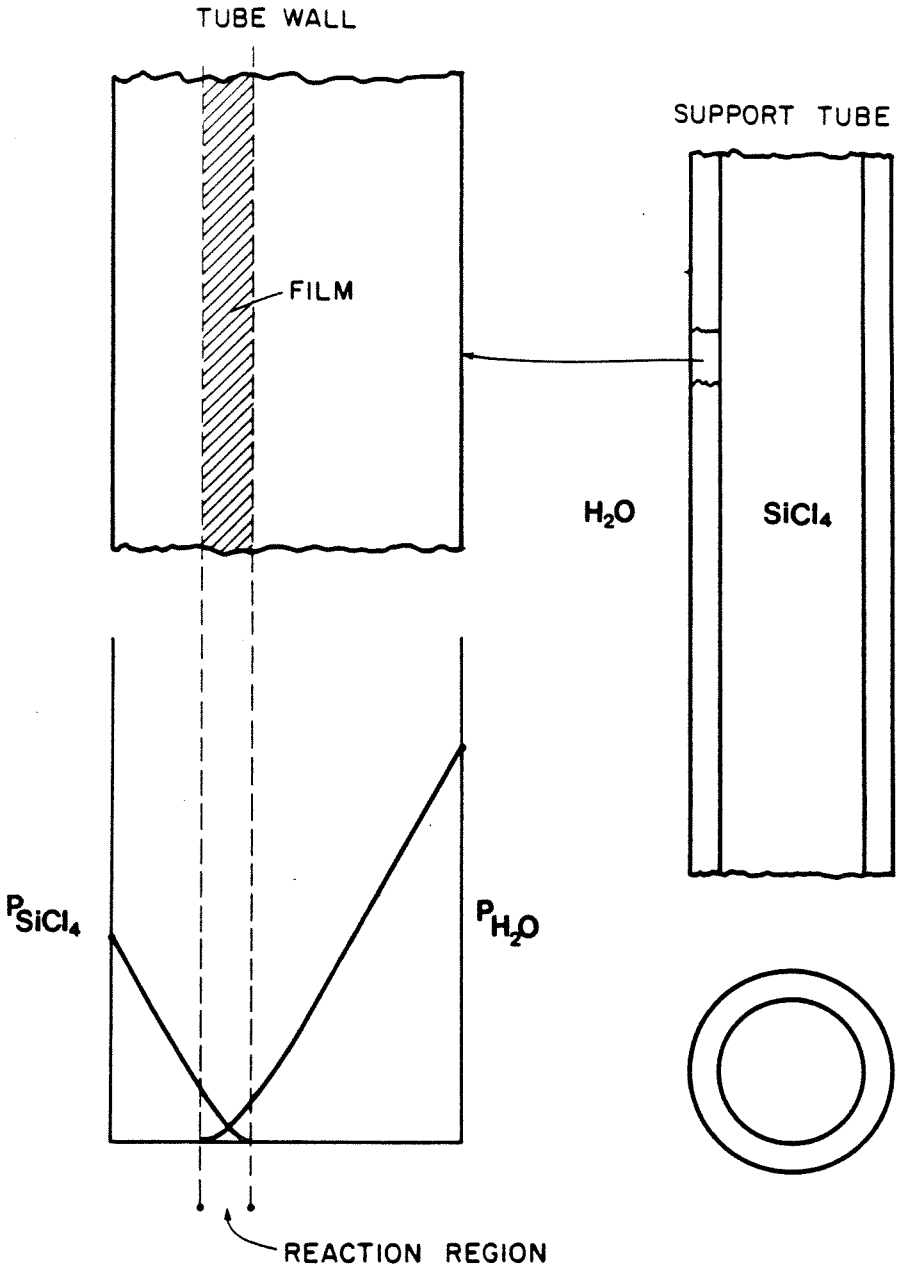

Figure 2.3 Schematic of concentration profiles in opposing-reactant deposition.

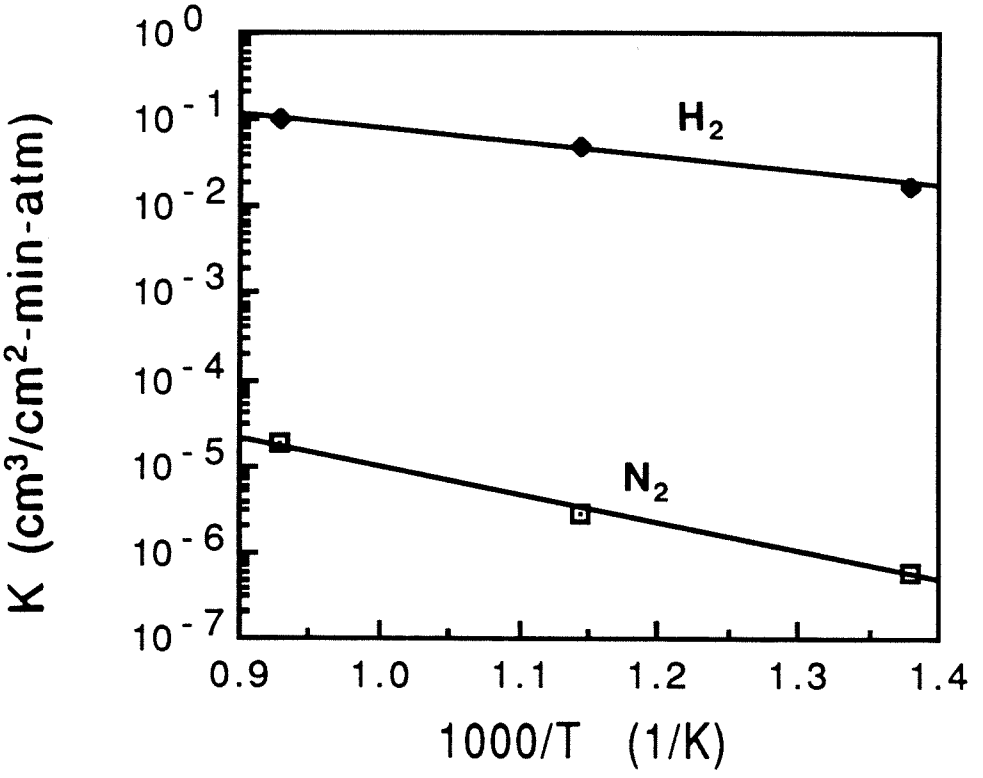

Figure 2.4 Arrhenius plots for H_2 and N_2 permeation coefficients of SiO_2 membranes. E_{H_2} = 37 kJ/mol; E_{N_2} = 60 kJ/mol.

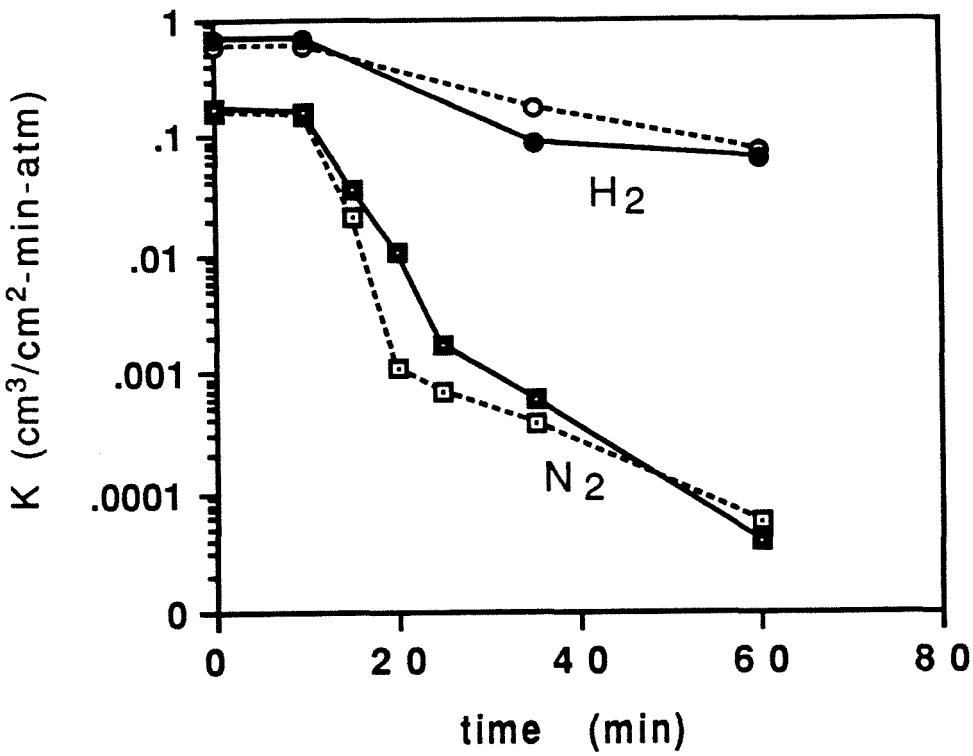

Figure 2.5 N_2 (□, ■) and H_2 (○, ●) permeation coefficients of TiO_2 membranes during deposition at 450°C (—) and 600°C (- - -). Reactants: 20% $TiCl_4$-N_2 and 12% H_2O-N_2.

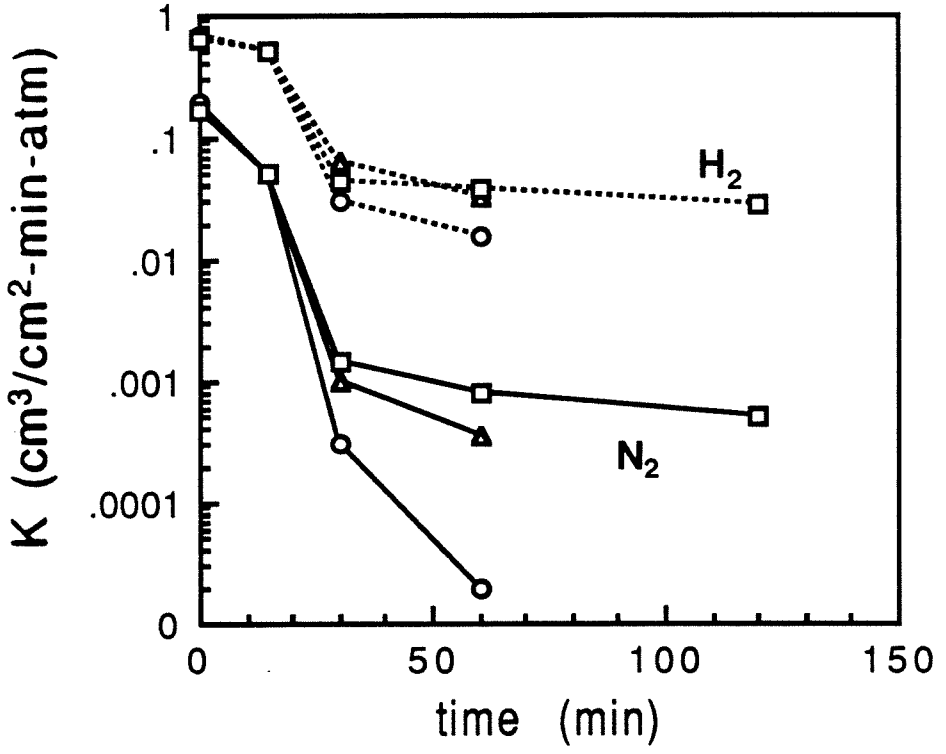

Figure 2.6 Permeation rate coefficients measured during deposition of Al_2O_3 for H_2 (- - -) and N_2 (—) at 450°C (○), 700°C (△), and 800°C (□). Reaction streams were 7% H_2O-N_2 and 20% $AlCl_3$-N_2 in opposing-reactants geometry.

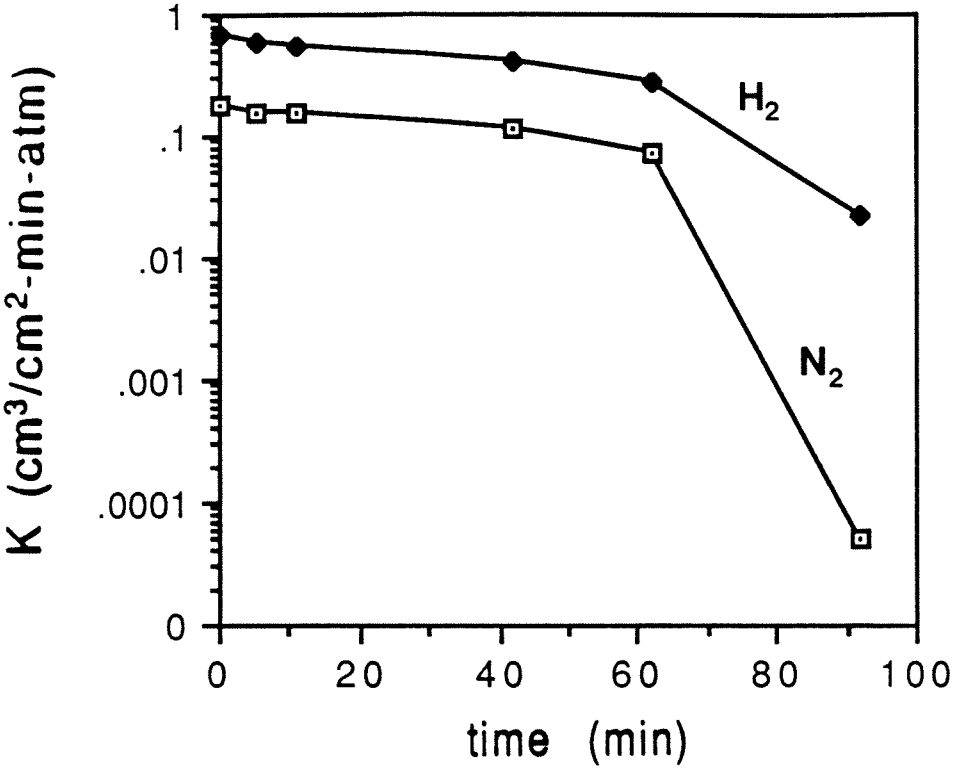

Figure 2.7 H_2 and N_2 permeation coefficients at 150°C during deposition of B_2O_3 in opposing-reactants geometry. Reactant streams: 10% BCl_3-N_2 and 10% H_2O-O_2.

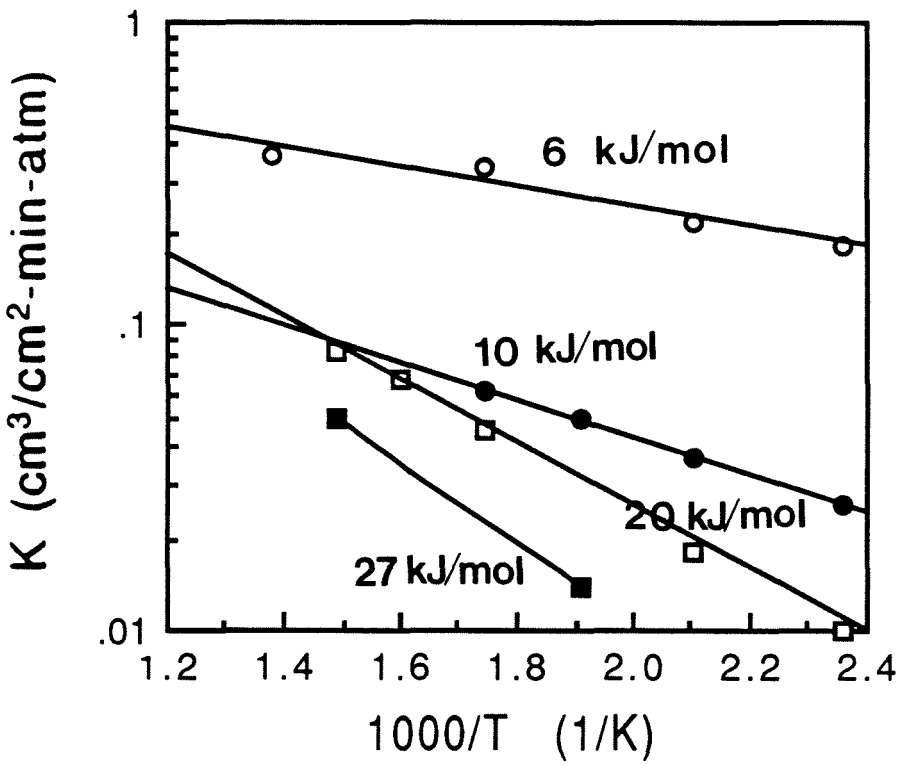

Figure 2.8 H_2 permeability coefficients of a B_2O_3 membrane deposition at 150°C and annealed under dry N_2 at 400°C overnight (▪), 300°C (□), and 150°C overnight (•) and exposed to laboratory air at room temperature for 23 days (○). Calculated activation energies are given on the figure.

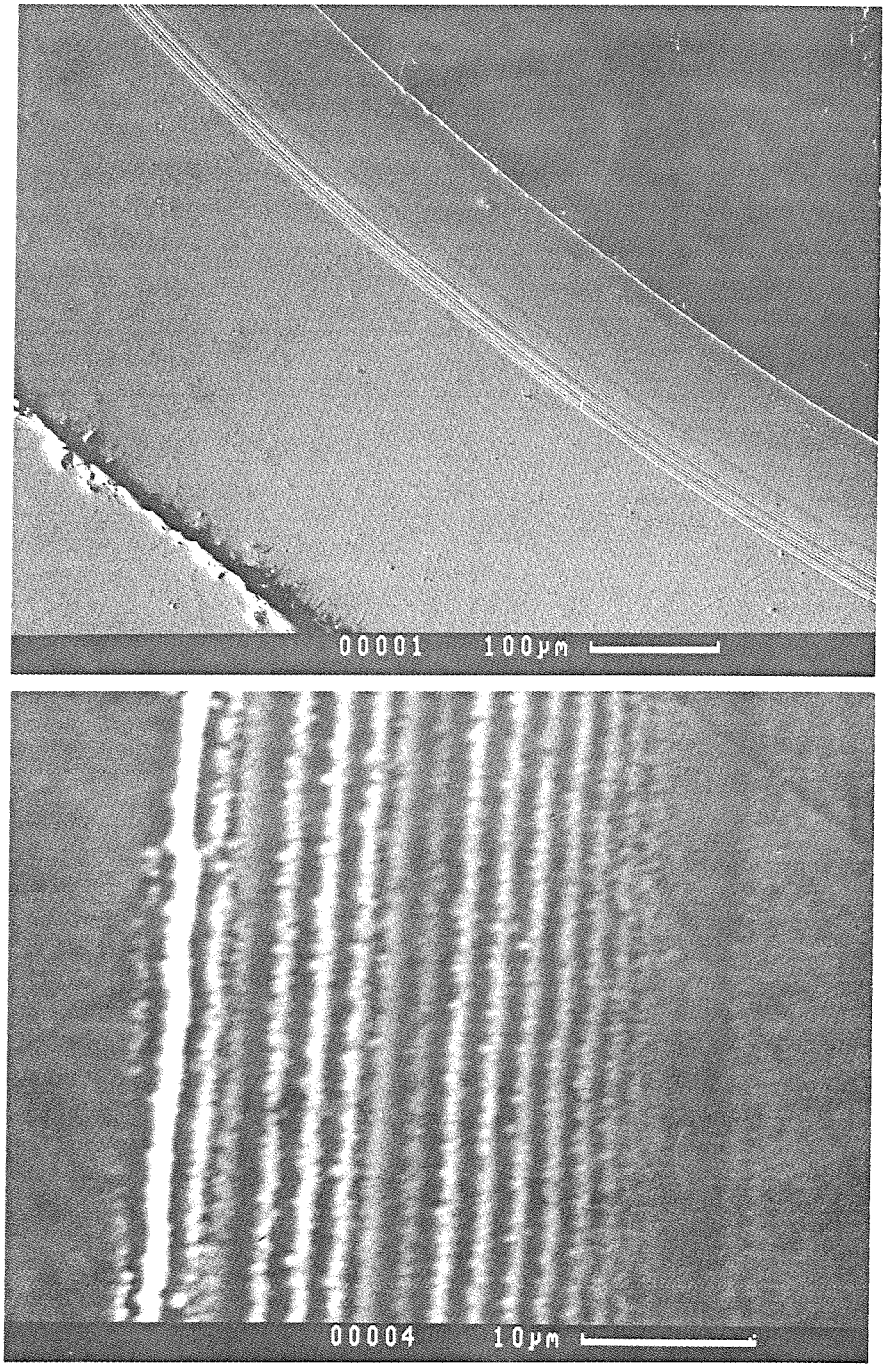

a

b

Figure 2.9 (a) Scanning electron micrographs of tube cross sections containing TiO_2 deposited at 600°C and (b) at higher magnification.

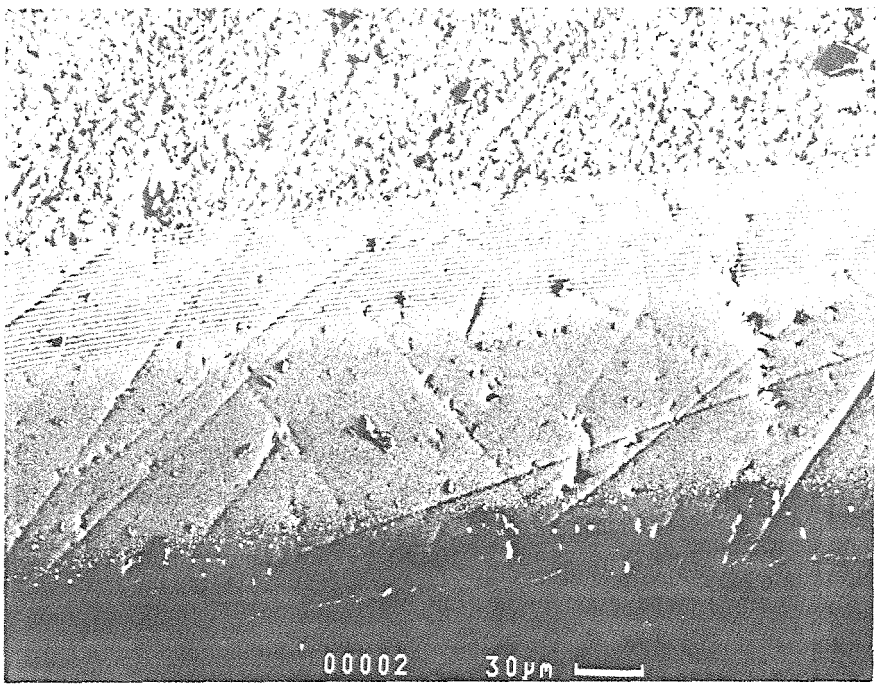

Figure 2.9 (c) Scanning electron micrographs of tube cross sections containing TiO_2 deposited at 450°C.

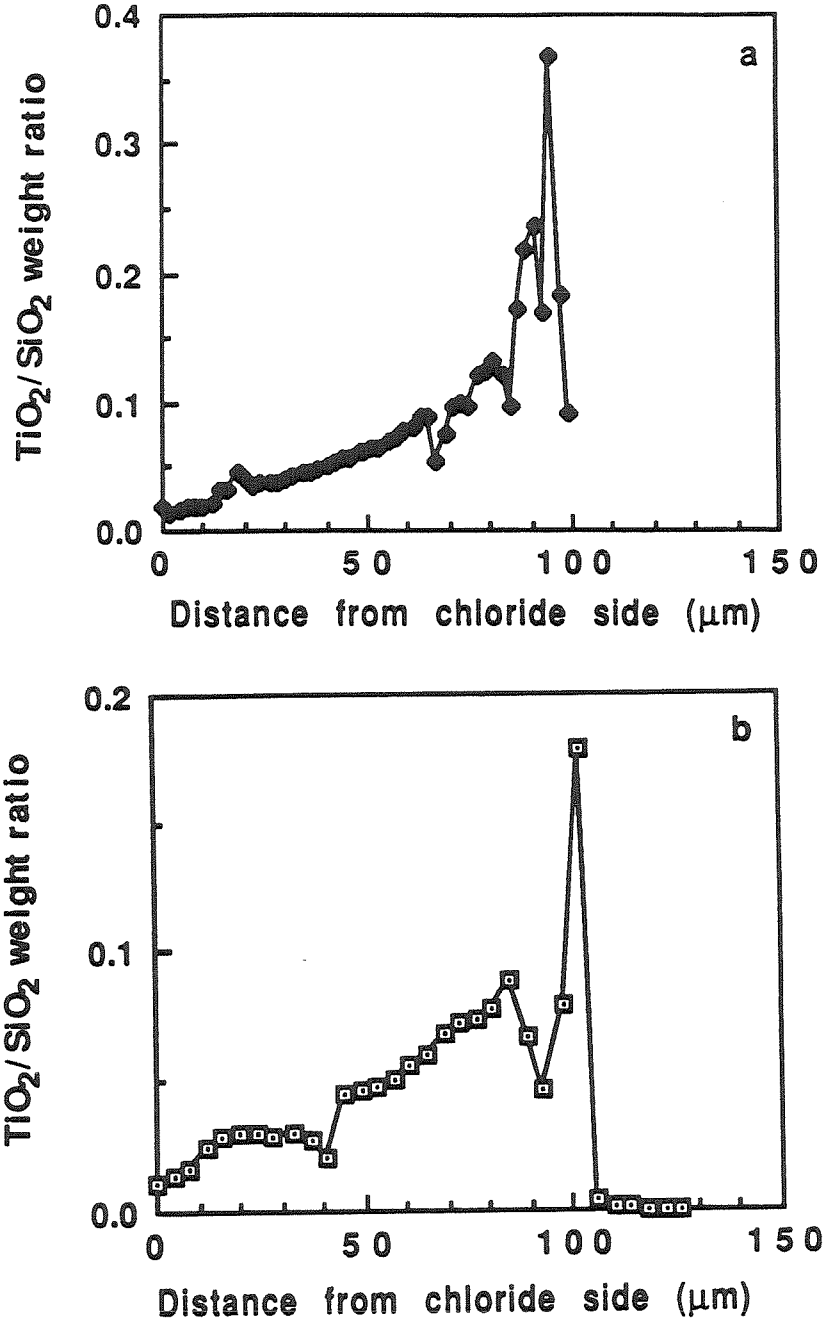

Figure 2.10 (a) EMA line scan of tube cross sections containing TiO_2 layers deposited at 600°C, and (b) 450°C.

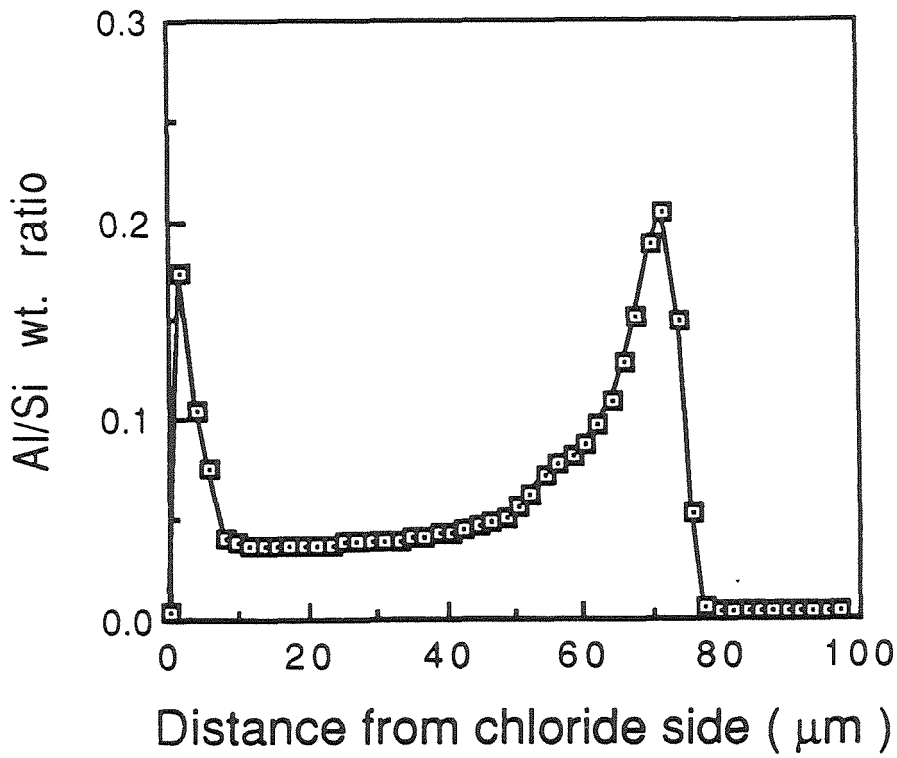

Figure 2.11 EMA linescan of a tube cross section containing Al_2O_3 layer deposited at 800°C in an opposing-reactants geometry. Reactant streams were 7% H_2O-N_2 and 20% $AlCl_3$-N_2.

Chapter III

Characterization of TiO_2 Membranes

Abstract

TiO_2 membranes were characterized by electron microscopy and electron microprobe analysis. The membranes were prepared by chemical vapor deposition at various temperatures using the opposing-reactant geometry. The spatial distribution of the TiO_2 deposit formed at 450°C and 600°C showed an asymmetric profile suggesting a heterogeneous mechanism for the reaction. The more symmetric density profile of the TiO_2 layer produced at 200°C indicated that homogeneous reaction as well as heterogeneous was important at a lower temperature. The activation energy of H_2 diffusion was greater for the membrane prepared at higher temperature. The membranes experienced a decrease in H_2 permeances and selectivity when heat treated in a high pressure gas mixture containing water vapor. Transmission electron microscopy of TiO_2 layers annealed at 800°C showed the anatase form of TiO_2.

3.1 Introduction

Synthesis of hydrogen permselective oxide membranes by chemical vapor deposition (CVD) was described in the previous chapter [1]. The permselective properties of SiO_2, TiO_2, and other oxide membranes were reported. SiO_2 membranes were successfully produced in both opposing-reactants geometry and one sided geometry. TiO_2 membranes, on the other hand, could be synthesized only using the opposing-reactant geometry. This difference was attributed to the high rate of homogeneous $TiCl_4$ hydrolysis in one sided geometry, which depleted rapidly the reactant concentrations, inhibiting the heterogeneous reaction. The deposition process can be dominated by homogeneous or heterogeneous reactions or both, depending on the reactant composition, the nature of the substrate, and the temperature. The roles of heterogeneous and homogeneous reactions on the formation of TiO_2 layers can be further investigated by conducting experiments with different experimental parameters.

Characterization of physical properties of the deposit layers is important in understanding the transport and reaction mechanism in the CVD process. The deposit profiles of the TiO_2 membranes were obtained from electron microprobe x-ray analysis. While it has been difficult to characterize SiO_2 films in Vycor (SiO_2) support tubes, TiO_2 films in Vycor supports is more easily distinguished, and thus can be characterized more effectively. Additional characterization of TiO_2 membranes by scanning electron microscopy (SEM) and electron microprobe analysis (EMA) from the samples prepared at different temperatures can provide qualitative comparison of the reaction mechanism at various temperatures. Transmission electron microscopy (TEM) can be used to study smaller scale morphological features of the membranes. At the same time, the electron diffraction capability of

TEM can provide information about the crystallinity of TiO_2 membranes [1].

3.2 Experimental Techniques

3.2.1 Preparation of Membranes

The experimental techniques for membrane deposition and permeation measurement were presented in the previous chapter. TiO_2 layers were deposited by opposing-reactants geometry.

3.2.2 Scanning Electron Microscopy and Electron Microprobe Analysis

For scanning electron microscopy and electron microprobe analysis, a small piece of the support tube containing TiO_2 was first cast in epoxy, cross sectioned, polished, and coated with carbon for electron conduction. The sample prepared was then examined by a *CamScan* electron microscope operating at 20 kV with the resolution of approximately 50Å. EMA was conducted by a *JEOL 733 Superprobe.*

3.2.3 Transmission Electron Microscopy

A thin cross section of the tube containing TiO_2 was examined using transmission electron microscopy (TEM). The tube was cut into a thin slice by a low-speed diamond blade and hand-ground and polished to the thickness of approximately 0.1 mm. The polished sample was mechanically dimpled to create a small hole across the profile and then ion milled to further decrease the thickness of the hole edges. Figure 3.1 shows the sample on a TEM holder (3 mm diameter) just before ion milling. The prepared sample was coated with carbon for electron conduction. A *Phillips 301* transmission electron microscope was used at 100 kV.

3.3 Results and Discussion

3.3.1 Permeance and Selectivity

TiO_2 membranes were synthesized by opposing-reactants geometry at 200°C, 300°C, 450°C, 600°C, and 800°C. The permeances of H_2 and N_2 in these membranes are listed in Table 3.1. The selectivity ratio, H_2:N_2, is in the range of 200–500 except for the membrane produced at 800°C which had a low H_2 permeance and selectivity. The TiO_2 layer deposited at this temperature (800°C) is believed to be crystalline with a high density, thus has lower H_2 permeance [1]. In general, the permeances of H_2 in TiO_2 membranes were lower than those in SiO_2 membranes.

3.3.2 Density Profiles and Reaction Mechanism

The deposit profiles of TiO_2 membranes deposited at 450°C and 600°C are shown in the previous chapter. The profiles featured asymmetric shape: a narrow peak with a gradual decrease toward the chloride side and a sharp decrease toward the water side. The peak region which corresponds to the point of pore plugging and is responsible for the separating properties is located at about 100μm from the boundary of $TiCl_4$ flow. The broad tail part does not contribute to the membrane selectivity, since the pathways in this region are still open, but decreases the membrane permeance somewhat.

The asymmetric feature in TiO_2 deposit density is caused by a heterogeneous reaction mechanism, discussed in the previous chapter. The first stage of the reaction takes place between gaseous $TiCl_4$ and hydroxyl groups on the surfaces of Vycor. The resulting surface -O-$TiCl_3$ groups subsequently react with H_2O diffusing from the other side, regenerating -OH groups. The TiO_2 layer is built

up on the pore surface by simultaneous chlorination and hydrolysis. The reaction front gradually moves toward the water side because the rate of chlorination is higher than that of hydrolysis. The reaction continues until the pores become plugged in a narrow region. The diffusion of bulky $TiCl_4$ becomes increasingly slow with the layer growth, while that of H_2O is relatively faster due to its smaller molecular size, thus the deposit growth does not advance far from the chloride side. The uniform striation of the TiO_2 layer shown in Figure 2.9 perhaps indicates the uniform advancement of the reaction front.

The composition profiles of two tube cross sections containing TiO_2 deposited at 600°C and 450°C are shown in Figure 3.2 for comparison. The totally plugged region in the layer deposited at 600°C is located closer to the chloride side than that in the layer deposited at 450°C. Also, the maximum value of TiO_2/SiO_2 weight ratio of the layer formed at 600°C is greater than the one formed at 450°C, although the reaction time was the same (60 minutes) for both depositions. This illustrates the effect of the reaction kinetics on the location and the thickness of the deposit layer. At 600°C, the layer was growing faster due to higher reaction rate, completing the pore plugging with less advancement of the deposit growth to the water side. With prolonged reaction time at 600°C, the reactant (particularly H_2O) continued to diffuse through the deposit layer and increased the thickness of the deposit. The thickening of the deposit layer occurred mainly from the chloride side because the diffusion of bulky $TiCl_4$ through the deposit toward the water side was almost impossible while that of H_2O toward the chloride side was slow but continuing. The deposit thickening reduced the H_2 permeance and selectivity, as shown in Table 3.1. At 450°C on the other hand, the slower reaction rate delayed pore plugging. After 60 minutes of reaction time the layer extended to a larger volume, but the totally plugged region was much thinner; therefore,

the selectivity and permeance of H_2 at the end of 60 minutes of deposition were higher than those of the layer prepared at 600°C. Also, since the totally plugged region was thinner at 450°C, the maximum value of TiO_2/SiO_2 weight ratio in the profile was lower. However, the true values of TiO_2/SiO_2 ratio in the totally plugged regions should be the same for both layers deposited at 450°C and 600°C at approximately 0.7 (considering the density of TiO_2 and Vycor) which is much higher than those shown in the profiles. The lower values in the electron probe trace are due to the finite volume excited by the electron beam on the sample surface. The characteristic x-ray intensities were averaged over the volume of 5μm diameter which was bigger than the scale of totally plugged regions.

The TiO_2 layer deposited at the lower temperature displayed some distinct features as compared to the ones formed at higher temperatures. The EMA line scan of the TiO_2 deposit layer prepared at 200°C is shown in Figure 3.3. The profile of the deposit density looks more symmetric compared to those of Figure 3.2. The fact that the peak region has sharp edges on both sides strongly suggests that a homogeneous reaction mechanism was at work. However, the fact that the deposit is located at about 100μm from the $TiCl_4$ flow side, and that the area between the $TiCl_4$ side to the peak region is uniformly coated with TiO_2 indicated significant involvement of the heterogeneous reaction as well. Since the homogeneous reaction between $TiCl_4$ and H_2O is known to take place much faster at low temperature region [2], we can assume that the reaction mechanism at 200°C was a combination of both heterogeneous reaction (indicated by the location of the layer) and homogeneous reaction (indicated by the symmetric profile). Figure 3.4 shows a scanning electron micrography of the TiO_2 layer deposited at 200°C. The layer formed at 200°C does not contain the striated structure that appeared in the images of layers formed at the higher temperatures

(Figure 2.9).

3.3.3 Activation Energy

The TiO_2 membranes prepared at various temperatures were annealed at 600°C under N_2 flow for 1 day in order to stabilize their permeances. Then the permeance of H_2 was measured at several temperatures. From Arrhenius plots of the permeances, the values of the activation energy for H_2 diffusion were calculated and listed in Table 3.2. The higher the temperature for deposition, the higher the activation energy, indicating a higher density of the deposit produced.

3.3.4 Heat Treatment

The TiO_2 membranes were heat treated in a high pressure mixture of N_2, H_2, H_2O, and CO_2 to evaluate the stability of the membranes in a typical environment of H_2 separation applications. The H_2 permeances decreased by 50% to 75%, while the N_2 permeances remained almost the same resulting in a decrease of selectivity. The permeances of H_2 and N_2 before and after the treatments are listed in Table 3.3. The decrease of permeance and selectivity was caused by densification of the layer as in the case of SiO_2 [3,4].

3.3.5 Transmission Electron Microscopy

When the membranes prepared at 450°C or 600°C were annealed at 800°C, the permeance of H_2 and the selectivity decreased significantly. As discussed in the previous chapter, this was believed to be caused by the phase transformation of amorphous TiO_2 to crystalline TiO_2 [5,6]. To verify this supposition, a sample was prepared from a membrane that was produced at 600°C and subsequently annealed at 800°C to be examined by TEM.

A transmission electron micrograph of a Vycor tube section that is largely free of TiO_2 deposit is shown in Figure 3.5. The large black dots in the middle of the picture are carbon particles coated on the surface to aid electron conduction. The porous network is shown as the bright contrast on the dark background of Vycor glass. Sample preparation by ion milling produced thickness variations which made it difficult to distinguish the contrast [7]. However, an estimate of the pore sizes (30Å–100Å) was obtained. In the lower middle section of the picture, the porous network in a small area is missing due to some TiO_2 deposit which is shown in the dark field image as brightly diffracting particles.

The tube section containing TiO_2 is shown in Figure 3.6 (a), (b), and (c). The particles of TiO_2 in the pores appear as dark spots in the bright field image. The larger black particles shown throughout the image are the carbon particles. In the dark field image, the TiO_2 particles are brightly diffracting and distinguished from the carbon particles. Highly diffracted images of TiO_2 particles appear to be bigger than their actual size because of the strong contrast from the background.

Figure 3.7 shows the electron diffraction pattern of the area concentrated with TiO_2. The ring pattern is created by the polycrystalline nature of randomly oriented TiO_2 particles. The crystal structure of TiO_2 can be determined by measuring the relative distances of the diffraction rings and by comparing with the combination of the indices of TiO_2 crystals. The diffraction pattern was determined to be consistent with the unit cell parameters of anatase TiO_2 [8].

3.4 Conclusions

TiO_2 membranes prepared by chemical vapor deposition in opposing-reactants geometry were characterized. The physical structure of the membranes

were examined by SEM. The spatial density profiles of the membranes obtained from EMA showed different characteristics depending on deposition temperature. The reaction mechanism at 450°C and 600°C was dominated by heterogeneous reaction, and the reaction at 200°C was both heterogeneous and homogeneous. The deposit produced at higher temperatures was denser as indicated by higher activation energy of H_2 diffusion. Heat treatment in a high pressure mixture of various gases reduced the H_2 permeances and selectivity of the membranes. TEM of a layer deposited at 600°C and subsequently annealed at 800°C gave a diffraction pattern characteristic of the anatase structure.

References

1. Tsapatsis, M., S. Kim, S. W. Nam, and G. R. Gavalas, "Synthesis of Hydrogen Permselective SiO_2, TiO_2, Al2O3, and B2O3 Membranes from the Chloride Precursors," *Ind. & Eng. Chem. Res.*, **30**, 2152 (1991).

2. Hudson, R. F. "The Vapor Phase Hydrolysis of Non-metallic Chlorides," *Proc. Int. Congr. Pure Appl. Chem.*, 297 (1947).

3. Nam, S. W. and G. R. Gavalas, "Stability of H_2-Permselective SiO_2 Films Formed by Chemical Vapor Deposition," *AIChE Symp. Ser.*, **85 (268)**, 68 (1989).

4. Arndt, J., "Densification of glasses of the system TiO_2-SiO_2 by Very High Static Pressures," *Phys. Chem. Glasses*, **24 (4)**, 104 (1969).

5. Reichmann, M. G. and A. T. Bell, "Raman Study of the Preparation of SiO_2-Supported TiO_2 from $TiCl_4$ and HCl," *Langmuir*, **3 (1)**, 111 (1987).

6. Sankur, H. and W. Gunning, "Crystallization and Diffusion in Composite TiO_2-SiO_2 Thin Films," *J. Appl. Phys.*, **66 (10)**, 4747 (1989).

7. Gavalas, G. R., "Silica Membranes for Hydrogen Separation in Coal Gas Processing," *Final Report to U. S. Dept. of Energy*, Report No. DE-FG22-89PC89765 (1993).

8. Whitehead, J. "Titanium Compounds, Inorganic," *Kirk-Othmer Encyclopedia Chem. Technol.* Vol. 23, p. 131 (1980).

Table 3.1 Permeation coefficients of N_2 and H_2 in TiO_2 membranes prepared at various temperature.

Deposition Temperature	Deposition time	Permeance (cm^3 (STP)/min atm cm^2) at deposition T H_2	at deposition T N_2	at 600°C H_2	at 600°C N_2
200°C	30 min	0.026	0.00087	0.15	0.00069
300°C	30 min	0.044	0.00066	0.088	0.00052
450°C	35 min	0.088	0.00059		
450°C	60 min	0.064	0.00054	0.096	0.00027
600°C	35 min	0.17	0.00038	0.17	0.00038
600°C	60 min	0.079	0.00059	0.079	0.00059
800°C	50 min	0.020	0.0011		

Reaction conditions: Opposing-reactants geometry
0.20 atm $TiCl_4$ and 0.12 atm H_2O

Table 3.2 Activation energy of H_2 permeation in TiO_2 membranes

Deposition temperature	Deposition time	E_{act} for H_2 permeation (kJ/mol)
200°C	30 min	14.8
300°C	30 min	16.0
450°C	2 hour	18.4
600°C	2 hour	20.2

The permeances were measured after annealing at 600°C under N_2 for 1 day.

Table 3.3 Permeation coefficients of N_2 and H_2 in TiO_2 membranes before and after heat treatments.

Reaction temp.	Reaction time	Permeation coefficient (cm^3 (STP)/min atm cm^2) at 600°C after deposition H_2	after deposition N_2	after treatment 1 H_2	after treatment 1 N_2	after treatment 2 H_2	after treatment 2 N_2
200°C	35 min	0.17	0.00057	0.068	0.00067	0.061	0.00056
450°C	45 min	0.15	0.00054	0.045	0.00052	0.037	0.00055
600°C	45 min	0.19	0.00073	0.081	0.00086	0.076	0.00086

Reaction conditions: Opposing-reactants geometry
0.10 atm $TiCl_4$ and 0.20 atm H_2O

Treatment 1 : 2 days at 550°C in 10 atm mixture of N_2, H_2, CO_2, and H_2O.
Treatment 2: 3 additional days in the same condition.

Figure 3.1 Optical microscope image of a tube cross section containing TiO_2 layer on 3mm TEM sample holder.

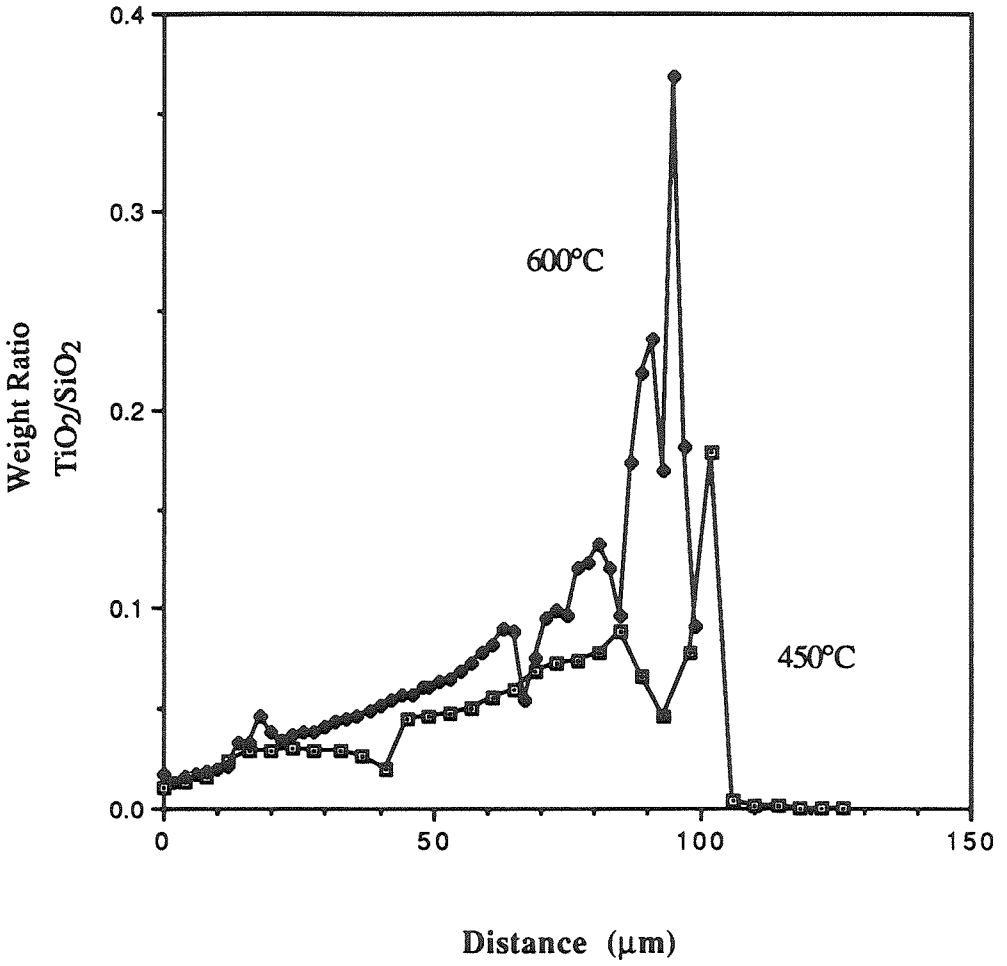

Figure 3.2 Spatial density profiles of deposit from EMA line scan of tube cross sections containing TiO_2 layers.

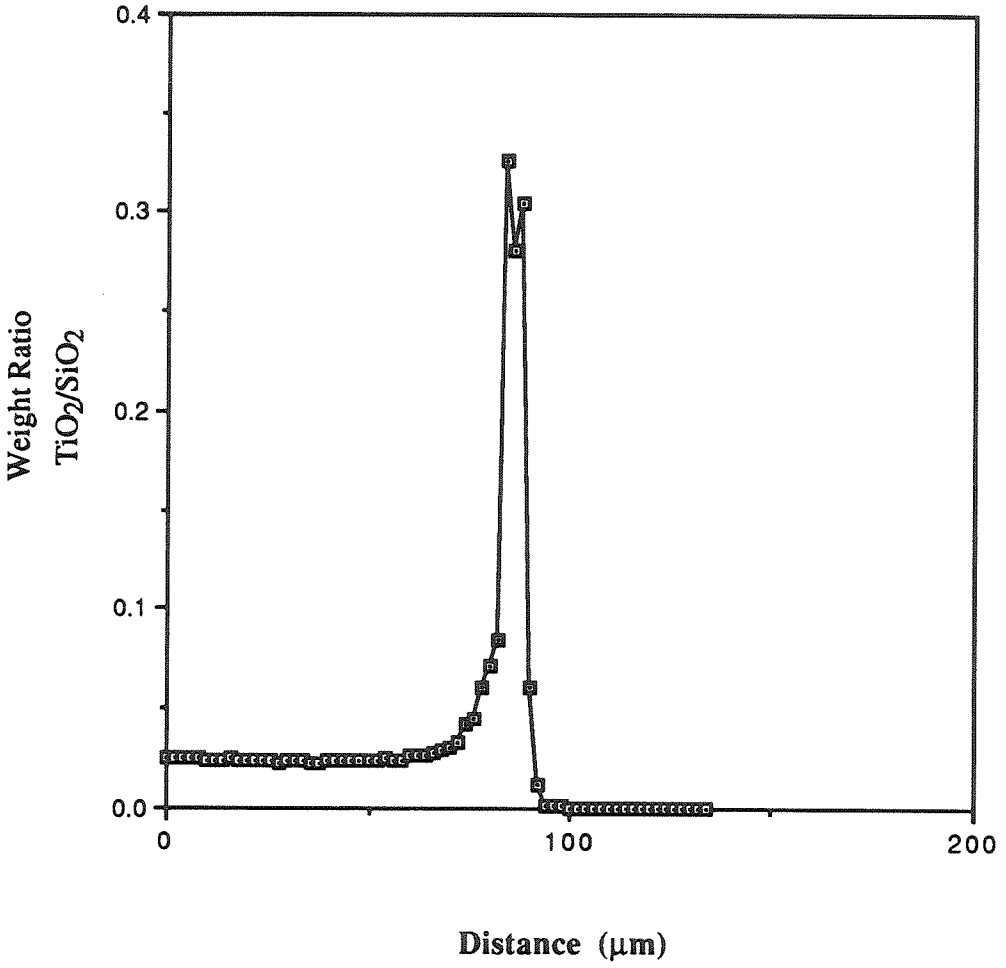

Figure 3.3 EMA line scan of a tube cross section containing TiO_2 layer deposited at 200°C.

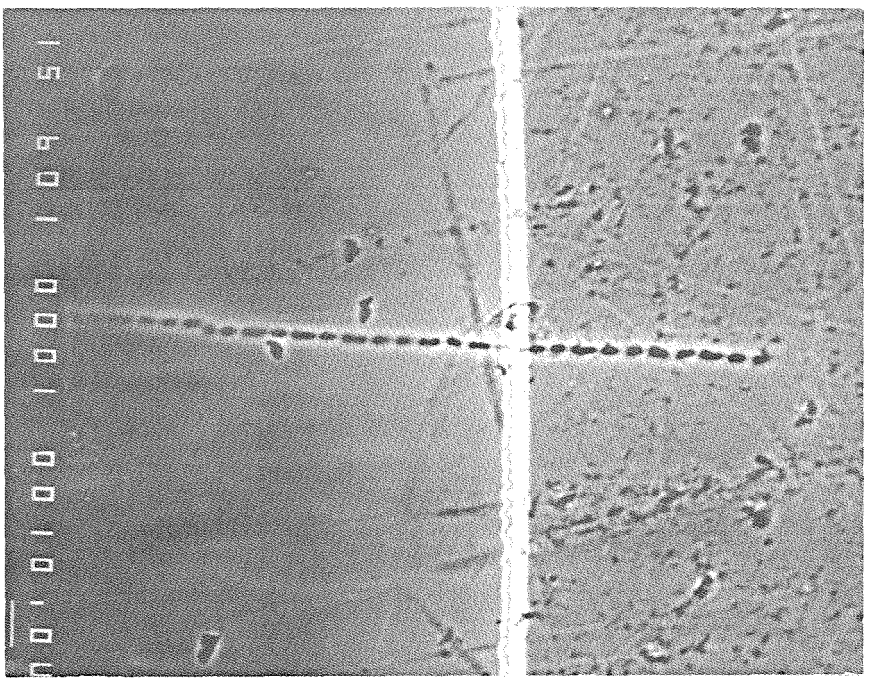

Figure 3.4 Scanning electron micrographs of a tube cross sections containing TiO_2 deposited at 200°C. Marker is 10μm.

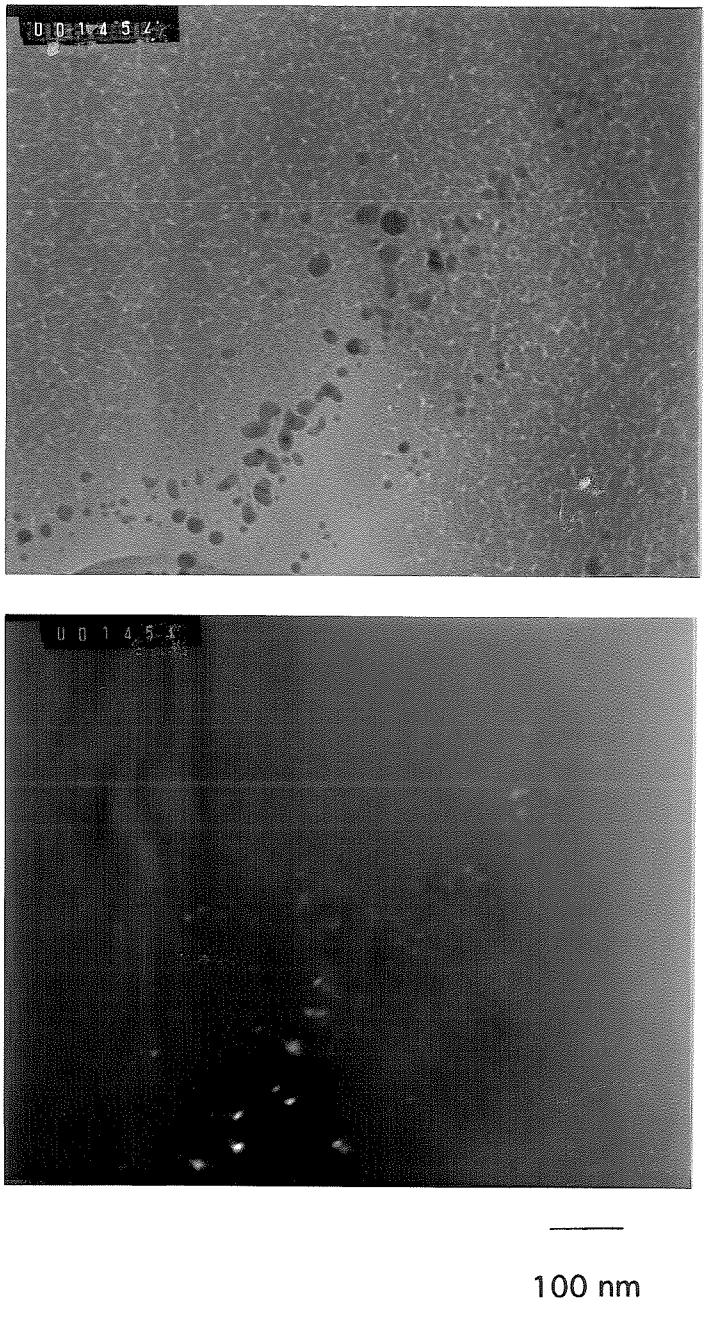

Figure 3.5 Transmission electron micrograph of a largely untreated section of Vycor tube: (a) bright field image and (b) dark field image.

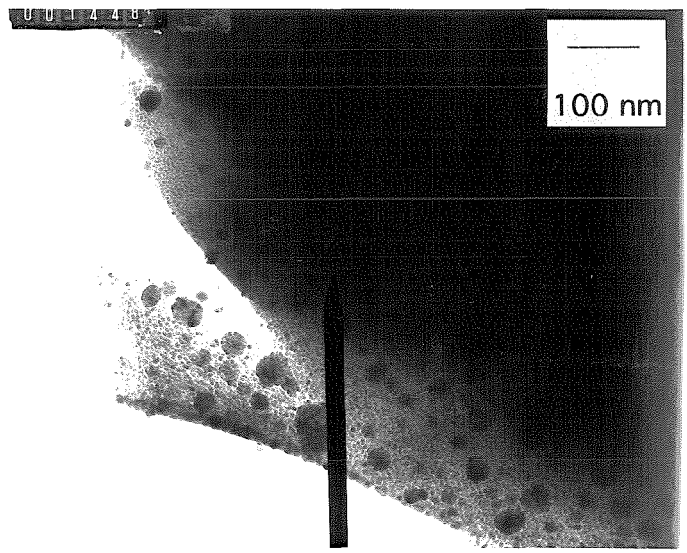

a

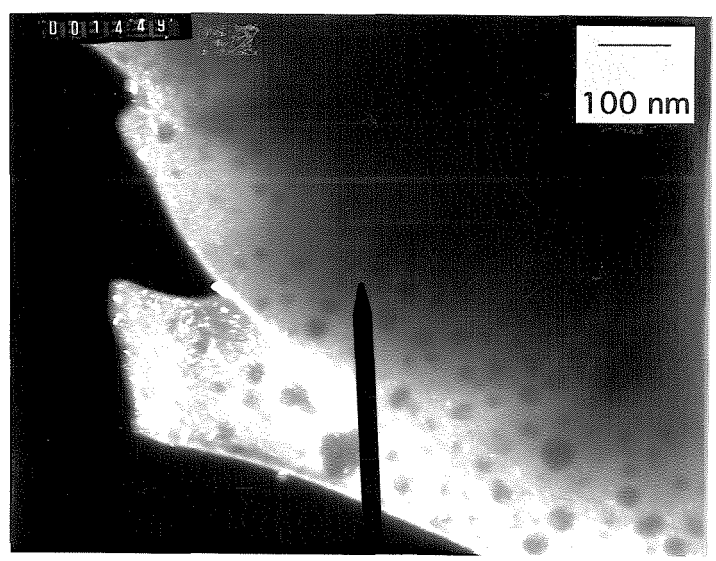

b

Figure 3.6 Transmission electron micrograph of a tube section containing TiO_2 deposited at 600°C and subsequently annealed at 800°C. (a) bright field image and (b) dark field image.

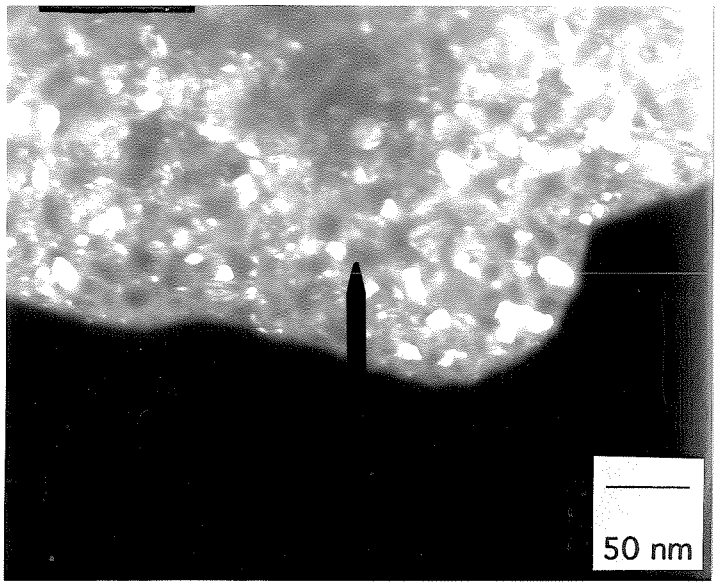

Figure 3.6 (c) TEM dark field image of a tube section containing TiO_2 deposited at 600°C and subsequently annealed at 800°C.

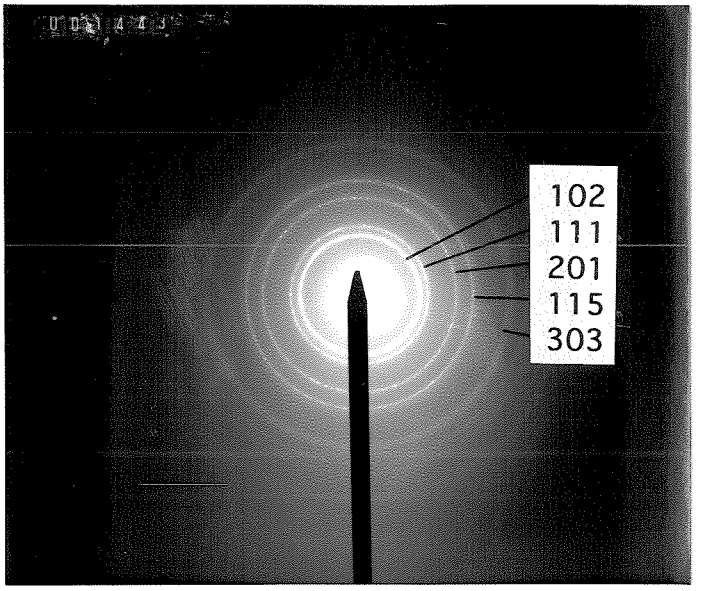

Figure 3.7 Electron diffraction pattern of the TiO_2 rich area shown in Figure 3.6 and corresponding crystal indices of anatase TiO_2.

Chapter IV

Kinetic Study of the Reactions of Chlorosilanes with Porous Vycor Glass

Published in *J. Colloid Interface Sci.*, **161**, 6 (1993).

Abstract

The alternating reactions of $SiCl_4$ and H_2O with the surface of Vycor glass have been studied by thermogravimetric analysis at 400–600°C. The results are interpreted by postulating two types of silanol groups (Si-OH) on the Vycor surface, paired and isolated. Reaction of $SiCl_4$ with paired silanols proceeds by competing steps which control the total extent of silylation. Upon reaction with H_2O, all surface Si-Cl groups are hydrolyzed reproducing Si-OH. Simultaneous silanol-silanol and silanol-surface chloride condensations eliminate H_2O or HCl to form new Si-O-Si bridges with final product silica. A kinetic model incorporating the silylation, hydrolysis and condensation steps describes well the TGA data.

4.1 Introduction

Chlorosilanes in the gas phase or in solution react readily with silanols (Si-OH groups) on the surface of silicas to form new silicon-bearing groups on the surface, e.g.,

$$SiOH\ (s) + SiCl_4\ (g) \rightarrow SiOSiCl_3\ (s) + HCl\ (g) \quad (1)$$

$$SiOH\ (s) + Si(CH_3)_3Cl\ (g) \rightarrow SiOSi(CH_3)_3\ (s) + HCl\ (g) \quad (2)$$

Reaction (2) and analogous reactions with other trialkylchlorosilanes are routinely used to convert silica surfaces to hydrophobic for chromatographic applications or to make glass fibers compatible with polymer resins in composite materials [1,2]. Reactions (1) and (2) and the analogous reactions with $AlCl_3$, BCl_3, and $TiCl_4$ have been used to probe the surface of various silicas [3–5] and, along with IR studies [e.g., 6–9], have provided detailed information about the nature and concentration of surface silanols.

When the glass surface silylated according to (1) is exposed to liquid water or to water vapor at elevated temperatures, hydrolysis of the SiCl bonds generates new silanol groups with the end result

$$Si\text{-}O\text{-}SiCl_3\ (s) + 3H_2O\ (g) \rightarrow Si\text{-}O\text{-}Si(OH)_3\ (s) + 3HCl\ (g) \quad (3)$$

Contacting the glass surface with $SiCl_4$ and H_2O simultaneously results in the growth of a silica layer by simultaneous silylation, hydrolysis and condensation steps,

$$Si\text{-}OH\ (s) + SiCl_4\ (g) \rightarrow Si\text{-}O\text{-}SiCl_3\ (s) + HCl\ (g) \quad (4)$$

$$Si\text{-}Cl\ (s) + H_2O\ (g) \rightarrow Si\text{-}OH\ (s) + HCl\ (g) \quad (5)$$

$$Si\text{-}OH\ (s) + Si\text{-}OH\ (s) \rightarrow Si\text{-}O\text{-}Si\ (s) + H_2O\ (g) \quad (6)$$

$$\text{Si-OH (s)} + \text{Si-Cl (s)} \rightarrow \text{Si-O-Si (s)} + \text{HCl (g)} \qquad (7)$$

The growth of silica layers on a glass surface contacted with $SiCl_4$ and H_2O has been used in our laboratory to prepare hydrogen membranes based on the well known permeation selectivity of silica for hydrogen [10,11]. The membranes are prepared by flowing a mixture of $SiCl_4$ and H_2O vapor through the bore (or around the external surface) of a mesoporous (40Å mean pore diameter) glass tube (Vycor) at atmospheric pressure and 600–700°C temperature [10,11]. The silica generated by reactions (4)–(7) gradually constricts the pores at and near the surface of the tube until the internal pore surface becomes inaccessible to $SiCl_4$. The constricted layer formed in this fashion is highly selective to hydrogen permeation providing hydrogen permeance about 0.3 $cm^3(STP)/(min \cdot cm^2 \cdot atm)$ and H_2:N_2 permeation selectivity in the 500–1000 range, both properties at 450°C. The permeance and selectivity of the silica membranes clearly depend on the spatial distribution of the silica deposit and are, therefore, controlled by kinetics of various steps in (4)–(7).

Among previous studies dealing with the reactions between chlorosilanes and silica surfaces we note the study of Evans and White [3] who recognized the consecutive nature of reactions (4) and (7) but did not measure the rates of the two steps individually. Hair and Hertl [5] derived an overall rate expression for silylation without considering reaction (7) as a kinetically significant step. The kinetics of the hydrolysis and condensation steps (6) and (7) have not been examined in these studies. In this paper we present results on reactions (4)–(7) with particular emphasis on uncoupling the kinetics of steps (4) and (7).

4.2 Experimental Techniques

Kinetic measurements were conducted using a *DuPont 951* thermogravimetric analyzer (TGA) interfaced to a microcomputer, illustrated schematically in Figure 4.1. A sample of approximately 20 mg ground Vycor glass of particle size below 100μm was placed as a thin layer on a quartz pan inside the quartz housing of the TGA, and pretreated by heating for 3 hours in N_2 flow of 200 cm^3/min at a specified pretreatment temperature (usually 600°C) in order to stabilize the number of surface silanols. In the tables and the Vycor samples are labeled as V600 if pretreated at 600°C, V450 if pretreated at 450°C, etc. Subsequent to the pretreatment the sample was brought to the reaction temperature and subjected to a flow of 9% $SiCl_4$-N_2 at a 250 cm^3/min flowrate. The silylation continued until the weight leveled off and was followed by a purge with a stream of 200 cm^3/min N_2 for 0.5 hour to remove all traces of gaseous reactants and products from the TGA. The purge was followed by reaction with a stream of 7% H_2O-N_2 at a 250 cm^3/min flowrate and by a purge with nitrogen at a 200 cm^3/min flowrate. For selected samples the cycle of silylation and hydrolysis with intermediate N_2 purges was repeated several times.

4.3 Experimental Results and Discussion

Figure 4.2 shows a TGA trace for the first silylation and the succeeding purge of a sample held at 600°C. Silylation is initially rapid with more than 70% of the total weight increase occurring within the first one half minute. The silylation rate slows down considerably after the first minute but is still appreciable after two minutes when the flow is switched to purge. Upon switching to purge the

weight started decreasing slowly and this decrease continued for at least twenty minutes. During the hydrolysis period the weight decreased due to the replacement of chloride groups by -OH groups (Figure 4.3). A slower decrease of weight occurred during the purge following hydrolysis. Figure 4.4 shows two complete reaction cycles at 600°C. The general features of the second cycle are similar to those of the first.

The weight decrease during the purge period can be explained by the consecutive reactions of the chloride groups with neighboring -OH groups:

$$\text{Si-O-SiCl}_3\ (s) + \text{Si-OH}\ (s) \rightarrow \text{Si-O-SiCl}_2\text{O-Si}\ (s) + \text{HCl}\ (g) \qquad (8)$$

$$\text{Si-O-SiCl}_2\text{O-Si}\ (s) + \text{Si-OH}\ (s) \rightarrow \text{Si-O-SiClO-Si}\ (s) + \text{HCl}\ (g) \qquad (9)$$

$$\qquad\qquad\qquad\qquad\qquad\qquad\qquad\qquad\qquad\qquad\qquad\qquad\quad |$$

$$\qquad\qquad\qquad\qquad\qquad\qquad\qquad\qquad\qquad\qquad\qquad\qquad\quad \text{O-Si}$$

The fact that reaction (8) is a slow step following the first silylation is consistent with our experimental observation that prolonging the purge diminished the weight loss during the subsequent hydrolysis by simply consuming chloride groups which would otherwise be available for hydrolysis. Further confirmation of the role of reactions (8) and (9) was obtained by an experiment using $Si(CH_3)_3Cl$ instead of $SiCl_4$. The silylation reaction in this case can be written as

$$\text{Si-OH}\ (s) + \text{Si}(\text{CH}_3)_3\text{Cl}\ (g) \rightarrow \text{Si-O-Si}(\text{CH}_3)_3\ (s) + \text{HCl}\ (g) \qquad (10)$$

whereupon there is no opportunity for subsequent reactions like (8) and (9). In this experiment, silylation was slower, and there was no weight decrease during the purge period.

The rate of reactions (8) and (9) depends on the concentration of chlorides and neighboring silanols. Table 4.1, comparing the weight changes of samples pretreated at different temperatures, shows that the weight decrease during the purge

succeeding silylation is higher for the sample pretreated at the lower temperature. The table also shows that the samples pretreated at the higher temperature had smaller weight gain during silylation. Preheating clearly reduces the concentration of surface -OH groups which are the reaction sites in silylation (reaction (1)).

Kinetic analysis of the TGA traces suggests that silylation does not proceed with all -OH groups at the same rate. When one of two neighboring -OH groups has reacted according to (1), silylation of the neighboring unreacted group is much slower, because of steric hindrance. The competition between the hindered silylation and the slow condensation reactions can be verified by comparison of the two experiments shown in Figure 4.5. Curve A shows the weight change of a sample subjected to 30 minutes of continuous $SiCl_4$ flow. Most of the weight gain was achieved during the first 1.5 minutes, while during the next 28 minutes the weight increased very slowly. This slow weight increase can be attributed to -OH groups of lower reactivity due to either steric hindrance by neighboring $-SiCl_3$ groups, or due to an initially sterically hindered position on the surface. Curve B is the trace of a sample subjected to 1.5 minutes of $SiCl_4$ flow followed by 15 minutes of purge followed by another $SiCl_4$ flow of nearly 30 minutes. Similar to curve A, the large weight gain during the first 1.5 minutes is due to the silylation of fast reacting -OH groups. During the succeeding purge, there is enough time for condensation reactions (8) and (9) to proceed without any competition with additional silylation. When gaseous $SiCl_4$ is introduced again, the weight increase during 30 additional minutes is less than that for trace A, since a large fraction of the -OH groups remaining after the first silylation was consumed by reactions (8) and (9) during the intermediate purge.

The weight loss during reaction with H_2O is due mainly to the hydrolysis of surface chloride groups by gaseous water (reaction (5)). This reaction is slower

than silylation and at 450°C, for example, the major weight loss under flow of 7% H_2O-N_2 lasted about 8 minutes as compared to the 5 minutes taken by silylation with 9% $SiCl_4$-N_2. Simultaneously with hydrolysis the even slower condensation reactions (6) and (7) also contribute to the weight loss. The condensation reaction (6) continues beyond the hydrolysis period into the final purge period.

In one experiment, repeated cycles of silylation and hydrolysis with intermediate N_2 purge were conducted until there was no more weight gain during the silylation step. This freezing of the reaction evidently occurs when the accumulation of the SiO_2 product is sufficiently advanced to prevent further diffusion of the reactants into the particle interior. At the point of this disruption of pore connectivity, the voids have not been completely eliminated. A certain residual void fraction has remained which, however, is inaccessible to $SiCl_4$, in accordance with the precepts of percolation theory. Subsequent to the disruption of connectivity, the reaction continues on the external particle surface and within small pore clusters connected to the surface, resulting in a negligible further weight gain. As shown in Figure 4.6, the weight of the sample initially increased almost linearly, and leveled off at about the tenth cycle with a total weight gain after 20 cycles of about 24%. Given an initial void fraction of 0.3, complete pore filling by material having the true (skeletal) density of Vycor (2.18) would give a 43% weight gain. The lower weight gain measured after 20 complete cycles seems to be partly due to the lower density of the highly defective SiO_2 deposit, and partly due to the residual porosity remaining after the disruption of pore connectivity.

Figure 4.7 shows the weight changes during silylation and hydrolysis for each of the twenty consecutive cycles. Consistent with the weight trace shown in Figure 4.6, the weight changes decreased in each successive silylation and hydrolysis. It is interesting to note that while the weight increase in the second and third

silylation periods is less than that of the first, the weight decrease in the second and third hydrolysis periods is either about the same, or in some cases, higher than that of the first. This may be explained by the location and accessibility of the reactive groups in the deposit layer. During the first silylation all silanol groups are on the initial pore surface, and are therefore, accessible to the bulky $SiCl_4$ molecules. In subsequent silylations the silanol groups at the top layer are accessible, but the groups buried in subsurface layers are increasingly inaccessible. As the area of the top layer decreases with the deposition of additional layers, the number of -OH groups accessible to $SiCl_4$ also decreases. By contrast, during hydrolysis, the small water molecules can reach readily the chloride groups in subsurface layers as well as those in the top layer. Similarly, the condensation of favorably located silanol groups can take place throughout the deposit. The extent of both reactions can increase with successive reaction cycles, although this increase tapers off after the second or third cycles because the number of remaining reactive groups at any given point below the surface continues to decrease.

4.4 Kinetic Model Description

The main feature of this model is the classification of silanols on the Vycor surface into isolated silanols and paired silanols. Illustrated in Figure 4.8 are the silylation reactions for the two classes of silanols. The reactions involving unpaired silanols and the silanols of each completely unreacted pair are relatively fast, and are assumed to have the same rate. For the paired silanols, two parallel paths are possible after the first silylation reaction. One path is silylation of the second silanol. This path is assumed to be slow because of steric hindrance by the neighboring bulky -$SiCl_3$ group. The other path is condensation of one of

the chloride groups with the remaining silanol. Condensation of a second chloride group as in reaction (9) will be neglected as this would require a much less likely initial configuration of three silanols in close proximity.

At 600°C silylation is very fast and largely controlled by external diffusion (from the free stream to the sample) and pore diffusion. In view of the large mass transfer limitations the kinetic analysis presented below used only the lower temperature data (400, 450, and 500°C). Although less pronounced at temperatures below 500°C, these mass transfer resistances should still be taken into account in quantitative kinetic analysis. The effect of external mass transfer is taken into account here using a convective mass transfer coefficient estimated from existing correlations for flow past a flat plate (the sample pan). Pore diffusion introduces more significant complications, for it creates intraparticle concentration gradients for the surface species as well as for the gaseous reactants. For a detailed analysis of the diffusion-reaction problem, it is necessary to treat the surface species concentrations as functions of time and intraparticle position. Such an elaborate analysis is not justified in view of the other simplifications made and in view of the irregular shape and variable size of the Vycor granules in the sample. Consequently, the surface species were characterized by a single concentration representing an average over the whole sample. The variation of the gas concentrations, on the other hand, was taken into account by using an effectiveness factor η calculated from standard reaction-diffusion theory assuming that silylation and hydrolysis are first order in the concentrations of $SiCl_4$ and H_2O, respectively. A detailed analysis that we have carried out for the case of a single silylation step (neglecting condensation reactions) shows that using the spatially averaged species concentration, instead of the concentration profile, introduces a small error ($< 2\%$) when the reaction Thiele modulus is below 1. Calculating the effectiveness factor on the

basis of spherical particles of uniform radius is a crude but inevitable approximation which probably corrects for most of the intraparticle diffusion effects which, in any case, are important only during the initial rapid silylation.

4.4.1 Silylation

On the basis of the above-assumptions the reactions during silylation and purge may be described by the following equations

$$\frac{dy_1}{dt} = \eta\, k_1 (a_1 - y_1)\, c_s \tag{11}$$

$$\frac{dy_2}{dt} = k_2\, y' \tag{12}$$

$$\frac{dy_3}{dt} = \eta\, k_3\, y'\, c_s \tag{13}$$

$$\frac{dy'}{dt} = 2\eta\, k_1\, (a_2 - y' - y_2 - y_3)\, c_s - k_2\, y' - \eta\, k_3\, y'\, c_s\,, \tag{14}$$

where the y_1, y_2, y_3 and y' are the concentrations of the various surface groups (defined in Figure 4.8) per unit mass of sample, a_1 and a_2 are the initial concentration of single and paired -OH groups, respectively, c_s is the concentration of $SiCl_4$ on the external particle surface, and η is the effectiveness factor. Initially all the y_i are zero.

To implement Equations (11)–(14) it is necessary to express c_s and η in terms of the free-stream concentration of $SiCl_4$ and the concentrations of the surface species. To determine c_s we used the following relation for the average mass transfer coefficient for laminar boundary layer parallel to a flat plate [14]:

$$Nu_L = \frac{k_c\, L}{D_{AB}} = 0.664\, Re_L^{1/2}\, Sc^{1/3}. \tag{15}$$

To implement the calculation of k_c, we estimated D_{AB} for $SiCl_4$-N_2 using standard procedures [15].

The balance between transfer of $SiCl_4$ from the free stream to the particle layer and reaction within the sample, yields the following expression

$$c_s = \frac{k_c\, c_o}{\eta\, k_1\, (a_1 - y_1 + 2\,(a_2 - y_2 - y_3 - y'))\frac{W_o}{A} + k_c}, \tag{16}$$

where c_o is the concentration of $SiCl_4$ in the fluid stream, W_o is the initial mass of the Vycor sample and A is the interfacial area of the sample layer. The surface concentration varies with time via the time dependence of the y_i. Since the sample pan does not quite have a flat plate geometry and since the area on the pan occupied by the particle layer is not exactly known, application of Equation (16) involves significant uncertainty equivalent to a 25% uncertainty on the mass transfer coefficient.

To take into account the effect of pore diffusion, an effectiveness factor, η, has been included in the rate expressions. This factor is obtained from standard theory using the Knudsen diffusion coefficients and assuming spherical particles of equal size,

$$\eta = \frac{3}{\phi}\left(\frac{1}{\tanh\phi} - \frac{1}{\phi}\right)$$

$$\phi = R_p \sqrt{\frac{k_1\, a\, \rho}{D_{eff}}},$$

where

$$a = a_1 - y_1 + 2\,(a_2 - y_2 - y_3 - y')$$

and

$$D_{eff} = \frac{D_k\, \epsilon}{\tau} = \frac{2}{3}\,\overline{r}\,\sqrt{\frac{8\,R\,T}{\pi\,M}}\,\frac{\epsilon}{\tau},$$

with D_k being the Knudsen diffusion coefficient, ϵ the void fraction, $\overline{r}$ the mean pore radius (taken equal to 20 Å), τ the empirical tortuosity factor set equal to 3, R the gas constant, T the temperature, and M the molecular weight.

4.4.2 Purge Following Silylation

At time t_p, the $SiCl_4$ flow is terminated, and the only possible reaction is condensation of the surface species. This is described by

$$\frac{dy_2}{dt} = k_2\, y' \tag{17}$$

$$\frac{dy'}{dt} = -k_2\, y', \tag{18}$$

while y_1 and y_3 remain constant. The initial conditions for y_2 and y' are the values of these concentrations at the end of silylation. To compare the solution of Equations (11)–(14) and (17) and (18) with the weight measurements, we use the following relation between the sample weight and the concentrations y_i,

$$\frac{W(t)}{W_o} = 1 + w_1\, y_1 + w_2\, y' + w_2\, y_2 + w_1\, y_3,$$

where w_1 and w_2 are stoichiometric coefficients relating the concentrations y_i to the sample mass ($w_1 = 133.4, \quad w_2 = 97.0$).

4.4.3 Hydrolysis

The reaction network during hydrolysis is illustrated in Figure 4.9. The reaction rates are expressed in the same manner as in silylation, i.e.,

$$\frac{dx_1}{dt} = \eta\, k_{H1}\, (b_1 - x_1)\, c_s$$

$$\frac{dx_2}{dt} = k_{H2}\, x' + k_{H4}\, x_3$$

$$\frac{dx_3}{dt} = \eta\, k_{H3}\, x'\, c_s - k_{H4}\, x_3$$

$$\frac{dx'}{dt} = 2\,\eta\, k_{H1}(b_2 - x' - x_2 - x_3)\, c_s - k_{H2}\, x' - \eta\, k_{H3}\, x'\, c_s,$$

with initial conditions

$$x_1 = x_2 = x_3 = x' = 0.$$

The expressions for c_s and η are analogous to those listed above for silylation.

4.4.4 Purge Following Hydrolysis

Only condensation reactions take place during the purge period yielding the expressions

$$\frac{dx_2}{dt} = k_{H2}\, x' + k_{H4}\, x_3$$

$$\frac{dx_3}{dt} = -k_{H4}\, x_3$$

$$\frac{dx'}{dt} = -k_{H2}\, x',$$

while x_1 remains constant. The sample weight during hydrolysis and purge can be written as

$$\frac{W(t)}{W_{Ho}} = 1 - (w_{H1}\, x_1 + w_{H2}\, x_2 + w_{H1}\, x_3 + w_{H1}\, x').$$

4.5 Numerical Results and Discussion

To estimate the initial silanol concentrations a_1 and a_2 we used data from the reactions with $Si(CH_3)_3Cl$ and $SiCl_4$. Silylation with $Si(CH_3)_3Cl$ is particularly useful in this respect because there is no competing condensation reaction to influence the weight gain. Thus, the weight gain during prolonged silylation with $Si(CH_3)_3Cl$ yields the total initial concentration $a_1 + 2\,a_2$ of silanols (recalling that a_2 was defined as the concentration of paired silanols). A short silylation with $SiCl_4$, on the other hand, consumes most of the unpaired silanols and one out

of each of the paired silanols. Hence, the weight loss during the purge following the silylation period yields a crude estimate for a_2, the remaining silanols that condense with chloride groups. This first estimate of a_2 was refined to give the best fit with the silylation data at the different temperatures (400, 450, and 500°C). The values of a_1 and a_2 obtained in this way were $a_1 = 5.71 \times 10^{-5}$ and $a_2 = 2.14 \times 10^{-4}$ mol/g of Vycor which correspond to 0.172 isolated -OH/nm^2 and 0.644 pairs of -OH/nm^2 for the samples pretreated at 600°C. Approximately 88% of the surface -OH groups are initially present in pairs. This is consistent with the paper of Peri and Hensley [12] in which they found that more than 95% of the silanols on the surface of silica gel were paired after drying at 400°C and often more than 85% were paired after drying at 600°C.

The rate parameters k_i and k_{Hi} were estimated from the initial slopes of the weight change data. During the first several seconds of silylation or hydrolysis, the sample weight was changing almost linearly, indicating that the process during this short period was not yet significantly affected by the change of surface group concentrations. Thus, the initial rate of silylation could be expressed as

$$rate = k_1 \, (a_1 + 2\, a_2) \, c_{si} \, \eta_i,$$

where c_{si} is the value of c_s initially, given by

$$c_{si} = \frac{k_c \, c_o}{\eta_i \, k_1 \, (a_1 + 2\, a_2) + k_c},$$

and η_i is the value of the effectiveness factor initially, computed from the initial value of the Thiele modulus

$$\phi_i = R_p \left(\frac{k_1 \, \rho \, (a_1 + 2\, a_2)}{D_{eff}} \right)^{1/2}.$$

The rate constant k_{H1} for hydrolysis was estimated by the same procedure.

The remaining rate constant k_2 for silylation and the rate constant k_3 for condensation were estimated by least squares using the complete weight gain or loss curves for the silylation and the purge, respectively. For the estimation of the constant k_3 the experimental data of the extended silylation shown in Figure 4.10 were particularly useful.

Unlike silylation which is hindered by neighboring surface -O-$SiCl_3$ groups, hydrolysis is less affected by such hindrance due to the small size of the water molecules. Accordingly, to simplify estimation, the constant k_{H3} was set equal to k_{H1}.

For convenience of notation we have used the subscript H for the rate constants during hydrolysis and the succeeding purge. However, k_{H2} refers to the same reaction (between a silanol and an adjacent chloride group) as k_2 and was, hence, set equal to k_2. The rate constant of condensation between two -OH groups, k_{H4}, was estimated from the weight loss during the purge following hydrolysis. When comparing the rates of silylation and hydrolysis, we note that k_1 is larger than k_{H1} consistent with the fact that k_3 is the rate constant of reactions with steric hindrance, while k_{H3} is the constant of the hydrolysis reaction which has little or no hindrance.

The model equations were integrated using a fourth-order Runge-Kutta algorithm with fixed step size. Figure 4.11 and Figure 4.12 show comparisons of experimental data and model calculations for silylation and hydrolysis at 400°C, 450°C, and 500°C. In general the kinetic model provides good agreement with the experimental data. The constants and parameters that were used for these calculations are listed in Table 4.2. The Arrhenius plots of the rate constants k_1, k_{H1}, and k_3 are shown in Figure 4.13. The activation energies calculated from the slopes of the Arrhenius plots are given in the figure. Not shown in the figure, the

activation energy of k_2 and k_{H4} calculated is 21.4 kcal/mole and 13.2 kcal/mole, respectively.

Having included the effects of external mass transfer and pore diffusion in the kinetics, it is interesting to examine the magnitude of these effects during a reaction cycle. Figures 4.14(a,b) and 4.15(a,b) show the calculated effectiveness factor and normalized surface concentration vs. time for silylation and hydrolysis, respectively. The effect of the mass transfer rates, both external and internal, is significant only at the beginning of the reaction period and is more pronounced at the higher reaction temperatures. Comparison of Figures 4.14(a,b) and 4.15(a,b) shows that the mass transfer limitations at any given temperature are more important for silylation than for hydrolysis.

The proposed kinetic model has grouped the silanols into isolated and paired. According to the literature there are two types of closely located silanols, geminal and vicinal. A significant number of geminal (connected to the same silicon atom) silanols are expected to remain even after long dehydration at high temperature (up to 700°C), since the combination of these two hydroxyls to form Si=O is forbidden. These geminal groups cannot be considered pairs in the concept of our model, because the possibility of condensation reactions within these geminal groups is virtually zero. Once one of the OH groups has reacted with $SiCl_4$, subsequent condensation reaction would involve the formation of a four-membered ring of two Si atoms connected by two O atoms. Such a structure is known to be impossible since typical -SiOSi- and -OSiO- angles in vitreous silica are much larger than the ones required for the four-membered ring [13]. Therefore, geminal hydroxyls should be considered single hydroxyl groups for the purpose of the model. The paired -OH groups would then consist of vicinal groups. Vicinal pairs also cannot be removed by drying at temperatures up to 700°C because elimination of H_2O

would again require four-membered ring formation. The high incidence of paired surface -OH groups estimated from the data after 600°C pretreatment is consistent with this constraint on condensation. Treating the geminal groups as single -OH groups is convenient but not entirely consistent because the second silylation reaction for each such pair might also be hindered. Nevertheless the introduction of additional configurations of silanols in the model would introduce additional parameters that could not be estimated from the available measurements.

4.6 Conclusions

The mechanism and kinetics of silylation by $SiCl_4$ and subsequent hydrolysis of porous Vycor were investigated at 400–600°C by thermogravimetric analysis. In addition to the silylation of surface hydroxyl groups and the subsequent hydrolysis of chloride groups, condensation reactions between a surface chloride with a silanol and between two silanols contribute to the overall reaction.

The silanols can be approximately classified as isolated and vicinal or paired, with the latter being the more abundant. After reaction of the first silanol of a pair with gaseous $SiCl_4$, the second -OH can either combine with a second gaseous $SiCl_4$ or condense with the already attached -$SiCl_3$ group. The competition between these two sterically hindered and slow reactions controls the overall extent of silylation.

A kinetic model postulating two types of silanols and including the silylation, hydrolysis, and condensation steps gave good agreement with the TGA data after appropriate adjustment of its parameters. The classification of silanols into two groups is viewed as a drastic approximation appropriate to the limited data available.

Nomenclature

A Interfacial area of the sample layer, cm^2

a_i Concentration of the initial surface -OH groups, mole/g

b_i Concentration of the initial surface -Cl groups, mole/g

c_o Concentration of the reactant in fluid flow, $mole/cm^3$

c_s Concentration of the reactant at the sample surface, $mole/cm^3$

D_{AB} Mass diffusivity of the reactant in N_2, cm^2/min

D_{eff} Effective diffusivity for intraparticle diffusion, cm_2/min

D_k Knudsen diffusion coefficient, cm^2/min

k_c Mean mass transfer coefficient, cm/min

k_i Reaction rate constants, $cm^3/(mole\ min)$ or min^{-1}

L Length of the sample pan, cm

M Molecular weight, g/mole

Nu_L Mean Nusselt number for a flat plate

n_i Number of initial surface -OH groups per surface area, nm^{-2}

R Gas constant, erg/(mole K)

R_p Particle radius, cm

Re_L Mean Reynolds number for a flat plate

$\overline{r}$ Average pore diameter, cm

Sc Schmidt number

T Temperature, K

t Time, minute

t_p Starting time of purge, minute

W Weight of the Vycor sample during the reaction, g

W_o Initial weight of the unreacted Vycor sample, g

w_i Weight factor for chlorination, g/mole

w_{Hi} Weight factor for hydrolysis, g/mole

x_i Concentration of the surface groups in hydrolysis process, mole/g

y_i Concentration of the surface groups in chlorination process, mole/g

ϵ Void fraction

ϕ Thiele Modulus for intraparticle diffusion

η Effectiveness factor

ρ Apparent density of porous Vycor, g/cm^3

τ Empirical tortuosity factor

Acknowledgements

The authors appreciate the funding of this work by the department of Energy under the University Coal Research Program, Grant DE-FG22-92PC92525.

References

1. Plueddemann, E. P., "Chemistry of Silane Coupling Agents," *Silylated Surfaces*, (D. E. Leyden and W. T. Collins, Eds.), Gordon and Breach, New York (1977).

2. Leyden, D. E., *Silanes, Surfaces, and Interfaces*, Gordon and Breach, New York (1986).

3. Evans, B. and T. E. White, "Adsorption and Reaction of Methylchlorosilanes at an "Aerosil" Surface," *J. Catal.*, **11**, 336 (1968).

4. Armistead, C. G., A. J. Tyler, F. H. Hambleton, S. A. Mitchell, and J. A. Hockey, "The Surface Hydroxylation of Silica," *J. Phys. Chem.*, **73**, 3947 (1969).

5. Hair, M. L. and W. Hertl, "Reactions of Chlorosilanes with Silica Surfaces," *J. Phys. Chem.*, **72**, 2372 (1969).

6. Hockey, J. A. and B. A. Pethica, "Surface Hydration of Silicas," *Trans. Faraday Soc.*, **57**, 2247 (1961).

7. Peri, J. B., "Infrared Study of OH and NH_2 Groups on the Surface of a Dry Silica Aerogel, *J. Phys. Chem.*, **70**, 2937 (1966).

8. Morrow, B. A. and I. A. Cody, "Infrared Studies of Reactions on Oxide Surfaces. 5. Lewis Acid Sites on Dehydroxylated Silica," *J. Phys. Chem.*, **80**, 1995 (1976).

9. Hoffmann, P. and E. Knözinger, "Novel Aspects of Mid and Far IR Fourier Spectroscopy Applied to Surface and Adsorption Studies on SiO_2," *Surface Sci.*, **188**, 181 (1987).

10. Tsapatsis, M., S. Kim, S. W. Nam, and G. Gavalas, "Synthesis of Hydrogen Permselective SiO_2, TiO_2, Al_2O_3, and B_2O_3 Membranes from the Chloride Precursors," *Ind. Eng. Chem. Res.*, **30**, 2152 (1991).

11. Tsapatsis, M. and G. R. Gavalas, "A Kinetic Model of Membrane Formation by CVD of SiO_2 and Al_2O_3," *AIChE J.*, **38**, 847 (1992).

12. Peri, J. B. and A. L. Hensley, Jr., "The Surface Structure of Silica Gel," *J. Phys. Chem.*, **72**, 2926 (1968).

13. Danielson, P., "Silica," *Kirk-Othmer Encyclopedia of Chemical Technology*, Vol. 20, p. 782 (1980).

14. Welty, J. R., C. E. Wicks, and R. E. Wilson, *Fundamentals of Momentum, Heat, and Mass Transfer*, p. 600, John Wiley & Sons, New York (1983).

15. Bird, R. B., W. E. Stewart, and R. N. Lightfoot, *Transport Phenomena*, p. 511, John Wiley & Sons, New York (1960).

Table 4.1 Weight changes in various parts of reaction cycle for samples pretreated at different temperatures.

Pretreatment T	Reaction T	Reaction time	S $+\Delta m$ %	P $-\Delta m$ %	H $-\Delta m$ %	P $-\Delta m$ %
800°C	600°C	2 min	2.4	0.53	0.66	0.13
600°C	600°C	2 min	4.4	0.56	1.67	0.14
600°C	450°C	6 min	4.6	0.15	2.03	0.29
450°C	450°C	6 min	5.5	0.26	2.43	0.38

S = silylation; P = purge; H = hydrolysis

Table 4.2 Constants and parameters used in the model calculation.

	Silylation			Hydrolysis		
T(°C)	400	450	500	400	450	500
c_o, $\frac{mole}{cm^3}$	1.63×10^{-6}	1.52×10^{-6}	1.42×10^{-6}	1.45×10^{-6}	1.35×10^{-6}	1.26×10^{-6}
D_{eff}, $\frac{cm^2}{min}$	2.32×10^{-2}	2.40×10^{-2}	2.48×10^{-2}	7.12×10^{-2}	7.38×10^{-2}	7.63×10^{-2}
k_c, $\frac{cm}{min}$	20.24	21.57	22.87	46.24	50.27	54.32
n_1, nm^{-2}	0.172	0.172	0.172	0.96	1.029	1.049
n_2, nm^{-2}	0.644	0.644	0.644	0.893	0.955	0.974
k_1, $\frac{cm^3}{mole\text{-}min}$	3.97×10^5	1.41×10^6	7.04×10^6	1.89×10^5	4.97×10^5	1.30×10^6
k_2, min^{-1}	0.01	0.03	0.08	0.01	0.03	0.08
k_3, $\frac{cm^3}{mole\text{-}min}$	3.31×10^4	6.39×10^4	1.41×10^5	1.89×10^5	4.97×10^5	1.30×10^6
k_4, min^{-1}	–	–	–	0.005	0.01	0.018

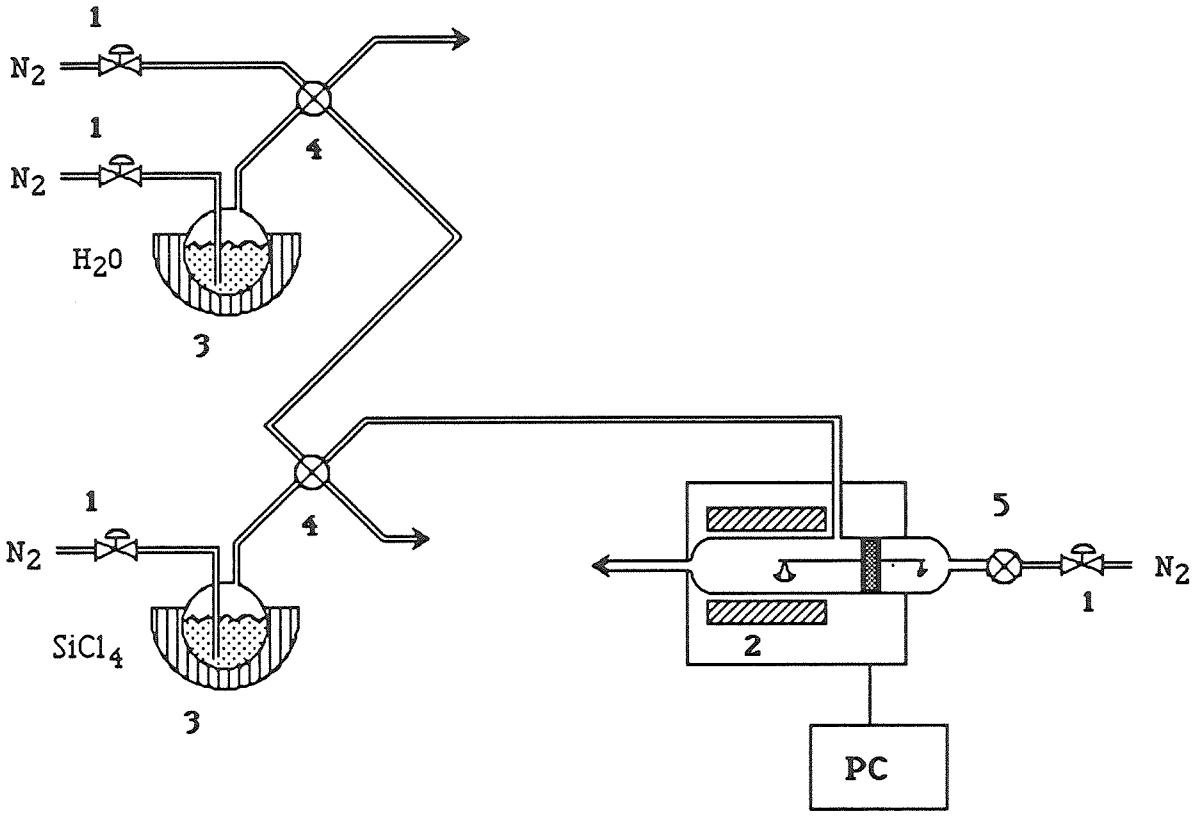

Figure 4.1 Schematic diagram of TGA system. 1, mass flowmeter with valve; 2, furnace with temperature controller; 3, bubbler with heating element and temperature controller; 4, four-way valve; 5, on-off valve.

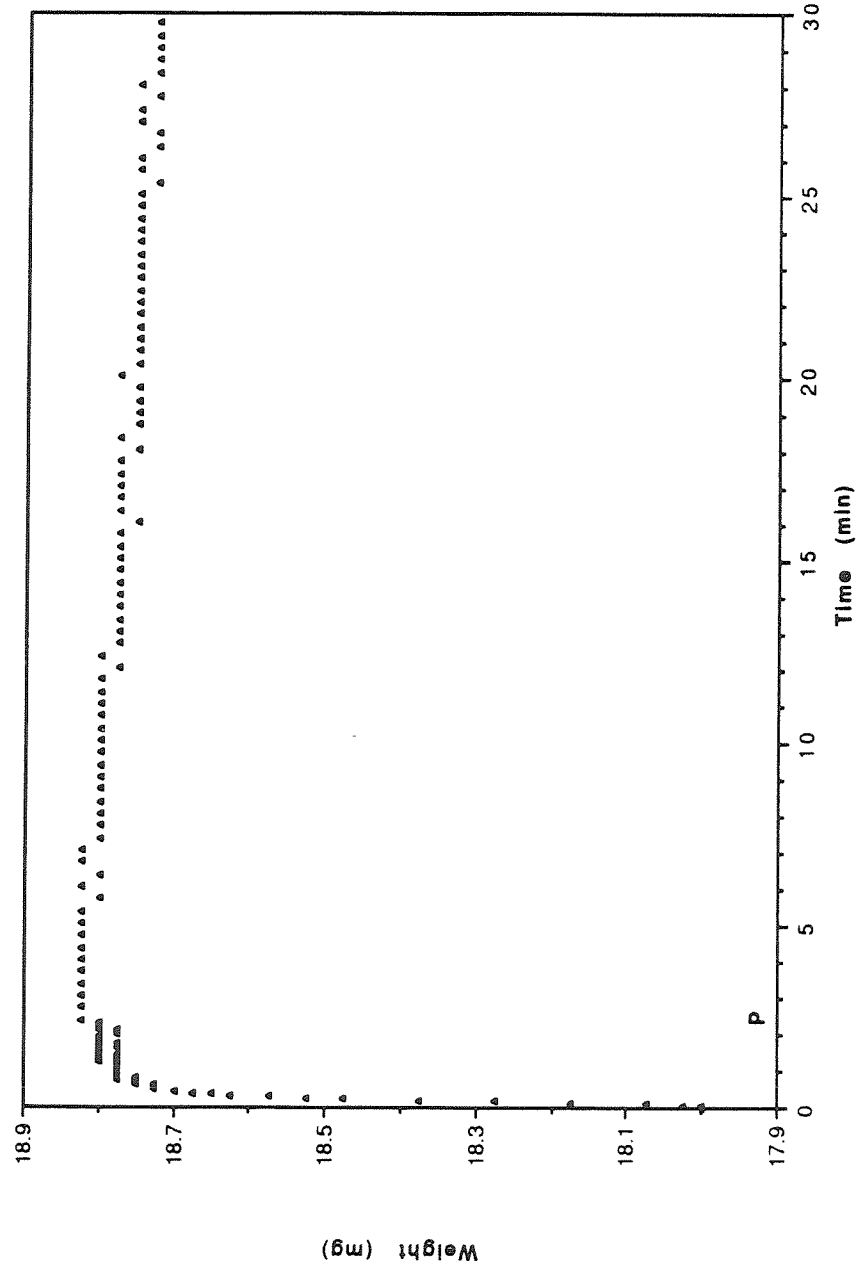

Figure 4.2 Weight of sample V600 during first reaction with 9% $SiCl_4$-N_2 at 600°C and subsequent purge at the same temperature. Point P indicates the beginning of purge period.

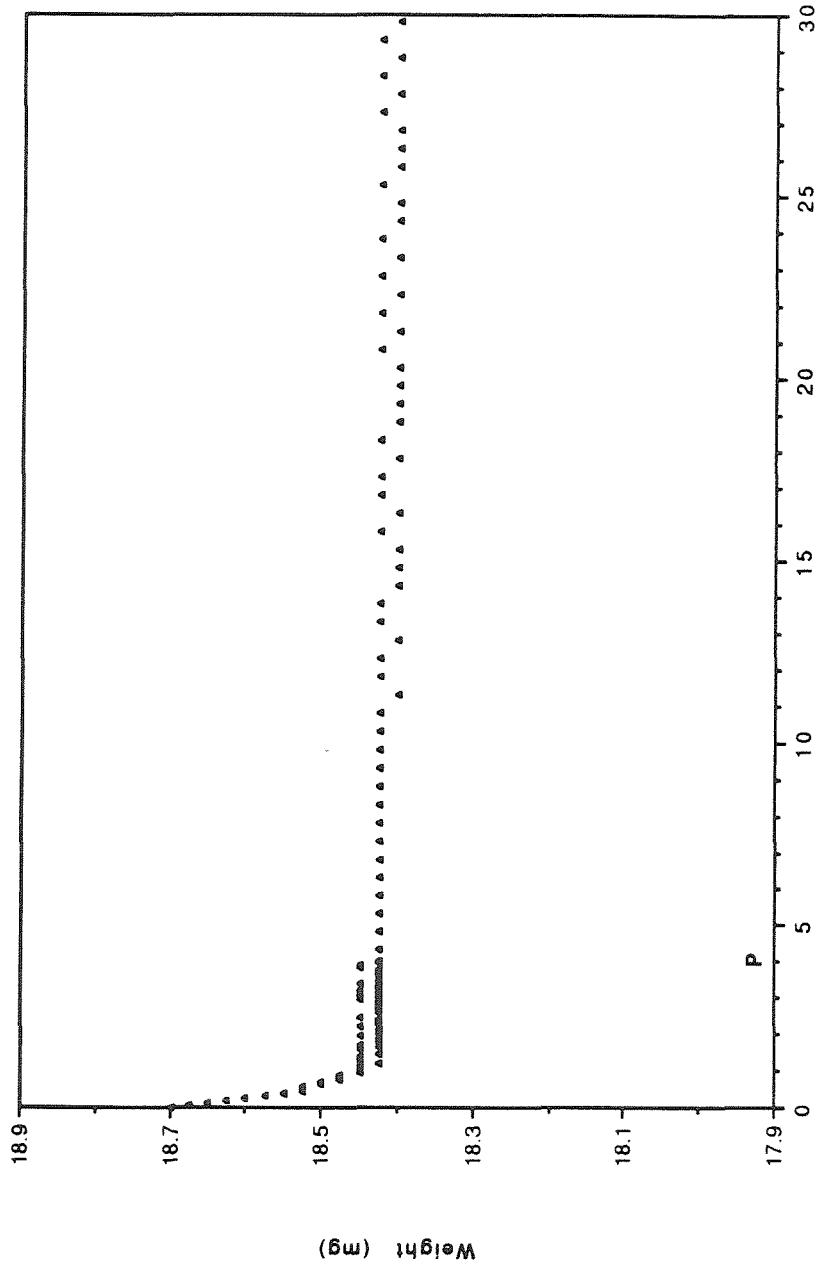

Figure 4.3 Weight of sample V600 prereacted as in Figure 2 during reaction with 7% H_2O-N_2 and subsequent purge at 600°C. Point P indicates the beginning of purge period.

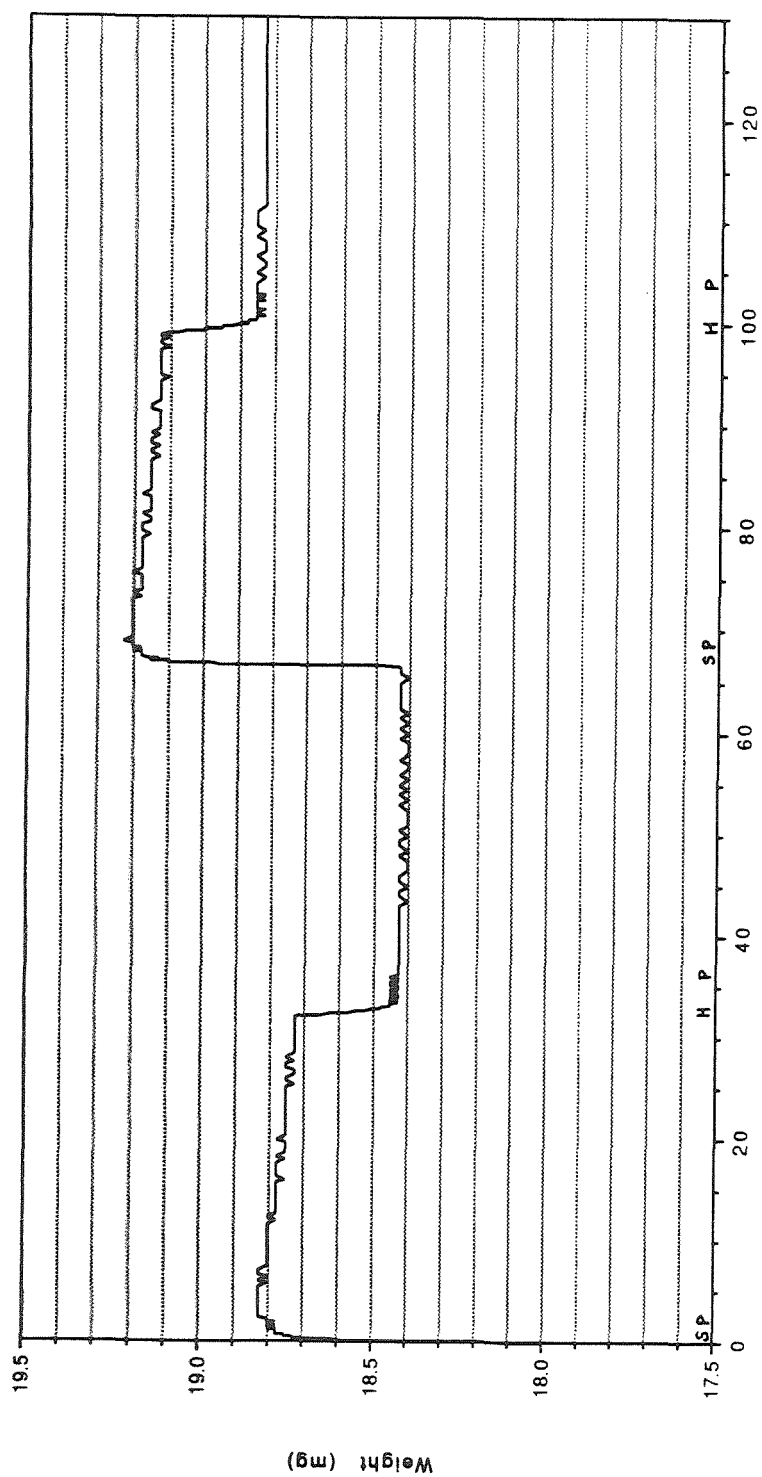

Figure 4.4 Weight of sample V600 during two cycles of reaction with 9% $SiCl_4$-N_2 at 600°C and subsequent purge with N_2, and hydrolysis with 7% H_2O-N_2 at the same temperature. Point S indicates start of silylation, P indicates termination of $SiCl_4$ or H_2O flow and beginning of purge period, and H signifies start of hydrolysis.

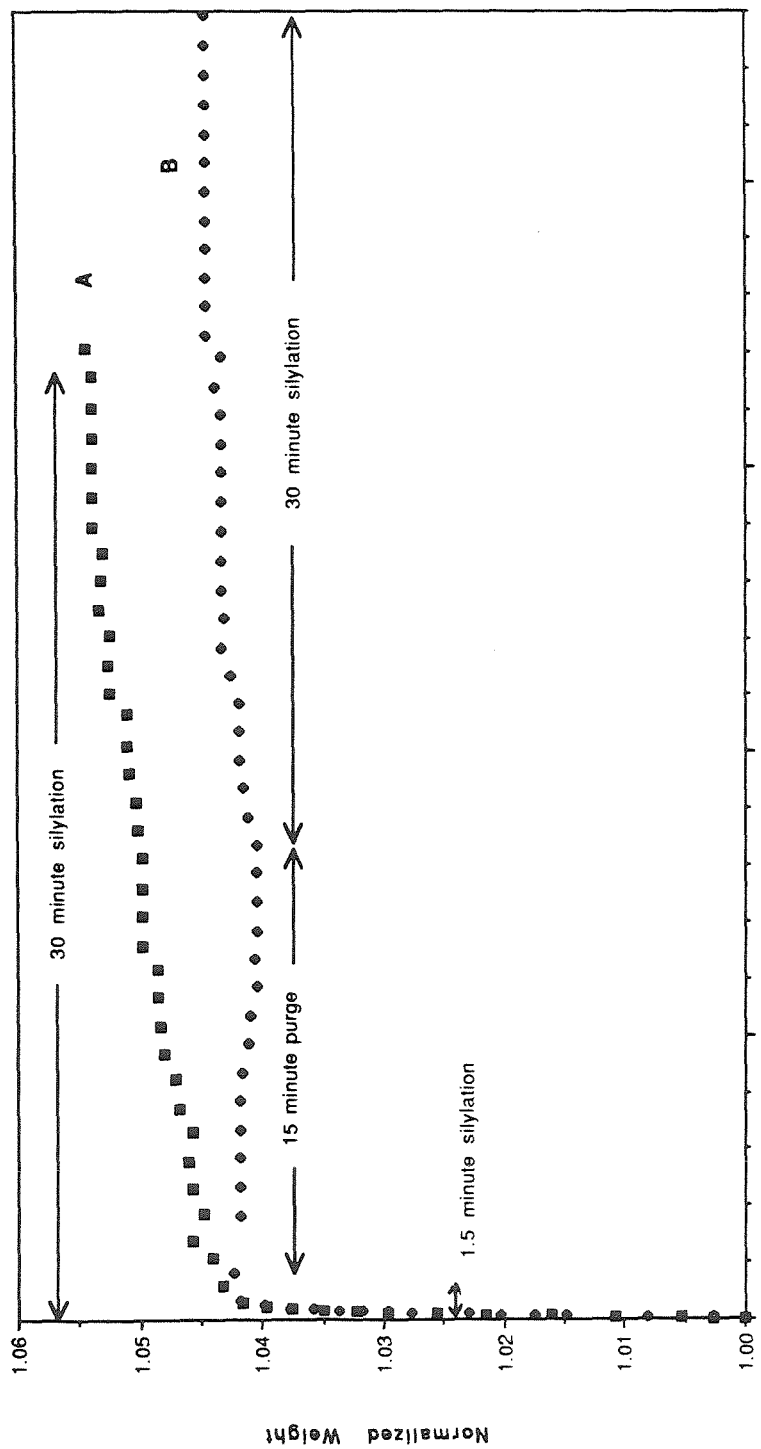

Figure 4.5 Comparison of two silylation experiments of V600 at 600°C with 9% $SiCl_4$-N_2. A: 30 min continuous silylation and B: 1.5 min silylation followed by 15 min purge followed by 30 min silylation.

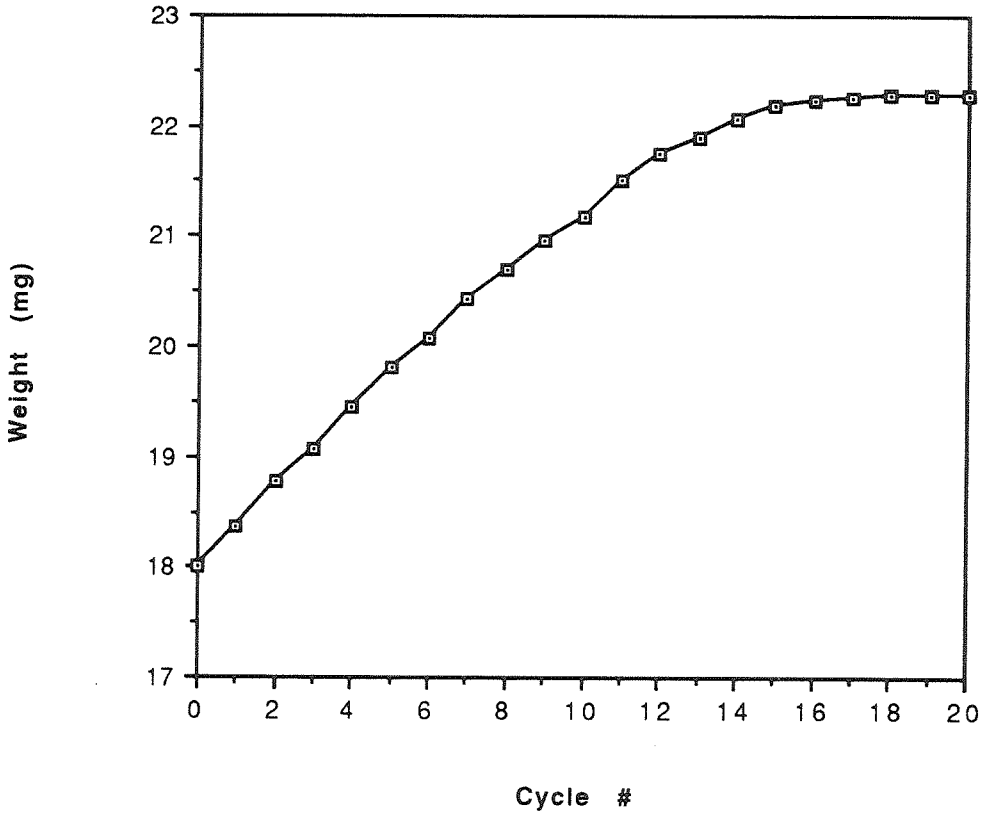

Figure 4.6 Weight of V600 during 20 consecutive cycles of silylation, purge, hydrolysis, and purge of 600°C. Reactions were carried out under the conditions of Figure 4.4.

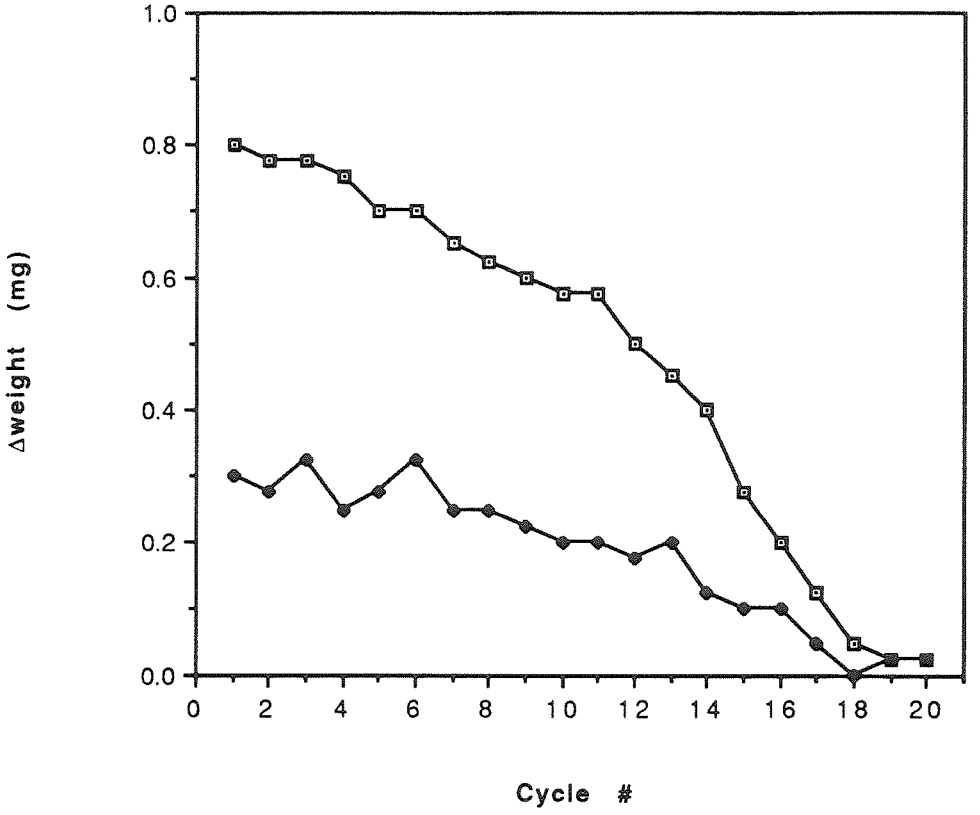

Figure 4.7 Weight change of V600 for each of the 20 consecutive cycles of silylation(□) and hydrolysis(●) of 600°C. For silylation Δweight is positive. For hydrolysis Δweight is negative.

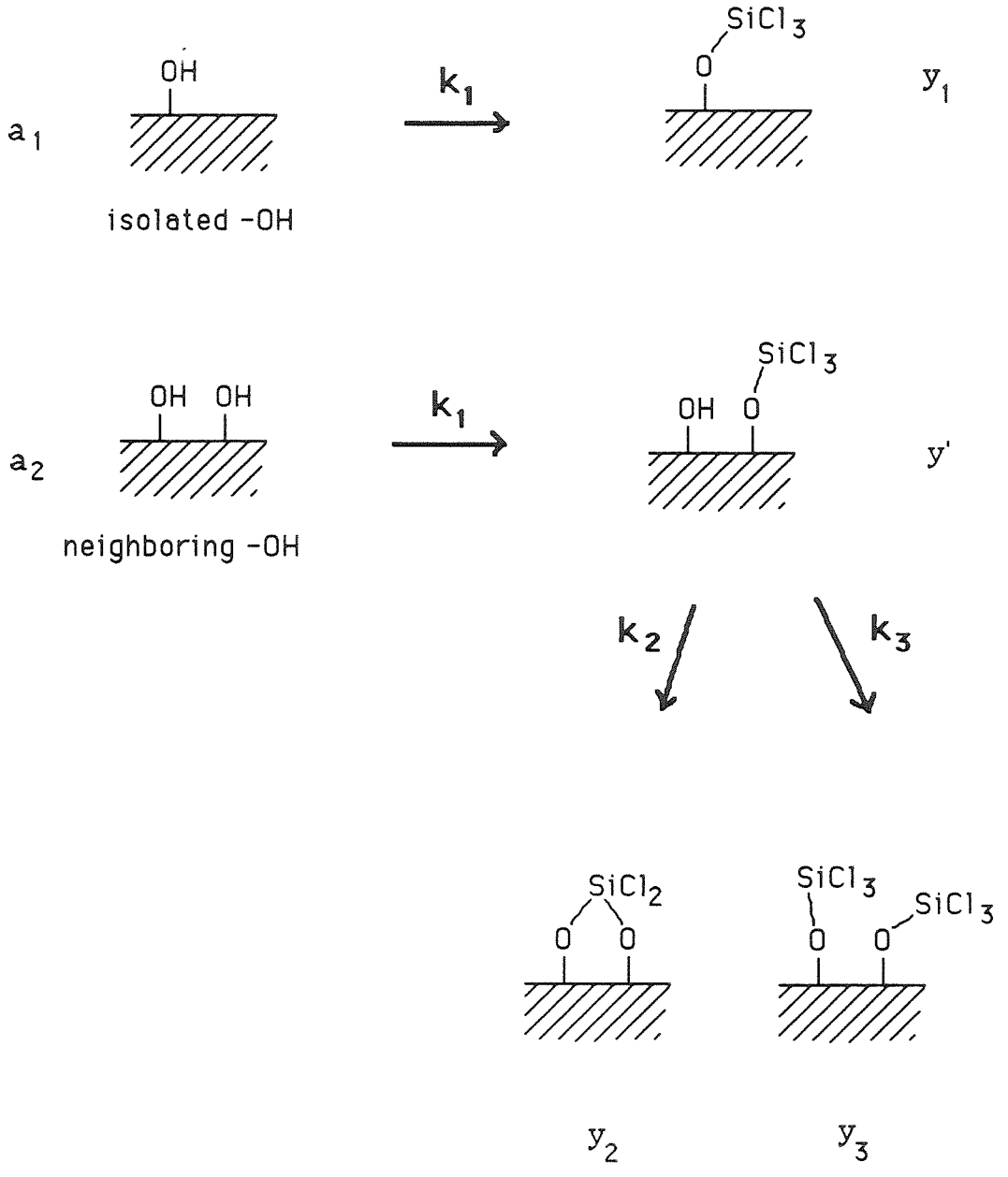

Figure 4.8 Kinetic model of the reaction network during silylation.

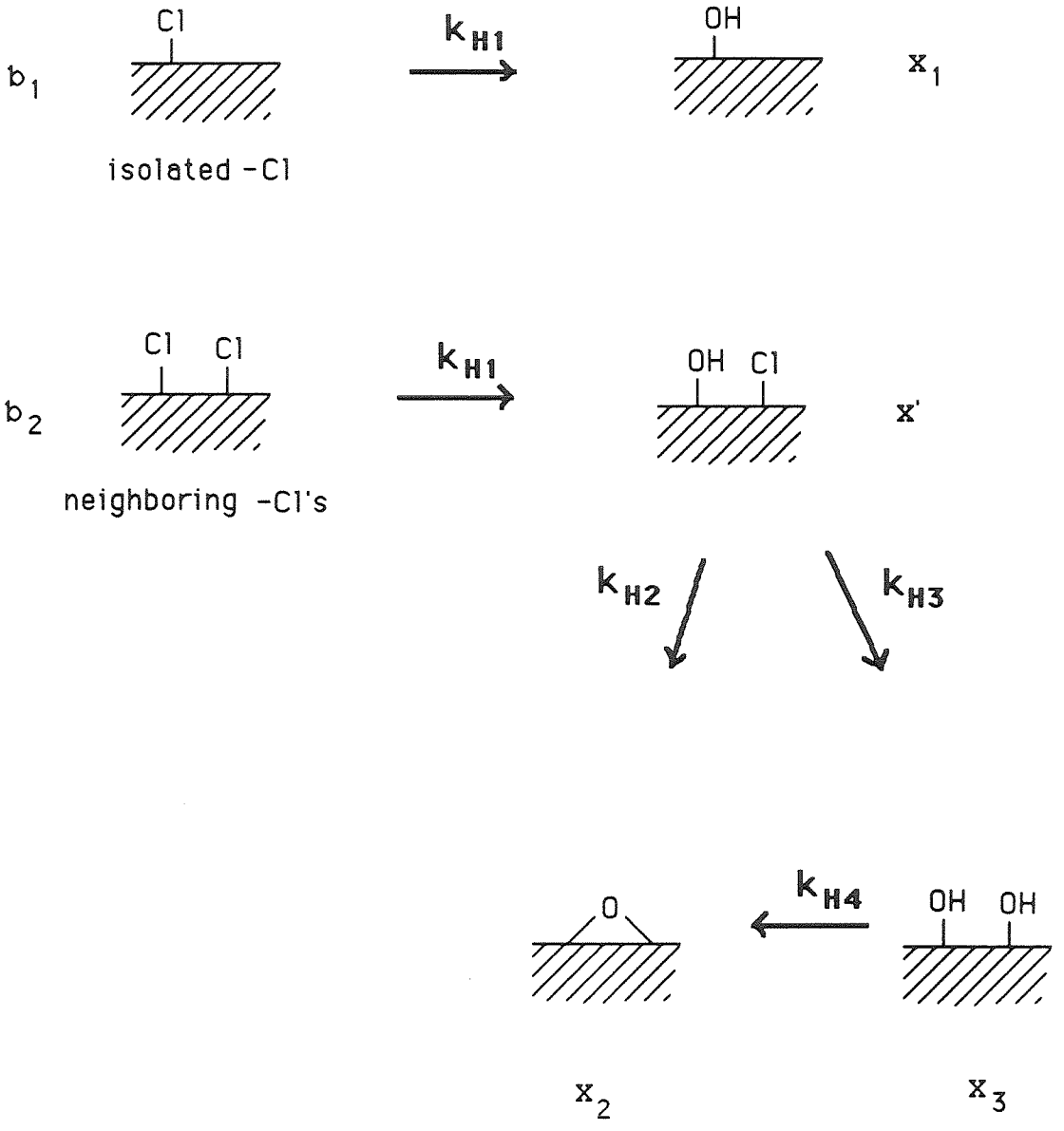

Figure 4.9 Kinetic model of the reaction network during hydrolysis

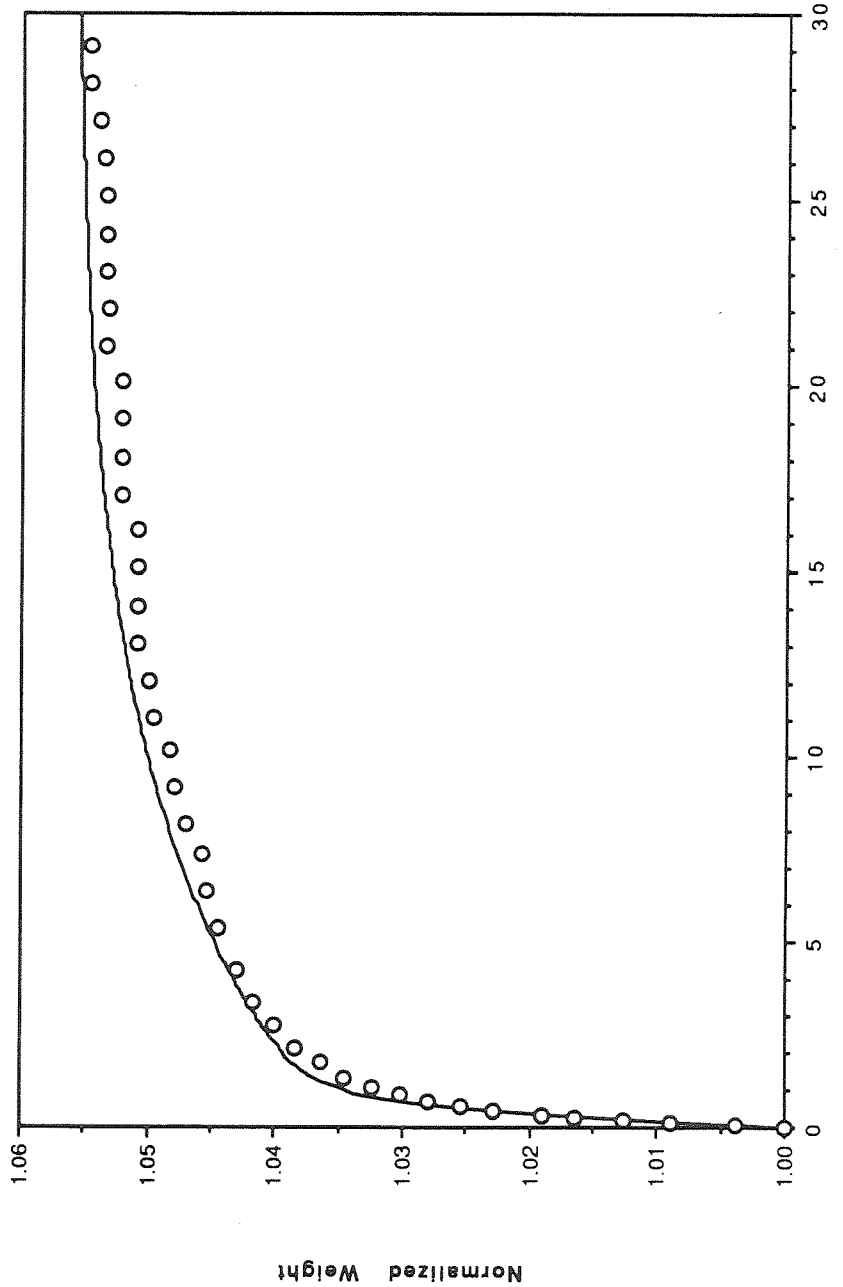

Figure 4.10 Experimental data points and model calculation (solid curve) for silylation of V600 for 30 min at 450°C.

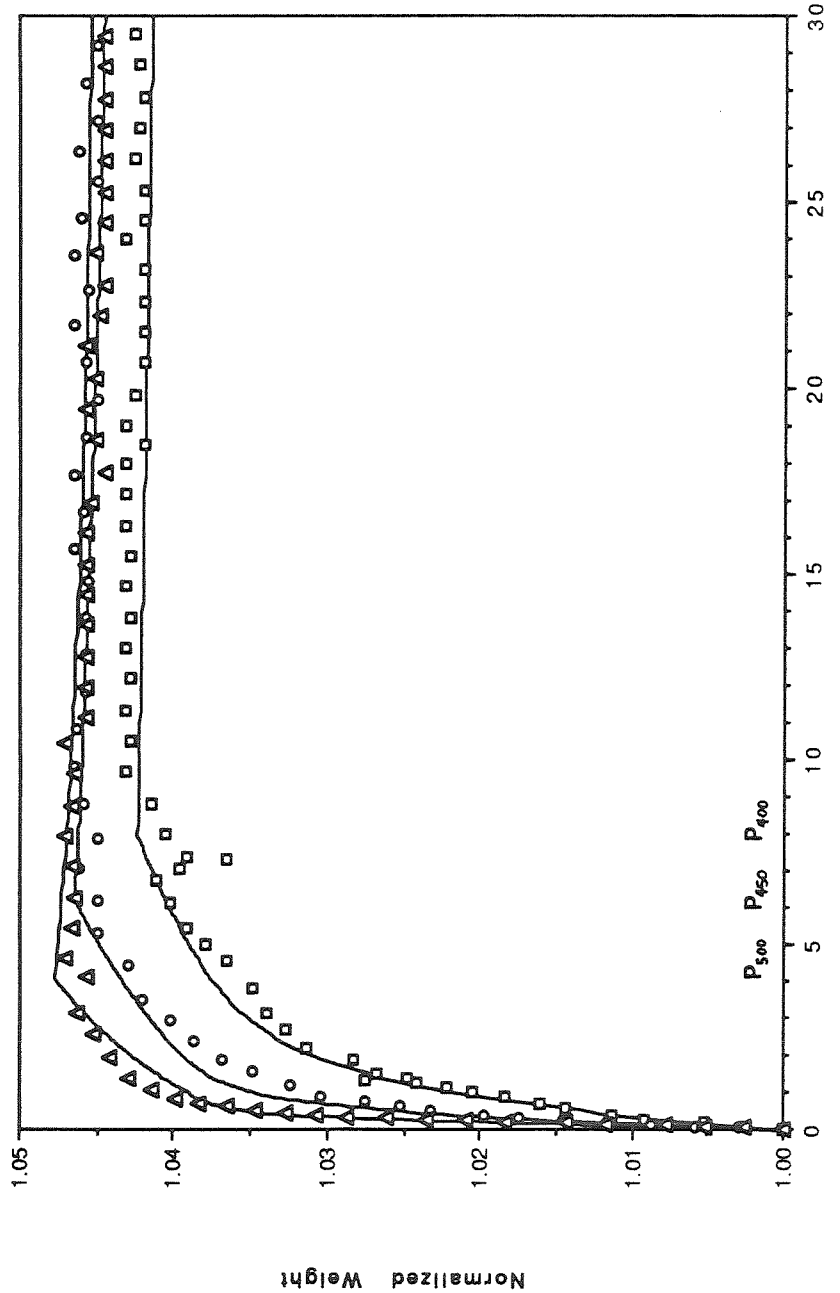

Figure 4.11 Experimental data points and model calculations (solid curve) for silylation at 400°C (□), 450°C (○), and 500°C (△) and subsequent purge at the same temperature. Point P indicates the beginning of the purge period.

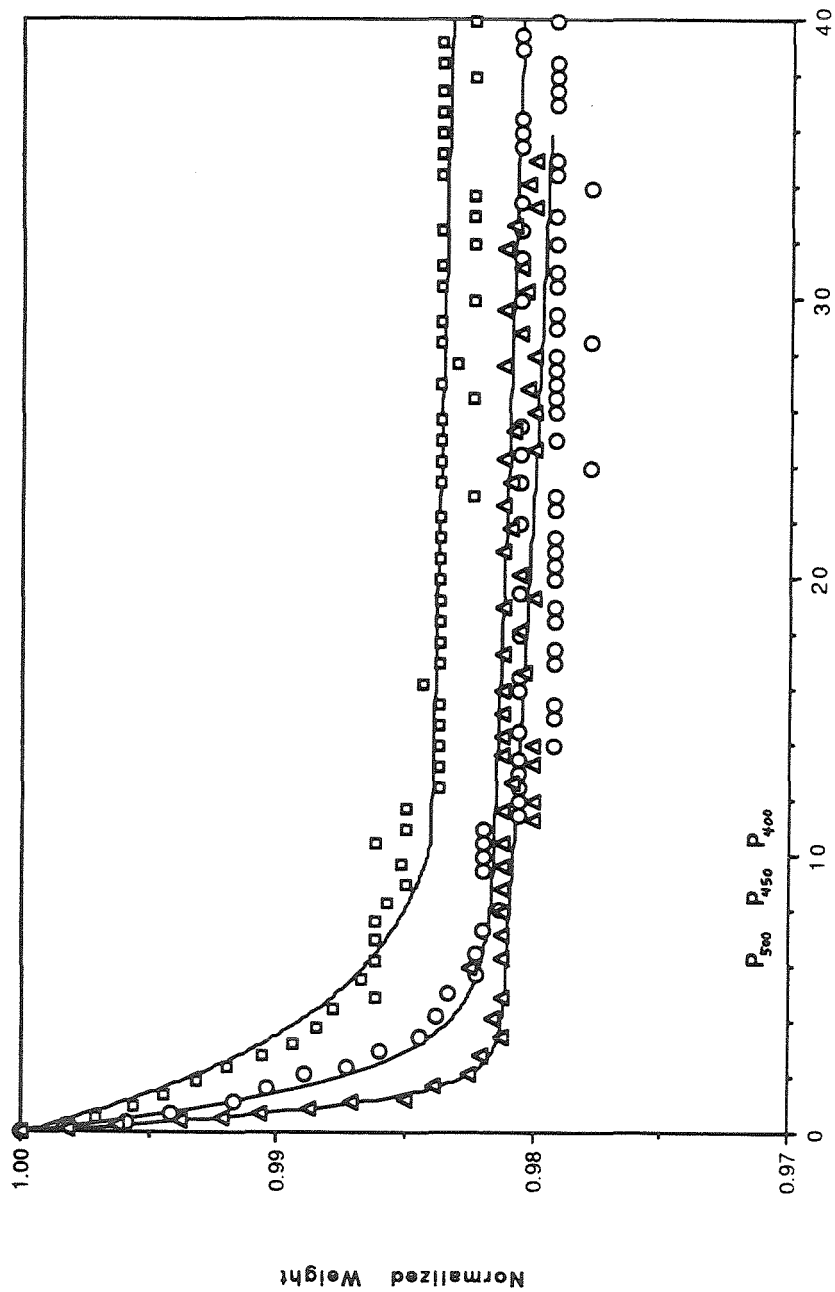

Figure 4.12 Experimental data points and model calculations (solid curve) for hydrolysis of precacted samples as specified in Figure 4.11 at 400°C (□), 450°C (○), and 500°C (△) and subsequent purge at the same temperature. Point P indicates the beginning of the purge period.

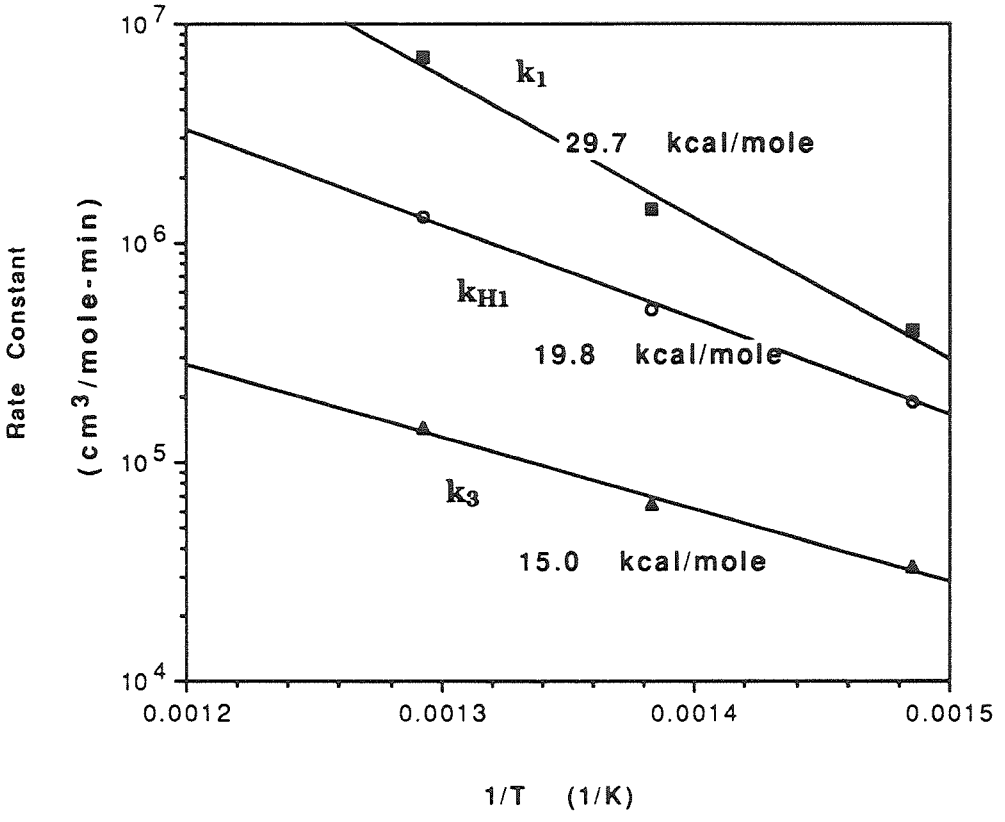

Figure 4.13 Arrhenius plots and activation energy values of the rate constants, k_1, k_{H1}, and k_3.

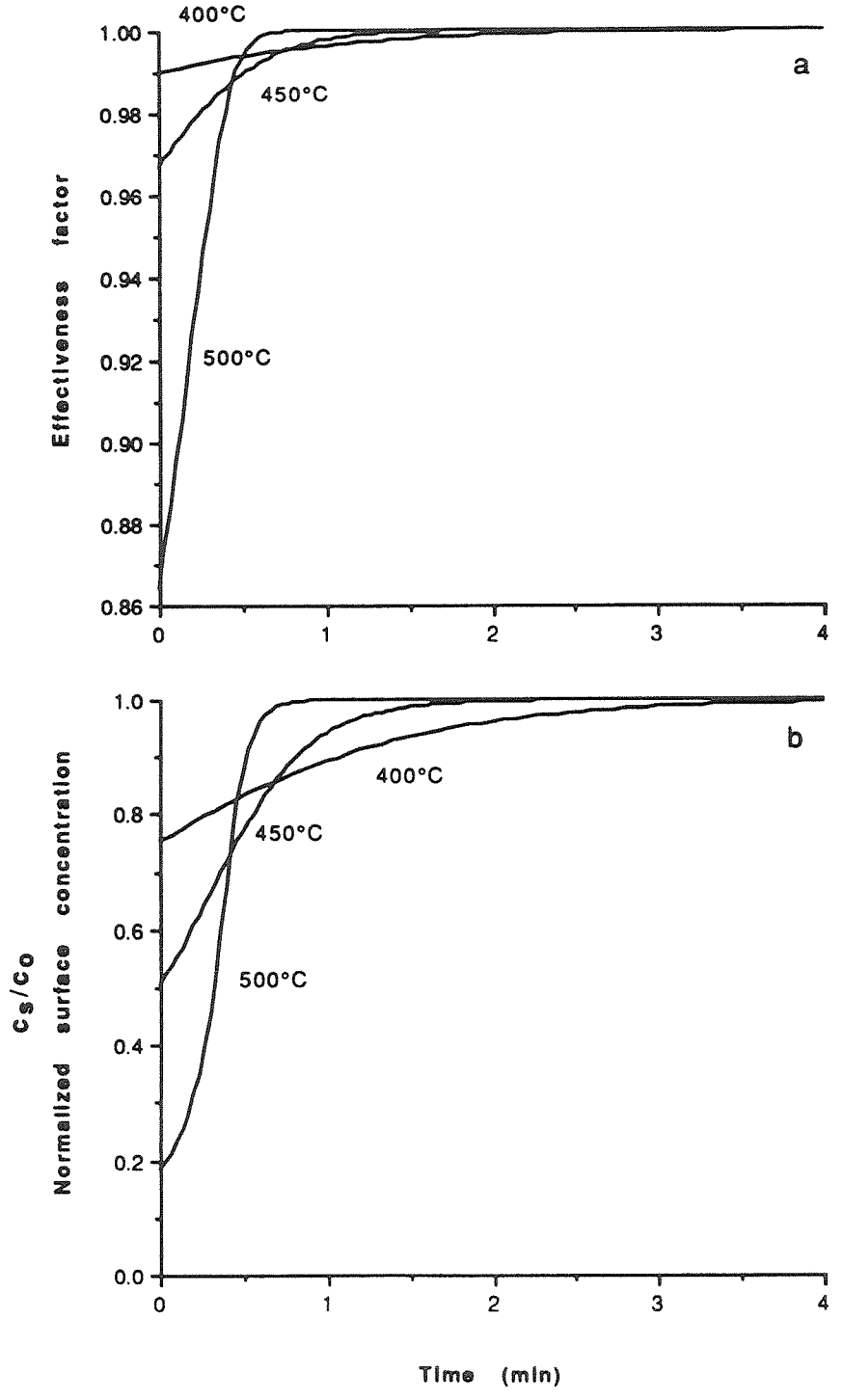

Figure 4.14 (a) Effectiveness factor and (b) normalized surface concentration calculations for silylation.

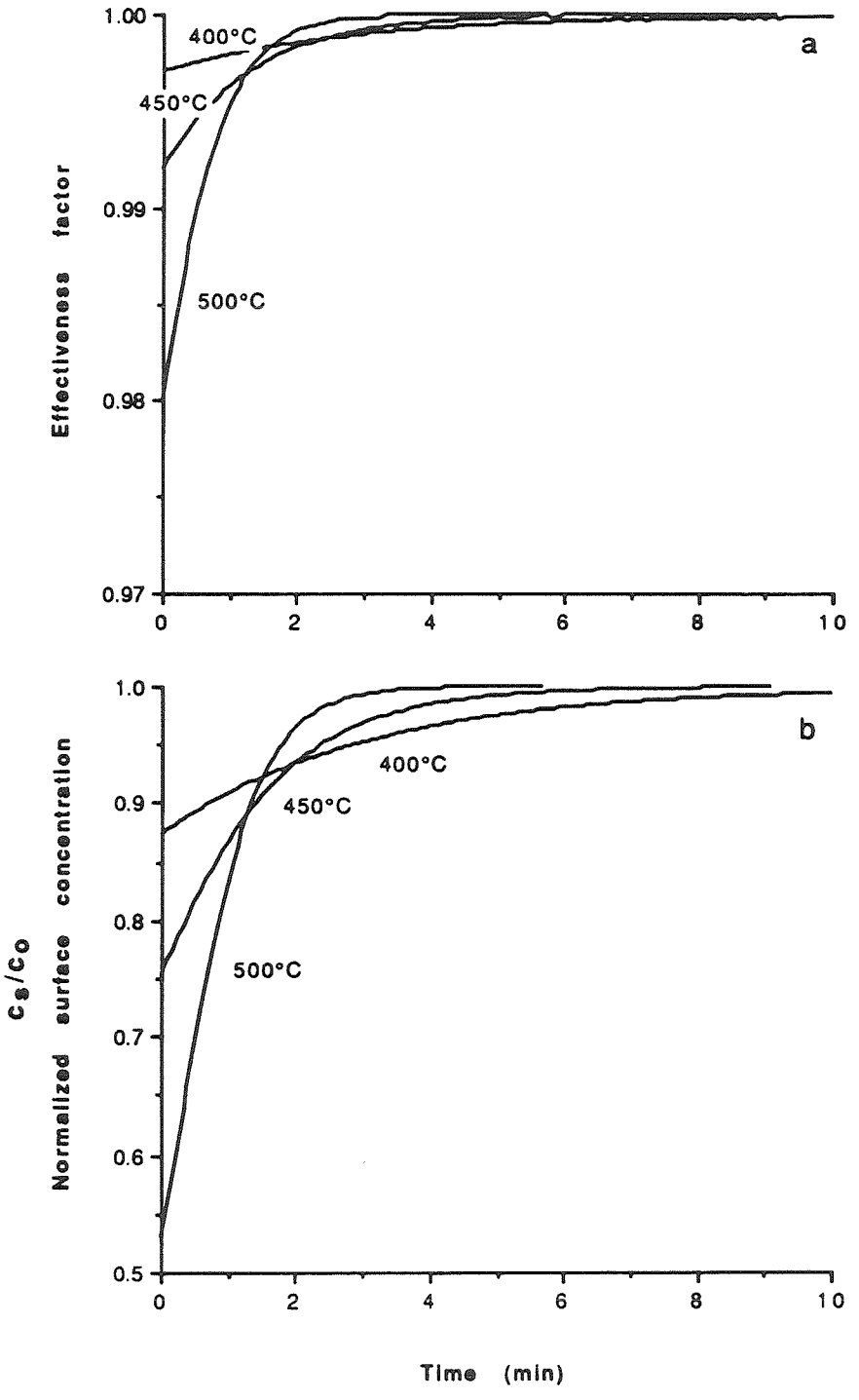

Figure 4.15 (a) Effectiveness factor and (b) normalized surface concentration calculations for hydrolysis.

Chapter V

Atomic Layering of Permselective SiO_2 Films, Characterization and Modeling

Submitted to *I&EC Research.*

Abstract

Thin SiO_2 layers were deposited on the surface of porous Vycor glass by alternating vapor phase reaction with $SiCl_4$ and H_2O. The membranes prepared by this technique had H_2 permeance of 0.3–0.4 $cm^3(STP)/(min \cdot cm^2 \cdot atm)$ and H_2:N_2 selectivity of 500–1000 at 600°C. The $SiCl_4$ dosage at each silylation cycle, the concentration of initial surface -OH groups, and the reaction temperature influence significantly the deposit layer thickness. After two weeks of heating at 550°C under 3 atmospheres of water vapor, the membrane H_2 permeance decreased by about 20%, and the selectivity increased to more than 2000. The membrane properties after this hydrothermal treatment are superior to those of membranes prepared earlier by one-sided (steady flow) deposition. A simple model incorporating diffusion and surface reaction was used to study the effect of various parameters on the formation of the deposit layer.

5.1 Introduction

Inorganic membranes have potential for improving the efficiency of high temperature chemical processes; in membrane-reactor configuration, combining reaction and product separation can greatly increase conversion [1,2]. Hydrogen permselective membranes, in particular, have potential applications in several large volume catalytic processes such as water gas shift reaction, dehydrogenation of hydrocarbons, and hydrogen sulfide decomposition [3–5].

Various amorphous oxides are known to be highly selective to H_2 permeation due to small molecular size of H_2 [6,7]. Amorphous silica (dense), for example, has hydrogen permeability 1.6×10^{-10} $\frac{cm^3(STP)\cdot cm}{cm^2\cdot s\cdot cmHg}$ and H_2:N_2 permeability ratio above 10^5 at 500°C. Because of the very low permeability membranes made of silica or other dense oxides need to have a composite structure comprising a thin layer of the selective oxide material supported on a much thicker porous substrate that provides mechanical strength.

Thin oxide layers can be prepared by chemical vapor deposition (CVD) on porous substrates. Using CVD, the desired films can be prepared at high temperatures obviating the drying and calcination required in film formation by liquid-phase techniques. As is well known, the removal of solvent or condensation products accompanying drying and calcination often causes shrinking and crack formation [8,9]. Thus, films produced by CVD are generally denser and more uniform than those produced by liquid-phase techniques.

CVD of amorphous silica membranes has been pursued by several investigators. In previous work we have employed hydrolysis of chlorosilane compounds at 600–800°C to prepare SiO_2 membranes supported on porous Vycor tubes [10]. The two reactants (e.g., $SiCl_4$ and H_2O) were passed at steady flow either at op-

posite sides of the tube wall (opposing-reactants geometry) or at the same side of the tube wall (one-sided geometry). One-sided deposition gave thinner and, therefore, more permeable layers on account of a more favorable balance between reaction and diffusion. Silica membranes have also been prepared by low pressure oxidation of triisopropylsilane [11] and by pyrolysis of tetraethylorthosilicate [12].

The formation of silica from chlorosilanes and water vapor involves reaction of the chlorosilane with surface hydroxyls (silylation reaction), hydrolysis of the surface chloride groups, and hydroxyl-hydroxyl and hydroxyl-chloride condensation, all proceeding simultaneously according to the following mechanism [10,13]:

$$\text{Si-OH (s)} + \text{SiCl}_4\text{ (g)} \rightarrow \text{Si-O-SiCl}_3\text{ (s)} + \text{HCl (g)} \quad (1)$$

$$\text{Si-O-SiCl}_3\text{ (s)} + 3\text{H}_2\text{O (g)} \rightarrow \text{Si-O-Si(OH)}_3\text{ (s)} + 3\text{HCl (g)} \quad (2)$$

$$\text{Si-OH (s)} + \text{Si-OH (s)} \rightarrow \text{Si-O-Si (s)} + \text{H}_2\text{O (g)} \quad (3)$$

$$\text{Si-OH (s)} + \text{Si-Cl (s)} \rightarrow \text{Si-O-Si (s)} + \text{HCl (g)} \quad (4)$$

Kinetic studies [13] have shown that the reaction of chlorosilanes with surface hydroxyls is very rapid at temperatures above 600°C. As desirable as the high rate is for producing a thin deposit layer, the fast depletion of the chlorosilane reactant causes significant concentration gradients along the axial direction when the support is a long tube or capillary. The longer the tube, the more severe this mass transfer limitation, resulting in nonuniform thickness along the length of the tube with the upstream part overdeposited to ensure adequate deposition in the downstream part. Overdeposition causes problems of reduced overall H_2 permeance and stability. When deposition is prolonged beyond the time required for pore plugging, the deposit layer continues to grow outside of the pores. This external growth occurs by deposition of particles formed in the gas phase as well as by the

heterogeneous mechanism (1)–(4). Regardless of the mechanism, a thick external layer lowers the permeance and can also cause thermomechanical stresses leading to crack formation [14]. Using low concentrations of $SiCl_4$ to minimize the homogeneous particle formation would accentuate concentration gradients especially if this technique were to be applied to the fabrication of multi-tube membrane modules. A more practical means of minimizing homogeneous particle formation and deposition gradients is, therefore, desirable.

Particle formation in the gas phase can be eliminated by flowing the chlorosilane and water vapor past the support surface alternatingly rather than simultaneously. This alternating deployment of reactants is well known in electronic device fabrication and sometimes referred to as atomic layer epitaxy [15,16]. Compared to simultaneous flow of the reactants, atomic layering provides strict control of the stoichiometry but is much slower. Atomic layering is particularly attractive for self-limiting reactions when after exhaustion of the surface active sites, the surface becomes "saturated" and the reaction stops. Extending the flow of the reactants beyond saturation will not have any further effect. After surface saturation by the first reactant, flow is switched to the second reactant until once more saturation occurs, completing one reaction cycle. Several consecutive reaction cycles are necessary to build up a layer of the desired thickness. Atomic layer epitaxy by means of self-limiting reactions has been used to deposit GaAs films [17].

In electronic device fabrication deposition takes place over a nonporous substrate. By contrast, in membrane preparation deposition is carried out over a porous substrate. In the latter case it is undesirable to continue reactant flow in any given cycle until the whole pore surface becomes saturated, for then the deposit layer would be formed throughout the thickness of the substrate and the resulting structure would be useless as a membrane. To limit the thickness of the

deposition layer it is necessary to change one half of the reaction cycle from continuous flow until saturation to a limited dosage of the reactant. For this purpose, the reactor volume above the substrate surface is evacuated, a metered dosage of the first reactant (e.g., $SiCl_4$) is admitted, and the volume is isolated. Reaction then proceeds not until surface saturation but until exhaustion of the reactant. Under these conditions the depth of penetration within the porous matrix is limited both by the reactant dosage and by the balance between the reaction and diffusion coefficients. The other half cycle involving reaction with H_2O need not be limited in dosage or time; it can be conducted by continuous flow, for the reactant can only react with the surface chloride groups resulting from the first part of the cycle.

It may be argued that admitting a limited dosage of the first reactant is equivalent to passing a steady flow of the reactant for a limited time. This would indeed be the case in the absence of longitudinal concentration gradients. However, admitting a dosage of the reactant to an evacuated space takes place very rapidly so that reaction subsequently proceeds uniformly over the external surface of the substrate.

In this paper we report experimental results on the preparation of silica membranes using the atomic layer epitaxy method modified to control the reactant dosage as described above, which we shall simply call "alternating reactant deposition." We also present a simple model used to explore the effect of reactant dosage, number of cycles, and other deposition parameters.

5.2 Experimental Techniques

A schematic of the apparatus for membrane deposition and permeation mea-

surements is shown in Figure 5.1. The reactor consisted of a quartz tube of 11 mm ID containing a concentric Vycor tube (7 mm OD, 4.8 mm ID, and 4 nm mean pore diameter) secured by vacuum tight fittings. The porous Vycor tubes were supplied by Corning, Inc. A new Vycor tube was used in each experiment. The tube consisted of a porous section welded on the one side or from both sides to nonporous sections. The porous Vycor tubes were supplied by Corning, Inc. The reactor was placed inside a tubular furnace with a temperature controller. The reactants $SiCl_4$ and H_2O were carried by N_2 gas from bubblers maintained at appropriate temperatures. In the arrangement shown in Figure 5.1, the Vycor tube was welded on one side to a nonporous section and sealed at the other side. In this geometry the reactants could only be admitted in the annular space between the Vycor tube and the larger quartz tube, and the deposit layer was formed in the pores below the external surface of the Vycor tube. In other experiments, the Vycor tube was welded on both sides to nonporous segments, and the reactants were admitted in the bore of the tube to form a layer on the inside surface.

Before each deposition experiment the porous Vycor tube in place in the reactor was heated slowly to 600°C and kept for a few hours under flow of a N_2-O_2 mixture for a few hours to remove adsorbed water and organic impurities. The reactor was then heated up to the reaction temperature of 700°C or 800°C.

Each membrane preparation experiment consisted of a number of cycles, each cycle comprising silylation, purge with N_2, hydrolysis, and another purge. For each cycle, the reactor was first evacuated while the storage bulb (1000 ml) was filled with 7% of $SiCl_4$ in N_2 at atmospheric pressure by steady flow from the bubbler. The storage bulb was then isolated from the flow and connected to the evacuated reaction chamber for a few seconds. The $SiCl_4/N_2$ mixture instantly filled the reactor, and after one or two seconds the valve was closed to isolate the reactor.

The reaction was allowed to progress for 1 minute after which the reactor was purged for 1 minute with dry N_2. Subsequently a stream of 100 cm^3/min of 10% H_2O-N_2 was passed through the reactor at atmospheric pressure for 5 minutes. The reactor was then purged once more for 5 minutes with dry N_2 to remove H_2O from the flow lines and the reactor surfaces.

After every 1 or 2 cycles, the permeation rate of N_2 was measured by the technique described in a previous paper [10]. The cycles of silylation and hydrolysis were repeated until the permeation rate of N_2 dropped to approximately one hundredth of its original value. At this point the permeation of H_2 and N_2 was measured at several temperatures.

For some experiments, the tubes were subjected to intermittent hydrothermal treatments during deposition. The tubes were exposed to flow of 10% H_2O in N_2 at the deposition temperature for 5–10 hours between some cycles. The purpose of the intermittent treatment was to allow the deposit layers densify sufficiently before the final deposition and thus avoid uncontrollable densification in subsequent hydrothermal annealing.

5.3 Experimental Results and Discussion

Figure 5.2 shows the evolution of permeance with successive reaction cycles for two experiments using support tubes of different length. SiO_2 layers were deposited on the outside surface of the support tubes at 700°C. The permeance of N_2 decreased slowly during the first several cycles, rapidly during the next few cycles, and again slowly during the final cycles. While the permeance of N_2 decreased by approximately a factor of 100, the permeance of H_2 decreased by only 20–40% from its original value, depending on reactant dosage and number of

cycles. The final permeances of H_2 and N_2 from these two experiments are listed in Table 5.1.

After deposition the two tubes were exposed to flow of 10% H_2O in N_2 at 700°C and atmospheric pressure for one day. This treatment caused approximately 8% decline in the permeance of H_2 and 50% decline in the permeance of N_2. The permeances of H_2 and N_2 after the treatment are shown by dotted lines in Figure 5.2 and are also listed in Table 5.1. This decrease of permeance during hydrothermal treatment can be attributed to densification of the deposit structure catalyzed by H_2O as discussed in our previous reports [14,18,19].

It is noted that the Membranes 1 and 2 described by Figure 5.2 and Table 5.1 were prepared with different $SiCl_4$ dosages, $0.62\mu mol/cm^2$ and $0.33\mu mol/cm^2$, respectively. Membrane 2 prepared with the smaller dosage required a greater number of cycles to attain pore plugging. Clearly, with the smaller amount of $SiCl_4$ per unit surface area per cycle, the reactant was depleted faster thereby requiring more cycles to complete pore plugging. It was also observed that the H_2 permeance as well as the H_2:N_2 selectivity was higher for the membrane prepared with the smaller dosage, indicating a thinner deposit layer.

The same trend is observed when comparing Membrane 1 (Figure 5.2) with Membrane 3 (Figure 5.3), the latter prepared by deposition on the inner wall of the support tube. The $SiCl_4$ dosage was lower ($0.28\mu mol/cm^2$) for Membrane 3, requiring a larger number of cycles to reach pore plugging (23 versus 16) and producing a membrane of higher H_2 permeance as shown in Tables 5.1 and 5.2a. The final H_2:N_2 selectivity is also higher for Membrane 3. These results suggest that decreasing the $SiCl_4$ dosage during silylation results in a thinner deposit layer and higher H_2 permeance. Immediately after deposition, the effect of dosage on H_2 permeance is rather weak because the resistance to permeation due to the deposit

layer is a relatively small fraction of the total resistance, but this effect becomes more pronounced after hydrothermal treatment which increases the resistance of the deposit layer.

The two experiments described by Figure 5.3 were carried out using the same dosages per cycle and varied only by the deposition temperature. In this two experiments, intermittent hydrothermal treatment was interposed every few cycles as described in the experimental procedure section. Figure 5.3 shows step declines of N_2 permeance after each of the hydrothermal treatments conducted after the 10th, 17th, and 23rd cycle for Membrane 3, and after the 9th and 15th cycle for Membrane 4. These decreases were relatively small in the earlier cycles and increased in the later cycles. The small change in early cycles was expected, since early during deposition the deposit layer makes a small contribution to the overall resistance. However, the direction of change at the early cycles was unexpected. With a small volume of deposit and with N_2 permeance at 90% of its original value, the pore cross sections should have been largely open. Shrinkage of the deposit should have increased rather than decreased the open pore cross section. One possible explanation for the decrease of permeance is that the deposit grows in a cluster-like or "tree-like" fashion rather than as a smooth layer. Hydrothermal treatment under these conditions could lead to cross-linking, reducing rather than increasing the open cross section. Yet, more complete understanding of the structural effect of hydrothermal treatment is necessary to fully explain the changes of the N_2 permeance.

Because of these decreases of N_2 permeance, Membrane 3 required only 23 cycles to attain N_2 permeance 1/30 of its original value, whereas Membrane 2, prepared without interposed hydrothermal treatments, required 27 cycles to reach a similar level, even though the dosage was lower for Membrane 3 (0.28 μmol/cm^2

vs. 0.33 μmol/cm^2). Prepared with the smaller dosage and fewer cycles, Membrane 3 contained much thinner and more permeable deposit layer, as indicated by permeance data in the tables.

At 800°C silylation was much faster than at 700°C, thus the reaction was confined to a thinner layer. For equal number of cycles the total amount of deposit was the same at both temperatures, but at 800°C the deposit was distributed over a thinner region resulting in a higher diffusion resistance. Therefore, at 800°C the permeance of N_2 decreased more rapidly, and pore plugging was achieved with fewer total cycles. By the same reasoning, the final deposit layer of the membrane produced at 800°C was probably thinner. Although Table 5.2a shows the initial H_2:N_2 selectivity of the membrane prepared at 800°C to be higher than that of the 700°C membrane, the H_2 permeance of the 800°C membrane was lower. The lower H_2 permeance of the membrane prepared at 800°C can be attributed to the higher density of the deposit layer due to the higher temperature employed throughout each deposition cycle and throughout the interposed hydrothermal treatments. The increase of the densification rate with temperature has been known from previous work [18]. The increased deposit density at 800°C is also reflected in the activation energies listed in Table 5.4. Immediately after deposition Membrane 4 (prepared at 800°C) had much higher activation energies than Membrane 3 (prepared at 700°C), although the activation energies reached a common value after a long hydrothermal treatment, as will be described shortly.

After deposition, Membranes 3 and 4 were annealed at 550°C under 3 atm of H_2O (and 7 atm of N_2) for several days. The changes in the gas permeances during this treatment are listed in Table 5.2a. The H_2 permeance at 700°C and 800°C decreased by at most 13% after 15 days of the treatment. At the lower temperature of measurement (450°C) the decrease was slightly larger because the activation

energy of the permeance increased after the treatment. The permeances listed in Table 5.2a are the result of in-series combination of the resistances of the support tube and the deposit layer. To examine the properties of the deposit layer by itself we subtracted the resistance of the support tube and recalculated the permeances as described in the Appendix. The results are listed in Table 5.3. The activation energies for the H_2 permeances of the deposit layers in Membranes 3 and 4, excluding the resistances of the support tube, are listed in Table 5.4. The activation energies of the two membranes for H_2 permeance were quite different initially but reached similar values, about 26 kJ/mol, after 15 days of the hydrothermal treatment. It is noted that Membrane 4 with lower initial activation energy underwent a sharper permeance decline by the hydrothermal treatment. The final activation energy of 26 kJ/mol reached after the hydrothermal treatment is somewhat lower than the activation energy, 30–32 kJ/mol, of nonporous Vycor [7]. This difference is easily explained by the nonuniform structure of the deposit layer consisting of in-series resistances of a thin region with no open pore paths followed by a thicker region of gradually increasing pore size. Even the thin region has some residual closed porosity which tends to lower the activation energy [13,14].

Activation energies for N_2 permeance are not presented in Table 5.4 because the measurements of the very small N_2 permeances were inaccurate especially at the lower temperature (450°C). Any small leaks in the system could cause significant error in the permeance measurements.

To compare the membranes prepared in this study with membranes prepared by one-sided deposition and subjected to the same hydrothermal treatment, selected data from a previous study [14] are reproduced in Table 5.2b. After 21 days of the treatment, the membrane prepared by one-sided deposition showed a 70% decrease of its H_2 permeance which reached 0.11 $cm^3(STP)/(min \cdot cm^2 \cdot atm)$ at

600°C. On the other hand, the membranes prepared by alternating reactants deposition had final H_2 permeances of 0.28–0.30 $cm^3(STP)/(min \cdot cm^2 \cdot atm)$ at 600°C after 15 days of the treatment. The membrane produced by one-sided deposition had lower initial activation energy before the treatment (10–15 kJ/mol [14]). The final activation energies for H_2 permeance were the same for the two types of membranes, suggesting that the difference in the H_2 permeance is due to a difference in thickness rather than the state of densification. The same trend was previously observed in the comparison of Membranes 3 and 4 in which the membrane with the higher initial activation energy underwent a smaller decrease of H_2 permeance after the treatment.

In view of the diffusion-limited nature of the deposition reaction, the deposit layer is expected to be spatially nonuniform with its density monotonically decreasing from the boundary towards the interior. To measure the profile density one could, in principle, use electron microprobe analysis (EMA). Unfortunately for SiO_2 deposition on porous Vycor (96+% SiO_2), small variations in the substrate porosity near the boundary superimposed on measurement error made the deposit density measurement very unreliable. To obtain some idea of the deposit density profile, we carried out TiO_2 deposition using alternating reaction with $TiCl_4$ and H_2O. In this instance, measurement of the TiO_2/SiO_2 ratio is much more reliable. Figure 5.4 shows the mass ratio of TiO_2 to the SiO_2 substrate as calculated from an EMA linescan over the tube cross section. The Ti density decreases sharply with depth and declines to zero within 6μm. In previous thermogravimetric studies we had found the $TiCl_4$ reaction with -OH groups on Vycor to be slower (about 5 times at 600°C) than the corresponding reaction with $SiCl_4$. Consequently, the density profile of the SiO_2 deposit should be sharper with total thickness perhaps about 3μm, on account of the inverse square root dependence of the depth of

reactant penetration on the reaction rate constant.

5.4 Model Description

The purpose of the calculations described below was to obtain a semiquantitative understanding of the effect of reactant dosage and other parameters on the deposit layer thickness and to identify the most important for membrane optimization. To describe the growth of the deposit layer it was sufficient to treat only the silylation part of the cycle when new material was added on the deposit. The role of the hydrolysis part of the cycle is to regenerate the -OH groups after each silylation. For each silylation period diffusion and reaction can be described by the equations:

$$\frac{\partial}{\partial z}\left(D_{eff}\frac{\partial C_{si}}{\partial z}\right) = kC_{si}C_{oh} \tag{5}$$

$$\frac{\partial C_{oh}}{\partial t} = -k\,C_{si}\,C_{oh} \tag{6}$$

$$V\left(\frac{dC_g}{dt}\right) = A\left(D_{eff}\left(\frac{\partial C_{si}}{\partial z}\right)\right)_{z=0} \tag{7}$$

with the initial and boundary conditions:

$$z = 0 : C_{si} = C_g(t)$$

$$z \to \infty : C_{si} \to 0, \quad C_{si} \to 0$$

$$t = 0 : C_{oh} = m_o\,S(\epsilon), \quad C_g = C_{bo}$$

where C_{si} and C_{oh} are the molar concentrations of gaseous $SiCl_4$ and surface -OH groups per unit total volume of the material, respectively, C_g is the bulk concentration of gaseous $SiCl_4$ in the reaction chamber, D_{eff} is the effective diffusivity

of $SiCl_4$ in the porous medium, V is the volume of tube bore or annulus containing the $SiCl_4$ reactant, A is the surface area of the reaction boundary (inside or outside cylindrical surface), m_o is the concentration of initial -OH groups per unit pore surface area, and $S(\epsilon)$ is the pore surface area per unit total volume of the porous material.

The plane geometry used in Equation (5) and the boundary condition at $z \to \infty$ are justified by the very small deposit layer thickness compared to the wall thickness (3μm versus 1100μm). In the formulation of Equation (5) the gas-phase accumulation term was omitted because of the small ratio, $\frac{C_{bo}}{m_o S(\epsilon)}$ (less than 0.01). The reaction was assumed to be 1st order in the concentration of gaseous $SiCl_4$ and in the concentration of -OH groups in the solid. The resistance due to external mass transfer of $SiCl_4$ in the radial direction was neglected because of the short diffusion path. Whether the reactant was introduced in the bore of the tube or in the annulus, the diffusion path in the radial direction was 2–2.5mm. With the binary diffusivity of $SiCl_4$ in N_2 at the reaction temperature of 700°C being about 0.6 cm^2/sec [20], the characteristic time for diffusion was only 0.07 sec compared to the reaction time of several seconds.

During each hydrolysis and the succeeding purge all -Cl groups are replaced by -OH groups. At the same time condensation reactions between two -OH groups and between -OH and -Cl reduce the concentration of the -OH groups available to the following silylation period. Since the time allowed to the hydrolysis and purge periods was held constant from cycle to cycle, it was assumed that the surface concentration of -OH groups was the same at the beginning of each cycle. However, since the deposit layer thickness and, hence, the surface area changed from cycle to cycle, the volumetric concentration of -OH groups also changed. Moreover, since the deposit layer thickness after the first cycle became a function

of position, the volumetric concentration of -OH was also a function of position.

At the beginning of the first cycle the diffusivity was spatially uniform, but as the deposit layer developed with repeated cycles, D_{eff} developed a spatial dependence. During each cycle the deposit growth was limited to a fraction of a monolayer, therefore, the change of $D_{eff}(x)$ was very small for the duration of any single cycle. Thus to simplify the calculations, D_{eff} was treated as a function of x, independent of time, during each cycle. Likewise, the void fraction, ϵ, the local average pore radius, r, and the surface area, S, were treated as functions of x, independent of time, during any single cycle. The equations were solved repeatedly for successive cycles, and at the end of each cycle new profiles of D_{eff}, ϵ, r and S were calculated according to the amount of deposit accumulated during the cycle. More specifically, the local void fraction was calculated using the relation,

$$\epsilon(x) = \epsilon_{no}(x) - v_s\, k \int_0^{t_p} C_{si}\, C_{oh}\, dt \tag{8}$$

where ϵ_{no} is the void fraction at the beginning of the cycle, v_s is the molar volume of the deposit, and t_p is the silylation time of each cycle.

The average local pore radius was related to the void fraction based on the random capillary model [21]:

$$r(x) = \sqrt{\frac{1}{-2\pi\lambda}\ln(1-\epsilon)}\,. \tag{9}$$

The surface area per unit volume, S, can also be calculated from the random capillary model as follows:

$$S(x) = -\frac{d\epsilon}{dr} = 4\pi\lambda\,(1-\epsilon)\,r. \tag{10}$$

Finally, the material deposited in each cycle (in moles per unit total volume of the support) can be expressed as

$$C_d(x) = C_{do}(x) + k \int_0^{t_p} C_{si}\, C_{oh}\, dt \tag{11}$$

where C_{do} is the value of C_d at the beginning of the cycle.

The diffusion of $SiCl_4$ is assumed to be in the Knudsen regime so that

$$D_{eff} = \frac{2}{3\tau}\sqrt{\frac{8\,R\,T}{M}}\,\epsilon\,r \tag{12}$$

where τ is an empirical tortuosity factor taken as 3. In the calculation of $D_{eff}(x)$, the pore radius, $r(x)$, was corrected by subtracting the kinetic radius of $SiCl_4$ (Lennard-Jones diameter, 5.78Å [22]). For the calculation of the N_2 flux performed at the end of each cycle, the diffusivity was calculated correcting pore radius by the kinetic diameter of N_2 (Lennard-Jones diameter, 3.68Å).

5.5 Transformation of Equations

Introducing the dimensionless variables and parameters,

$$c = \frac{C_{si}}{C_{bo}} \qquad s = \frac{C_{oh}}{m_o\,S(\epsilon_{no})}$$

$$c_b = \frac{C_g}{C_{bo}} \qquad x = \frac{z}{L}$$

$$D = \frac{D_{eff}(\epsilon_{no})}{D_{eff}(\epsilon_o)} \qquad \sigma = \frac{S(\epsilon_{no})}{S(\epsilon_o)}$$

$$\Phi^2 = \frac{L^2\,k\,m_o\,S(\epsilon_o)}{D_{eff}(\epsilon_o)} \qquad b = k\,C_{bo}$$

equations (5)–(7) become:

$$\frac{\partial}{\partial x}\left(D\frac{\partial c}{\partial x}\right) = \Phi^2\,\sigma\,c\,s \tag{13}$$

$$\frac{\partial s}{\partial t} = -b\,c\,s \tag{14}$$

$$\frac{dc_b}{dt} = \frac{A\,D_o}{V\,L}\left(D\frac{\partial c}{\partial x}\right)_{x=0} \tag{15}$$

with the initial and boundary conditions:

$$x = 0: \quad c = c_b(t)$$

$$x \to \infty: \quad c \to 0, \quad \frac{\partial c}{\partial x} \to 0$$

$$t = 0: \quad s(x) = 1, \quad c_b = 1$$

where

$$D_o = D_{eff}(\epsilon_o).$$

The above system of partial differential equations in x and t can be greatly simplified by a well known transformation [23] using the dependent variable,

$$C(x,t) = \int_0^t c(x,t')\, dt'. \tag{16}$$

To this end, Equation (14) is divided by s and integrated with respect to t to obtain

$$s = \exp(-b\, C). \tag{17}$$

On the other hand, direct integration of Equation (14) gives

$$s = 1 - b \int_0^t c\, s\, dt'$$

so that

$$\int_0^t c\, s\, dt' = \frac{1}{b}\big[1 - \exp(-b\, C)\big]. \tag{18}$$

Integrating now Equation (13) with respect to t and using Equation (18) yield an equation in C as the dependent variable, i.e.,

$$\frac{\partial}{\partial x}\left(D \frac{\partial C}{\partial x}\right) = \frac{\Phi^2\, \sigma}{b}\big(1 - \exp(-b\, C)\big) \tag{19}$$

with the boundary conditions:

$$x = 0 : C = C_b = \int_0^t c_b \, dt'$$

$$x \to \infty : C \to 0, \quad \frac{\partial C}{\partial x} \to 0.$$

To obtain an expression for C_b we integrate equation (15) once with respect to t:

$$\frac{dC_b}{dt} = 1 + \frac{A\,D_o}{V\,L}\left(D\frac{dC}{dx}\right)_{x=0} \tag{20}$$

with the initial condition:

$$t = 0 : C_b = 0, \quad c_b = 1.$$

Equations (13)–(15) have been reduced to two coupled ordinary differential equations one in x, the other in t.

In preparation for a numerical solution, Equation (19) is rewritten as a system of two first-order equations:

$$\frac{dC}{dx} = \frac{y}{D} \tag{21}$$

$$\frac{dy}{dx} = \frac{\Phi^2\,\sigma}{b}\big(1 - \exp(-b\,C)\big) \tag{22}$$

with the boundary conditions:

$$x = 0 : C = C_b$$

$$x \to \infty : C \to 0, \quad y \to 0.$$

For sufficiently large values of x, i.e., away from the reaction layer, D is uniformly equal to 1, and Equations (21) and (22) can be analytically solved for y in terms of C as follows. Equation (22) is rewritten with C as the independent variable, i.e.,

$$\frac{dy}{dC}\,\frac{dC}{dx} = \frac{dy}{dC}\,\frac{y}{D} = \frac{\Phi^2\,\sigma}{b}\big(1 - \exp(-b\,C)\big)$$

and then integrated from $x \to \infty$ to $x = x_o$ where x_o is sufficiently large that D and σ are equal to 1 in (x_o, ∞). The result is

$$y_o = \frac{\Phi^2}{b}\left[\left(2\big(b\,C_o + \exp(-b\,C_o) - 1\big)\right)\right]^{1/2} \tag{23}$$

where $y_o = y(x_o, t)$ and $C_o = C(x_o, t)$ which replaces the boundary condition at $x \to \infty$.

It will be shown now how to calculate $C(x, t + \Delta t)$ and $C_b(t + \Delta t)$ given $C(x, t)$ and $C_b(t)$. We choose some value $C(x_o, t+\Delta t)$ slightly higher than $C(x_o, t)$ and obtain $y(x_o, t + \Delta t)$ from Equation (23). Equations (21) and (22) are then integrated backwards from $x = x_o$ to $x = 0$ using the 4th-order Runge-Kutta method to obtain $C(0, t + \Delta t)$ and $y(0, t + \Delta t)$. It is noted that

$$C_b(t + \Delta t) = C(0, t + \Delta t); \quad \left(D\frac{dC}{dx}\right)_{x=0} = y(0, t + \Delta t).$$

Equation (20) is then used in the approximate form,

$$\frac{1}{\Delta t}\big(C(0, t + \Delta t) - C(0, t)\big) = 1 + \frac{A\,D_o}{2\,V\,L}\big(y(0, t + \Delta t) + y(0, t)\big) \tag{24}$$

which gives Δt. The values of $C(x, t_p)$ can be used to calculate the amount of deposit and the void fraction at the end of each reaction period, $t = t_p$, as follows:

$$C_d(x) = C_{do}(x) + m_o\,S(\epsilon_o)\Big[1 - \exp\big(-b\,C(x, t_p)\big)\Big] \tag{25}$$

$$\epsilon(x) = \epsilon_{no}(x) - v_s\,m_o\,S(\epsilon_o)\Big[1 - \exp\big(-b\,C(x, t_p)\big)\Big]. \tag{26}$$

Having obtained the void fraction, $\epsilon(x)$, new profiles of $D_{eff}(x)$ and $r(x)$ are calculated using Equations (8) and (10). The equations are solved for successive cycles until the pore diameter reaches the kinetic diameter of $SiCl_4$ (5.78Å).

5.6 Discussion of Numerical Results

The parameters used in the calculations are listed in Table 5.5. The average initial pore radius was calculated from BET surface area and porosity data supplied by Corning by the formulas of the random capillary model, i.e.,

$$r_o = \sqrt{\frac{1}{-2\pi\lambda}\ln(1-\epsilon_o)}$$

$$S(\epsilon_o) = 4\pi\,\lambda\,(1-\epsilon_o)\,r_o.$$

The molar volume of the deposit, v_s, (in Table 5.5) was estimated from previous thermogravimetric measurements of repeated silylation and hydrolysis until pore plugging [13]. The estimated value was larger than that of amorphous silica because of the highly defective nature of the deposit and the inclusion of a residual volume of trapped voids in the layer. The rate constant of the silylation was estimated by extrapolation from the previous thermogravimetric measurements at 400–500°C [13]. The initial surface density of -OH groups was also estimated from the previous thermogravimetric measurements.

Figure 5.5 shows the calculated deposit density profiles after each cycle versus normalized distance from the boundary, for $SiCl_4$ dosage $0.33\mu mol/cm^2$ and other parameters corresponding to the preparation of Membrane 2 (Table 5.1). The deposit density declines to 10% of its boundary value within $15\mu m$. With the $SiCl_4$ diffusion coefficient and the surface area decreasing with cycle number, the depletion of the reactant slows down, and in the final few cycles the reactant is not fully consumed within the one-minute reaction time. As a result of the decreasing diffusion coefficient, the penetration depth of the reactant gradually decreases, causing the change of curvature observed in Figure 5.5.

Figure 5.6 shows the calculated bulk reactant concentration for selected cycles and for two values of the dosage (0.33μmol/cm^2 and 0.62μmol/cm^2). The reactant is depleted faster for the smaller dosage resulting in a thinner layer. The effect of reactant dosage on the deposit layer thickness is further shown in Figure 5.7. Smaller dosage necessitates a larger number of cycles to reach pore plugging. For the smallest dosage shown in Figure 5.7, the total number of cycles required for pore plugging was 83. As the dosage is further reduced, the extent of silylation at each cycle becomes smaller because of fast exhaustion of the reactant, and the consumption of surface -OH groups is accordingly smaller. In the limit of zero dosage and infinite number of cycles, the concentration of -OH groups is constant, thus the reaction occurs with the initial surface concentration of -OH maintained at all values of x. As that limit is approached, the deposit density profile also reaches a limit as shown in Figure 5.7. This limit represents the thinnest membrane that can be theoretically prepared within the assumptions of the model. Figure 5.8 shows the calculated evolution of N_2 permeance versus the product of dosage and cycle number, i.e., versus the total amount of $SiCl_4$ introduced. As the dosage decreases, the permeance curve tends to a limiting curve corresponding to the limiting density profile.

Figure 5.9 shows the calculated flux for different dosages and the experimental flux for 0.33μmol/cm^2 dosage (Membrane 2). The poor agreement between calculated and experimental curves for the 0.33μmol/cm^2 dosage can be attributed to the drastic assumptions made in the calculation of D_{eff}. These assumptions were:

(i) Uniform pore size distribution

Vycor has a unimodal pore size distribution with mean pore diameter 40Å and upper and lower cutoff points at about 100Å and 20Å, respectively. The

pores have the shape of capillaries with varying cross sections. Replacing the pore size distribution by a single pore size would tend to underpredict the diffusivity. It also explains the calculated steep decrease to zero during the last few cycles, which is at variance with the measured gradual decline. On the other hand, replacing a varying cross section with a uniform cross section would overpredict the diffusion coefficients throughout deposition. A related factor in overpredicting the diffusion coefficient is the decrease of connectivity (generation of open non-conducting pores), not taken into account in the calculations.

(ii) Layer-like growth

If as discussed earlier the deposit growth is cluster-like or tree-like, the decrease of diffusivity at the beginning of deposition would be steeper than if growth was layer-like. The differences between calculated and experimental permeances during the early cycles can be largely attributed to the different modes of deposit growth.

(iii) Knudsen diffusion

The calculations were carried out assuming Knudsen diffusivities (corrected for the size of the diffusing molecule) until the pore diameter reached the kinetic diameter of $SiCl_4$ at which point the pores were regarded "plugged," i.e., completely blocked to flow. However, as the pore diameter declines below 20Å, the Knudsen formula becomes increasingly inaccurate and becomes totally inadequate for pores below 10Å. Using the Knudsen formula throughout deposition would again overpredict the effective diffusivity.

In view of the above uncertainties the calculation of diffusivities and permeance is increasingly in error as the deposition progresses. Figure 5.9, therefore, was included to illustrate the inadequacy of standard diffusion models for the purpose

of predicting the evolution of membrane permeance.

To investigate the effect of the aforementioned assumption (i), we introduced a pore size distribution to the model using three initial pore radii (25Å, 20Å, and 10Å). For simplicity of calculation the parallel pore model was used instead of random capillary model. Figure 5.10 compares the flux calculated using a single pore size (20Å radius) and those calculated using different pore size distributions. The curves calculated for the pore size distributions show more gradual decline during the last few cycles, as observed experimentally. On the other hand, the slow decline during the early cycles is still at variance with the experimental steeper decline. The steeper experimental decline during the early cycles could be attributed to the varying cross section of individual pores and to the cluster-like growth of the deposit. To explore the first effect calculations were performed treating each pore as two in-series sections of different initial diameters. The flux calculated with this modified pore geometry featured a steeper decline in the early cycles, but was in poor agreement with the later part of the experimental curves.

Figure 5.11 shows the effect of the initial -OH concentration on the deposit profile. Higher initial concentrations of -OH increase the reaction rate and thus decrease the penetration depth and the number of cycles to complete pore plugging. To maintain the initial -OH groups at as high a level as possible, it is important to limit the length and temperature of pretreatment preceding membrane deposition.

5.7 Conclusions

Hydrogen permselective silica membranes were deposited on porous Vycor tubes by a series of alternating reactions with $SiCl_4$ and H_2O. As the $SiCl_4$ dosage in each cycle was decreased, the number of cycles required for membrane

formation increased and the membrane permeance increased. The permeance improvement diminishes and becomes insignificant for $SiCl_4$ dosage below about 10 μmol/cm^2. Upon prolonged hydrothermal treatment the membrane permeance decreased about 20–30%. Comparison of the membranes prepared by alternating deposition with those prepared in our earlier work by one-sided deposition revealed the following differences. Immediately after deposition both types of membranes have approximately the same permeance. Upon prolonged hydrothermal treatment, however, the membranes prepared by alternating deposition suffer much smaller decline in permeance (20–30% vs. 70–80%) and have better H_2:N_2 selectivity. These results strongly suggest that the membranes prepared by alternating deposition are thinner and initially denser. Both types of membranes reach approximately equal densities after prolonged hydrothermal treatment. The smaller thickness of the membranes prepared by alternating deposition is mainly due to the elimination of axial reactant concentration gradients and gas-phase particle formation both of which result in thicker deposit layers.

Nomenclature

A External surface area of support tube, cm^2

b A parameter abbreviation for $k\,C_{bo}$, min^{-1}

C A variable defined in transformation of equations, min

c Dimensionless variable for $SiCl_4$ concentration in porous medium

c_b Dimensionless variable for bulk $SiCl_4$ concentration in gas phase

C_{bo} Initial concentration of bulk $SiCl_4$ concentration in gas phase, mol/cm^3

C_d Concentration of SiO_2 deposit, mol/cm^3

C_g Concentration of bulk $SiCl_4$ concentration in gas phase, mol/cm^3

C_{oh} Concentration of -OH groups in porous medium, mol/cm^3

C_{si} Concentration of $SiCl_4$ in porous medium, mol/cm^3

D Dimensionless variable for $SiCl_4$ diffusivity in porous medium

D_{eff} Diffusion coefficient of $SiCl_4$ in porous medium, cm^2/min

k Reaction rate constant for silylation reaction, $cm^3/(min{\cdot}mol)$

L Thickness of the support tube wall, cm

M Molecular weight of $SiCl_4$, g/mol

m_o Concentration of initial -OH per unit surface area, mol/cm^2

R Gas constant, erg/(mol·K)

r Average local pore radius, cm

S Surface area of porous Vycor per unit total volume, cm^2/cm^3

s Dimensionless variable for concentration of -OH groups

t Time, min

t_p Time period for one reaction cycle, min

V Volume of the reactor, cm^3

v_s Molar volume of SiO_2 deposit, cm^3/mol

x Dimensionless variable for distance in Vycor wall

y A variable defined as $D\frac{dC}{dx}$, min

z Distance in Vycor wall cross section, cm

ϵ Void fraction

λ Probability density function characterizing the porous medium (in random capillary model)

Φ Thiele modulus

σ Dimensionless surface area, $\frac{S(\epsilon)}{S(\epsilon_o)}$

τ Empirical tortuosity factor

Acknowledgement

The authors appreciate the funding of this work by the Department of Energy under the University Coal Research Program, Grant DE-FG22-92PC92525. Corning Inc. graciously donated the porous Vycor tubes.

References

1. Sun, Y. M. and S. J. Khang, "Catalytic Membrane for Simultaneous Chemical Reaction and Separation Applied to a Dehydrogenation Reaction," *Ind. Eng. Chem. Res.*, **27**, 1136 (1988).

2. Armor, J. N., "Catalysis with Permselective Inorganic Membranes," *Applied Catalysis*, **49**, 1 (1989).

3. Kameyama, T., M. Dokiya, M. Fujushige, H. Yokokawa, and K. Fukuda, "Possibility for Effective Production of Hydrogen from Hydrogen Sulfide by Means of a Porous Vycor Glass Membrane," *Ind. Eng. Chem. Fundam.*, **20**, 97 (1981).

4. Mohan, K. and R. Govind, "Analysis of Equilibrium Shift in Isothermal Reactors with a Permselective Wall," *AIChE J.*, **34**, 1493 (1988).

5. Raymont, M. E. D., "Make Hydrogen from Hydrogen Sulfide," *Hydrocarb. Process.*, **54 (7)**, 139 (1975).

6. Shelby, J. E., Molecular Solubility and Diffusion, *Treatise of Materials Science and Technology*, Vol. 17, Academic Press, New York (1979).

7. Altemose, V. O., "Permeation of Gases in Glass," *Seventh Symposium on the Art of Glassblowing*, The American Scientific Glassblowers Society, Wilmington, Del. (1962).

8. Brinker, C. J., "Structure of Sol-Gel-Derived Glasses," *Glass Science and*

Technology Vol. 4A, p. 169, Academic Press, New York (1990).

9. Yoldas, B. E., "Alumina Gels that Form Porous Transparent Al_2O_3," *J. Mat. Sci.*, **10**, 1856 (1975).

10. Tsapatsis, M., S. Kim, S. W. Nam, and G. R. Gavalas, "Synthesis of H_2 Permselective SiO_2, $TiCl_4$, Al_2O_3, and B_2O_3 Membranes From the Chloride Precursors," *Ind. Eng. Chem. Res.*, **30**, 2152 (1991).

11. Megiris, C. E. and J. H. E. Glezer, "Preparation of Silicon Dioxide Films by Low-Pressure Chemical Vapor Deposition on Dense and Porous Alumina Substrates," *Chem. Eng. Sci.*, **47**, 3925 (1992).

12. Ha, H. Y., S. W. Nam, S. A. Hong, and W. K. Lee, "Chemical Vapor Deposition of Hydrogen Permselective Silica Films on Porous Glass Supports from Tetraethylorthosilicate," *J. Membr. Sci.*, in press (1993).

13. Kim, S. and G. R. Gavalas, "Kinetic Study of the Reactions of Chlorosilanes with Porous Vycor Glass," *J. Colloid and interface Sci.*, **161**, 6 (1993).

14. Tsapatsis, M. and G. R. Gavalas, "Structure and Aging Characteristics of H_2 Permselective SiO_2-Vycor Membranes," *J. Membrane Sci.*, accepted (1993).

15. Ritala, M., M. Leskelä, E. Nykänen, P. Soininen, and L. Niinistö, "Growth of Titanium Dioxide Thin Films by Atomic Layer Epitaxy," *Thin Solid Films*, **225**, 288 (1993).

16. Suntola, T. and Simpson, M., *Atomic Layer Epitaxy* p. 1, Blackie, Glasgow

(1990).

17. Usui, A., "Study of Self-limiting Growth Mechanism in Chloride ALE," *Thin Solid Films*, **225**, 53 (1993).

18. Nam, S. W. and G. R. Gavalas, "Stability of H_2 Permselective SiO_2 Films Formed by Chemical Vapor Deposition," *AIChE Symp. Ser.*, **85**, 68 (1989).

19. Kern, W., "Densification of Vapor-Deposited Phosphosilicate Glass Films," *RCA Review*, **37 (3)**, 55 (1976).

20. Welty, J. R., C. E. Wicks, and R. E. Wilson, *Fundamentals of Momentum, Heat, and Mass Transfer* p. 600, John Wiley & Sons, New York (1983).

21. Gavalas, G. R., "A Random Capillary Model with Application to Char Gasification at Chemically Controlled Rates," *AIChE J.*, **26**, 577 (1980).

22. Prausnitz, J. M., R. N. Lichtenthaler, and E. G. de Azevedo, *Molecular Thermodynamics of Fluid-Phase Equilibria* p. 85, Prentice-Hall Inc., Englewood Cliffs, N. J. (1986).

23. Del Borghi, M., J. C. Dunn, and K. B. Bischoff, "A Technique for Solution of the Equations for Fluid Solid Reactions with Diffusion," *Chem. Eng. Sci.*, **31**, 1065 (1976).

Appendix: Calculation of the permeance of deposit layer excluding the resistance of Vycor tube.

The tube cross section is regarded to comprise two resistances in series, that of the deposit layer of nominal thickness δ, and that of the free-of-deposit support tube defined by $r_i \leq r < r_o - \delta$ for outside deposit and $r_i + \delta < r \leq r_o$ for inside deposit. The nominal thickness δ is used only in the calculation of the support resistance thus is not very important since $\delta \sim 10\,\mu$m while $r_o - r_i = 1100\,\mu$m. Having taken the two resistances in series, we have the flux,

$$N = K\,\Delta C = \left(D_{eff}\,\frac{dC}{dr} \right) \tag{A1}$$

where K is the permeance of the gas in the deposit layer, C is the concentration of the gas, and D_{eff} is the effective diffusivity of the gas in the Vycor tube.

The flowrate of the gas in the membrane, F, is then

$$F = 2\,\pi\,r\,l \left(D_{eff}\,\frac{dC}{dr} \right) \tag{A2}$$

where l is the length of the membrane tube.

When the deposit layer is on the outside surface as shown in Figure 5.12a, separating variables and integrating Equation (A2) from r_i to $r_o - \delta$ gives

$$F = \frac{2\,\pi\,l\,D_{eff}(C_2 - C_3)}{\ln\left(\frac{r_o - \delta}{r_i}\right)}. \tag{A3}$$

From Equation (A1) we also have

$$F = 2\,\pi\,l\,(r_o - \delta)\,K\,(C_1 - C_2). \tag{A4}$$

Equations (A3) and (A4) can be combined to obtain

$$C_2 = \frac{\frac{2\,\pi\,l\,D_{eff}\,C_3}{\ln(\frac{r_o-\delta}{r_i})} + 2\,\pi\,l\,(r_o-\delta)\,K\,C_1}{\frac{2\,\pi\,l\,D_{eff}}{\ln(\frac{r_o-\delta}{r_i})} + 2\,\pi\,l\,(r_o-\delta)\,K}. \qquad (A5)$$

When C_2 is substituted in the expression for F in Equation (A4) there is obtained

$$F = \frac{2\,\pi\,l\,(r_o-\delta)(C_1-C_3)}{\frac{1}{K} + \frac{(r_o-\delta)\,\ln(\frac{r_o-\delta}{r_i})}{D_{eff}}}. \qquad (A6)$$

Equation (A6) gives the flowrate in terms of two resistances, the resistance of Vycor tube, R_v, and the resistance of the deposit layer, R_d, where

$$R_v = \frac{(r_o-\delta)\,\ln(\frac{r_o-\delta}{r_i})}{D_{eff}} \qquad (A7)$$

and

$$R_d = \frac{1}{K}. \qquad (A8)$$

Based on the measured values of the flowrate the overall permeance, P, is given by

$$P = \frac{F}{2\,\pi\,l\,(r_o-\delta)\,(C_1-C_3)}. \qquad (A9)$$

When the deposit layer is on the inside surface as shown in Figure 5.12b, integration of Equation (A2) from $r_i+\delta$ to r_o gives

$$F = \frac{2\,\pi\,l\,D_{eff}(C_2-C_3)}{\ln(\frac{r_o}{r_i+\delta})}. \qquad (A10)$$

Again from Equation (A1) we obtain

$$F = 2\,\pi\,l\,(r_i+\delta)\,K\,(C_1-C_2) \qquad (A11)$$

so that combining (A10) and (A11) gives

$$C_2 = \frac{\frac{2\,\pi\,l\,D_{eff}\,C_3}{\ln(\frac{r_o}{r_i+\delta})} + 2\,\pi\,l\,(r_i+\delta)\,K\,C_1}{\frac{2\,\pi\,l\,D_{eff}}{\ln(\frac{r_o}{r_i+\delta})} + 2\,\pi\,l\,(r_i+\delta)\,K}. \qquad (A12)$$

Substituting C_2 in Equation (A11) gives

$$F = \frac{2\,\pi\,l\,(r_i+\delta)(C_1 - C_3)}{\frac{1}{K} + \frac{(r_i+\delta)\,\ln(\frac{r_o}{r_i+\delta})}{D_{eff}}} \qquad (A13)$$

so that

$$R_v = \frac{(r_i+\delta)\,\ln(\frac{r_o}{r_i+\delta})}{D_{eff}}. \qquad (A14)$$

The overall permeance, P, is given by

$$P = \frac{F}{2\,\pi\,l\,(r_i+\delta)\,(C_1 - C_3)}. \qquad (A15)$$

For both of the above cases, the permeance of the deposit layer is given as

$$K = \frac{1}{1/P - R_v} \qquad (A16)$$

where R_v is also the inverse of the gas permeance either at the inner or outer radius in untreated Vycor tube.

Table 5.1 Membrane permeance to H_2 and N_2 after deposition and after hydrothermal treatment by flow of 10% H_2O-N_2 at atmospheric pressure and 700°C for one day. The $SiCl_4$ dosage per cycle was 0.62μmol/cm^2 for Membrane 1 and 0.33μmol/cm^2 for Membrane 2.

	Permeance at 700°C (cm^3(STP)/min atm cm^2)			
	After final cycle		After H_2O treatment	
	N_2	H_2	N_2	H_2
Membrane 1	0.00317	0.283	0.0018	0.278
Membrane 2	0.00089	0.313	0.00042	0.288

Table 5.2a Permeance of membranes deposited on the inner surface before and after hydrothermal treatments. The dosage of $SiCl_4$ per cycle was 0.28 μmol/cm^2.

			Permeance (cm^3(STP)/min atm cm^2)							
	Reaction T (°C)	Measure-ment T (°C)	after Deposition		after Treatment 1		after Treatment 2		after Treatment 3	
			N_2	H_2	N_2	H_2	N_2	H_2	N_2	H_2
Membrane 3	700	700	0.0039	0.38	0.0011	0.37	0.00049	0.34	0.00042	0.33
		600	0.0036	0.37	0.00073	0.35	0.00021	0.31	0.00015	0.30
		450	0.0019	0.33	0.00041	0.29	0.00016	0.23	0.000094	0.21
Membrane 4	800	800	0.0013	0.37	0.00099	0.37	0.00053	0.34	0.00033	0.34
		600	0.00046	0.34	0.00038	0.33	0.00025	0.30	0.00018	0.28
		450	0.00020	0.28	0.00026	0.27	0.00018	0.20	0.00015	0.19

Treatment 1: 5 days at 550°C under 7 atm N_2 and 3 atm H_2O.
Treatment 2: 10 days at 550°C under 7 atm N_2 and 3 atm H_2O.
Treatment 3: 15 days at 550°C under 7 atm N_2 and 3 atm H_2O.

Table 5.2b Permeance of membranes[1] produced by one-sided (simultaneous flow) deposition before and after hydrothermal treatments.

Reaction T (°C)	Measure-ment T (°C)	Permeance (cm^3(STP)/min atm cm^2) After Deposition[2] N_2	H_2	After Treatment 1 N_2	H_2	After Treatment 2 N_2	H_2	After Treatment 3 N_2	H_2
750	750	0.002	0.40						
	600			0.006	0.25	0.0001	0.12	0.0001	0.11

[1]Selected data from Table I in (Tsapatsis and Gavalas, 1993).

[2]Deposition by continuous flow of 0.027atm $SiCl_4$ and 0.13atm H_2O for 5 minutes.

Treatment 1: 2 days at 550°C under 7 atm N_2 and 3 atm H_2O.

Treatment 2: 9 days at 500°C under 7 atm N_2 and 3 atm H_2O.

Treatment 3: 21days at 500°C under 7 atm N_2 and 3 atm H_2O.

Table 5.3 The permeance of deposit layers excluding the resistance of Vycor tube. The $SiCl_4$ dosage per cycle was 0.28μmol/cm^2.

			Permeance (cm^3(STP)/min atm cm^2)							
	Reaction T (°C)	Measure-ment T (°C)	after Deposition		after Treatment 1		after Treatment 2		after Treatment 3	
			N_2	H_2	N_2	H_2	N_2	H_2	N_2	H_2
Membrane 3	700	700	0.0041	1.74	0.0012	1.57	0.00049	1.15	0.00042	1.04
		600	0.0037	1.33	0.00074	1.13	0.00021	0.76	0.00015	0.70
		450	0.0019	0.82	0.00041	0.62	0.00016	0.40	0.000094	0.34
Membrane 4	800	800	0.0013	1.65	0.00099	1.58	0.00053	1.18	0.00033	1.16
		600	0.00046	0.99	0.00038	0.93	0.00025	0.72	0.00018	0.63
		450	0.00020	0.56	0.00026	0.51	0.00018	0.32	0.00015	0.29

Treatment 1: 5 days at 550°C under 7 atm N_2 and 3 atm H_2O.
Treatment 2: 10 days at 550°C under 7 atm N_2 and 3 atm H_2O.
Treatment 3: 15 days at 550°C under 7 atm N_2 and 3 atm H_2O.

Table 5.4 Activation energy for H_2 permeance of Membranes 3 and 4 before and after hydrothermal treatments (in kJ/mol).

	After Deposition	After Treatment 1	After Treatment 2	After Treatment 3
Membrane 3	17.3	21.5	24.6	25.8
Membrane 4	20.1	20.8	24.5	25.8

Treatment 1: 5 days at 550°C under 7 atm N_2 and 3 atm H_2O.
Treatment 2: 10 days at 550°C under 7 atm N_2 and 3 atm H_2O.
Treatment 3: 15 days at 550°C under 7 atm N_2 and 3 atm H_2O.

Table 5.5 Parameters used in the calculations.

$D_{eff}(\varepsilon_o) = 2.32 \times 10^{-2}$ cm^2/min	$C_{bo} = 8.77 \times 10^{-7}$ mol/cm^3
$k = 3.7 \times 10^{8}$ cm^3/mol min	$v_s = 49.2$ cm^3/mol
$m_o = 1.6 \times 10^{-10}$ mol/cm^2	$V = 12.5$ cm^3
$S(\varepsilon_o) = 3.0 \times 10^{6}$ cm^2/cm^3	$A = 33.0$ cm^2
$L = 0.11$ cm	$\varepsilon_o = 0.3$
Dosage = 0.33μmol/cm^2	$r_o = 16.65$ Å

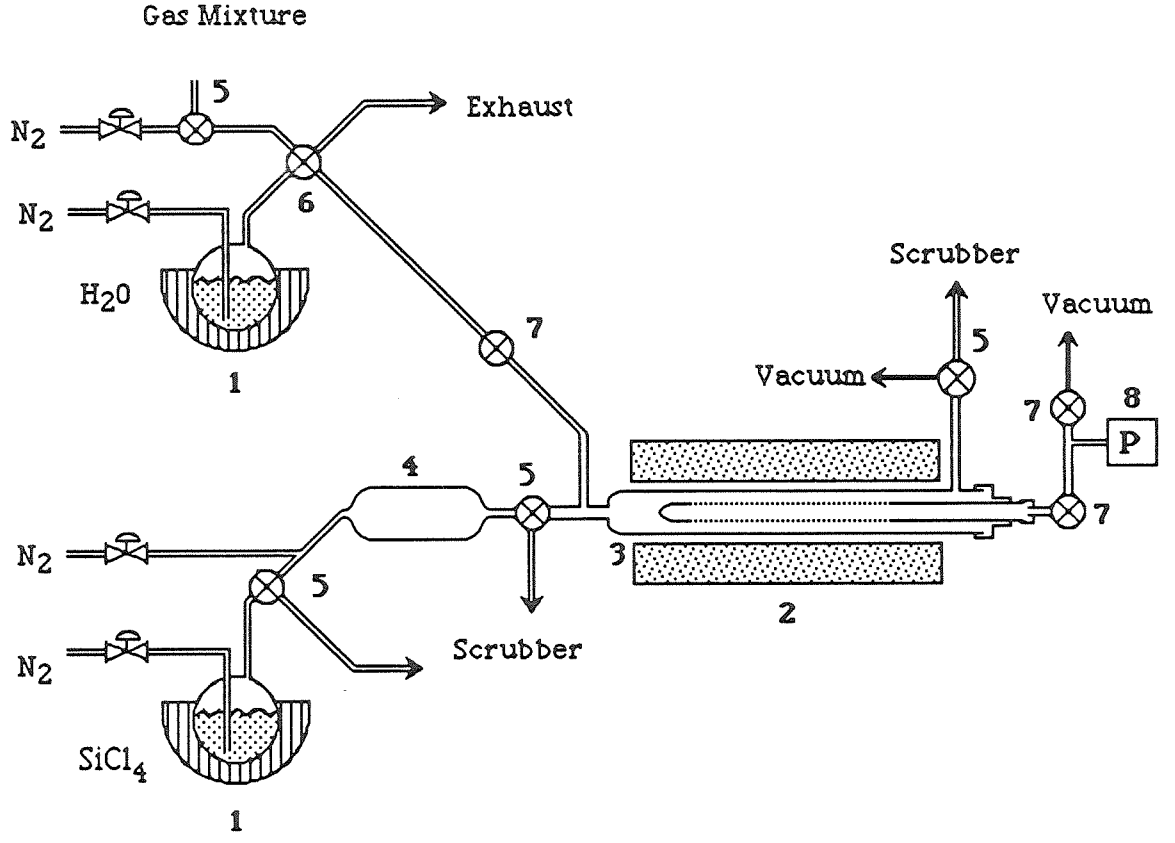

Figure 5.1 Schematic diagram of the reactor system. 1, bubbler with heating element and temperature controller; 2, furnace with temperature controller; 3, quartz tube reactor; 4, fixed volume gas collection bulb; 5, 3-way valve; 6, 4-way valve; 7, on-off valve; 8, pressure transducer connected to microcomputer.

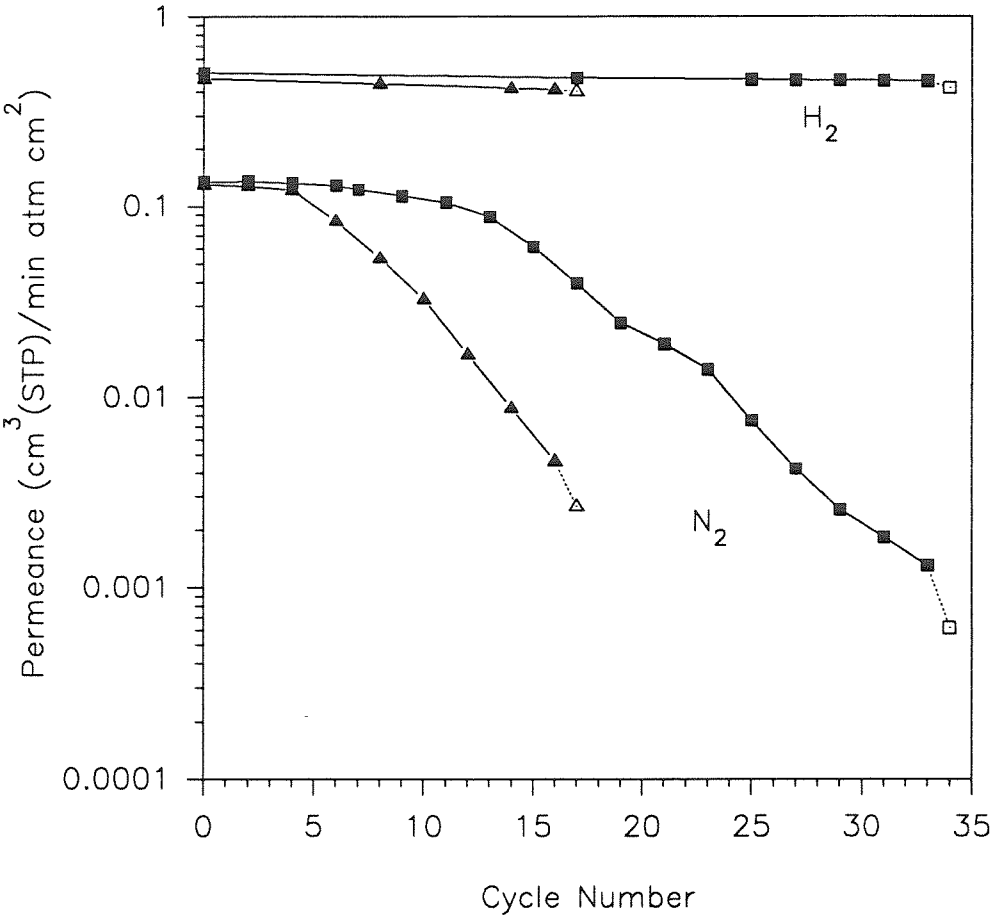

Figure 5.2 Permeance of H_2 and N_2 versus cycle number at 700°Cfor $SiCl_4$ dosage of 0.62μmol/cm^2 for Membrane 1 (▲) and 0.33μmol/cm^2 for Membrane 2 (■). (△) and (□) indicate the permeance changes after 1 day of hydrothermal treatment at 700°C under 0.1 atm H_2O and 1 atm of N_2.

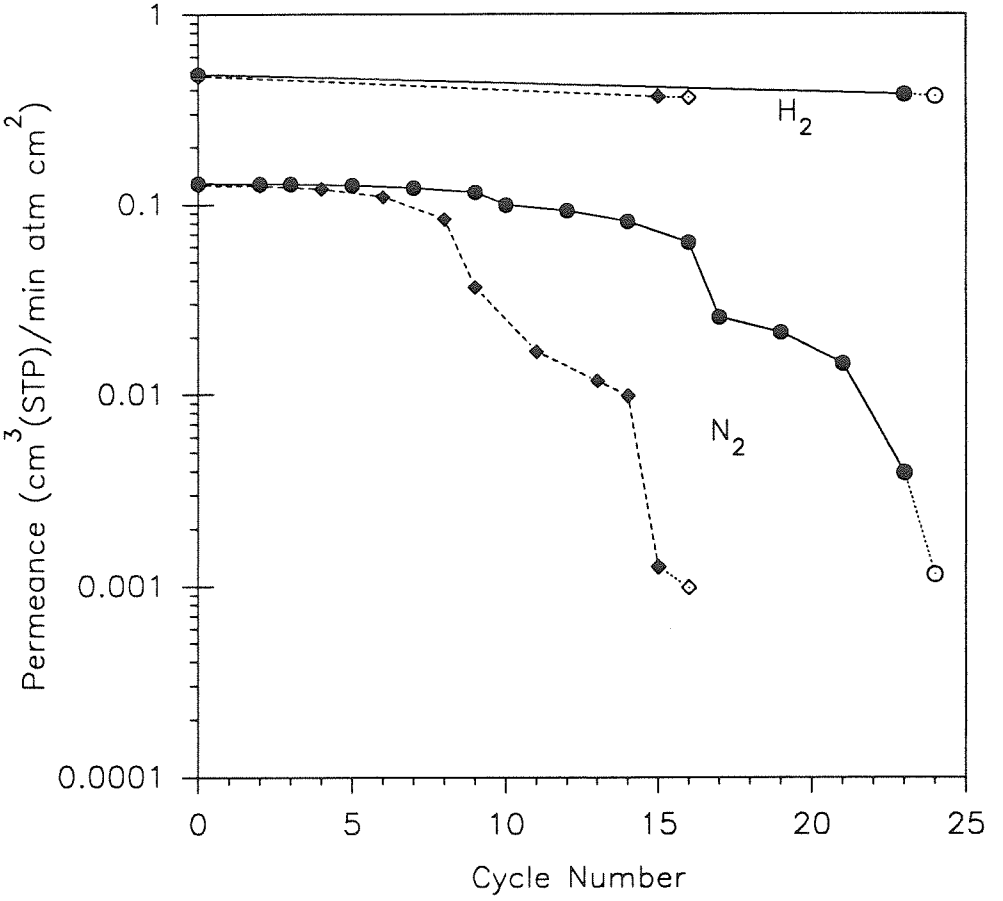

Figure 5.3 Permeance of H_2 and N_2 versus cycle number for the reaction at 700°C (Membrane 3, •) and 800°C (Membrane 4, ◆) for $SiCl_4$ dosage of 0.28μmol/cm^2 per cycle. (◇) and (○) indicate the permeance changes after 5 days of hydrothermal treatment at 550°C under 3 atm H_2O and 7 atm of N_2.

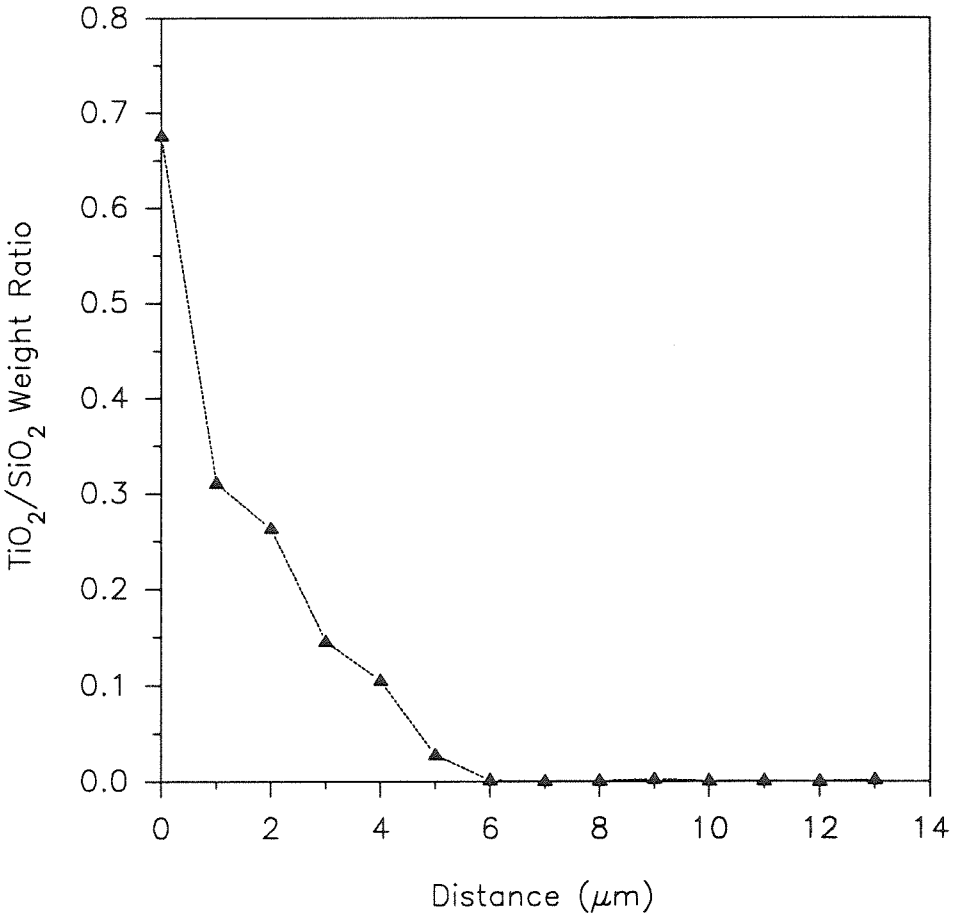

Figure 5.4 EMA linescan of a tube cross section containing TiO_2 layers deposited at 700°C using $TiCl_4$ dosage of $0.37\mu mol/cm^2$ per cycle.

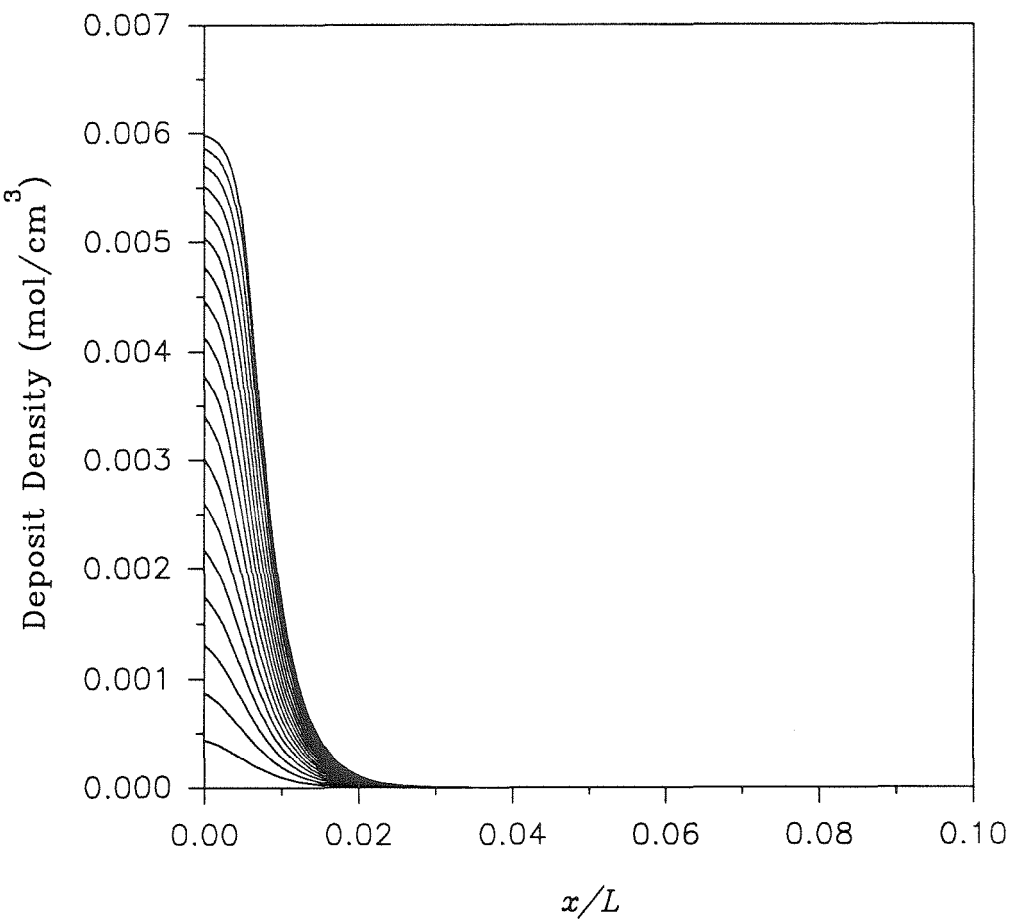

Figure 5.5 Calculated deposit density profiles after each cycle of deposition at 700°C. The $SiCl_4$ dosage was $0.33\mu mol/cm^2$ per cycle.

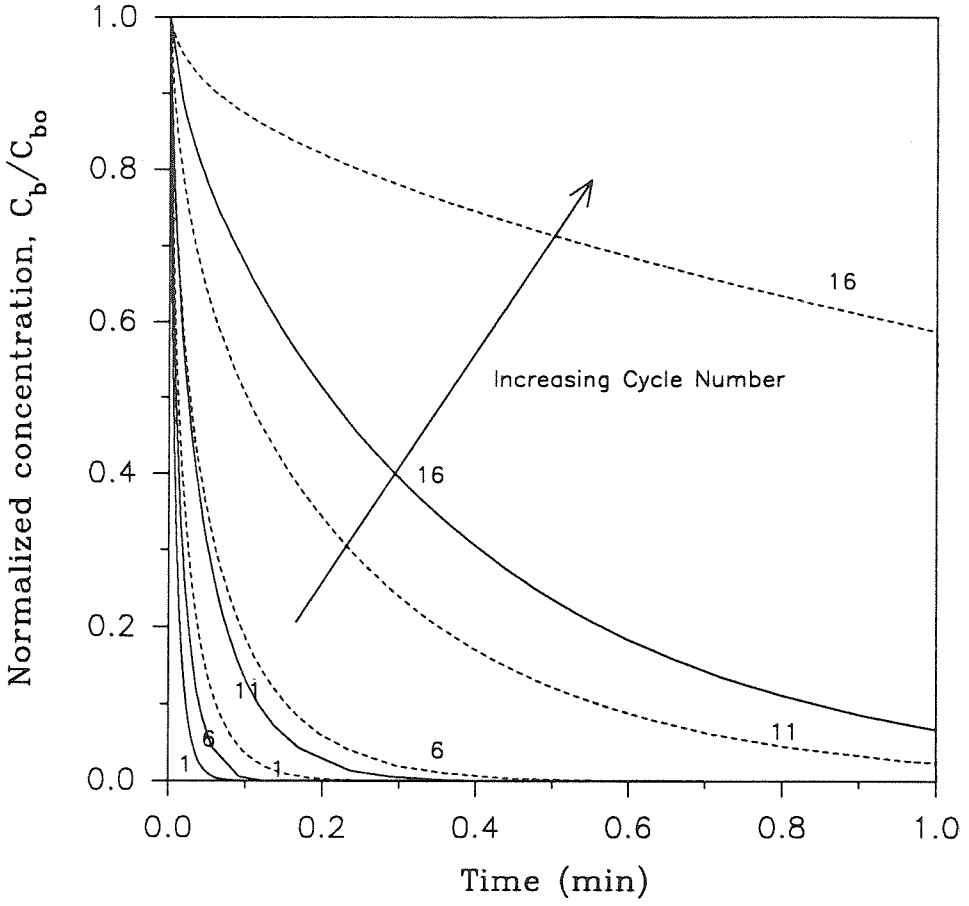

Figure 5.6 Calculated bulk $SiCl_4$ concentration, C_g/C_{bo}, versus reaction time in selected cycles for $SiCl_4$ dosage of $0.33\mu mol/cm^2$ (—) and $0.62\mu mol/cm^2$ (- - -).

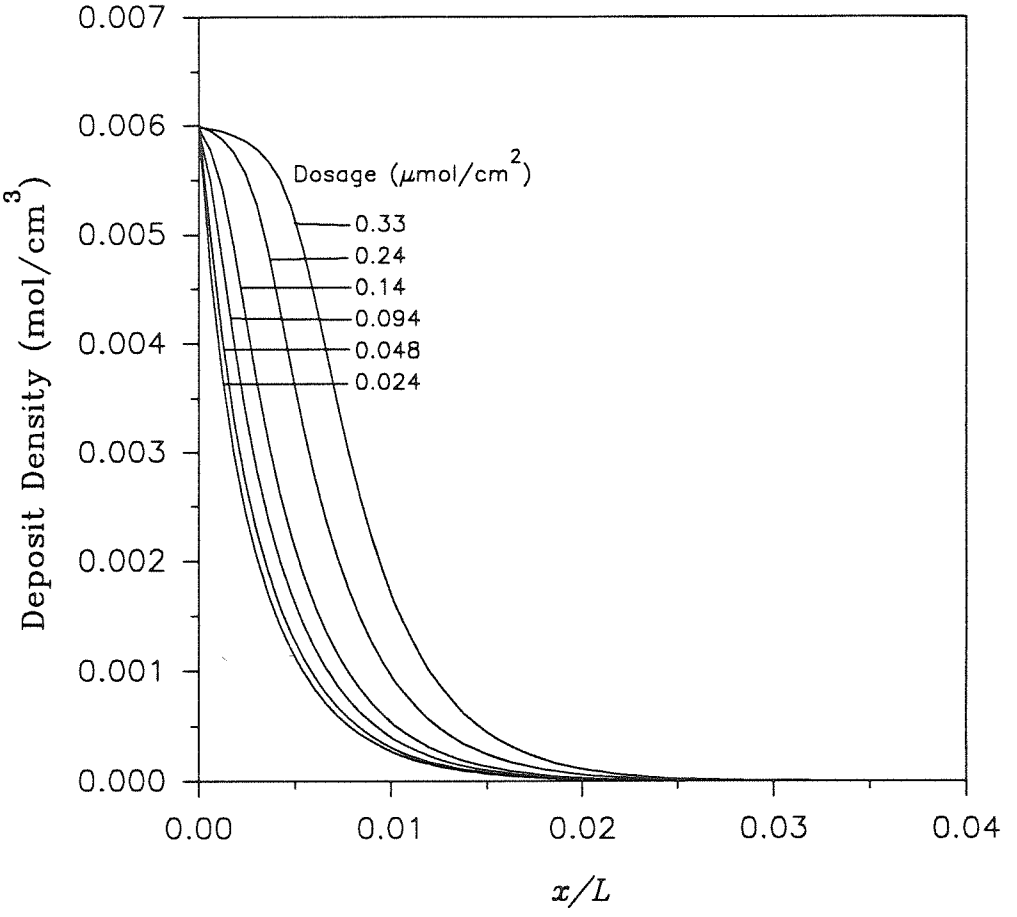

Figure 5.7 Calculated final deposit density profiles for different $SiCl_4$ dosages.

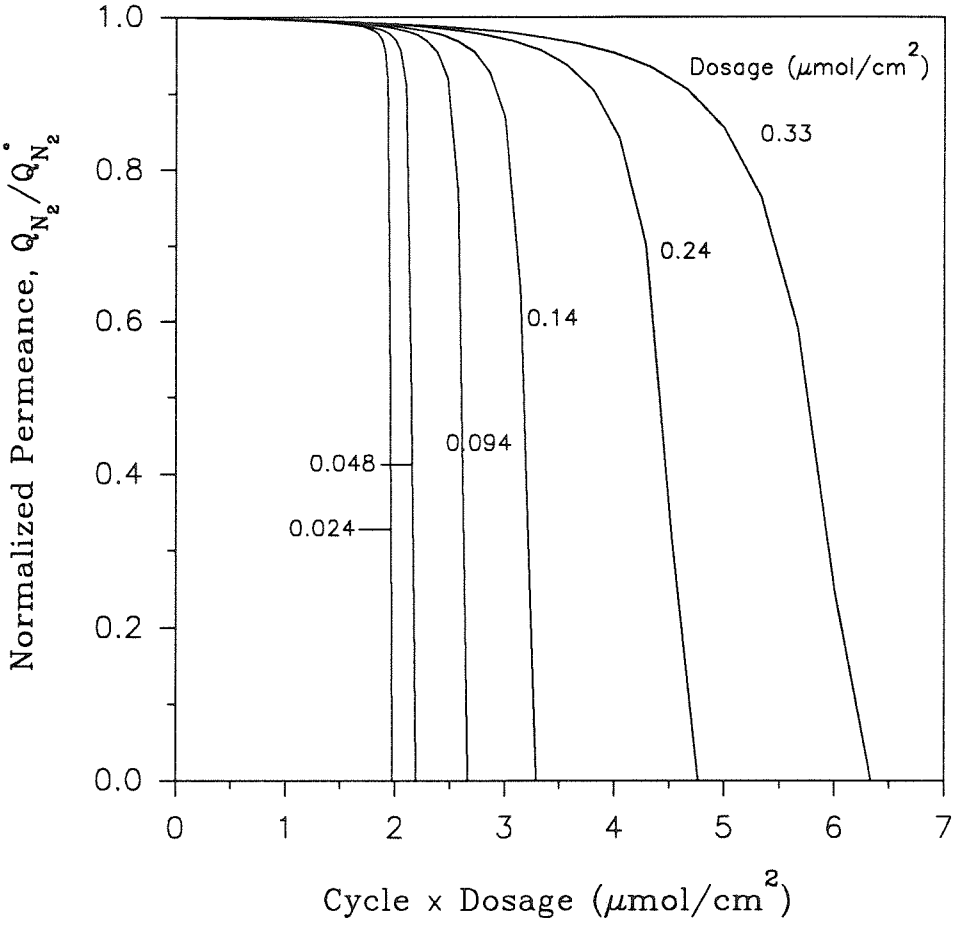

Figure 5.8 Calculated permeance versus cumulative dosage of $SiCl_4$.

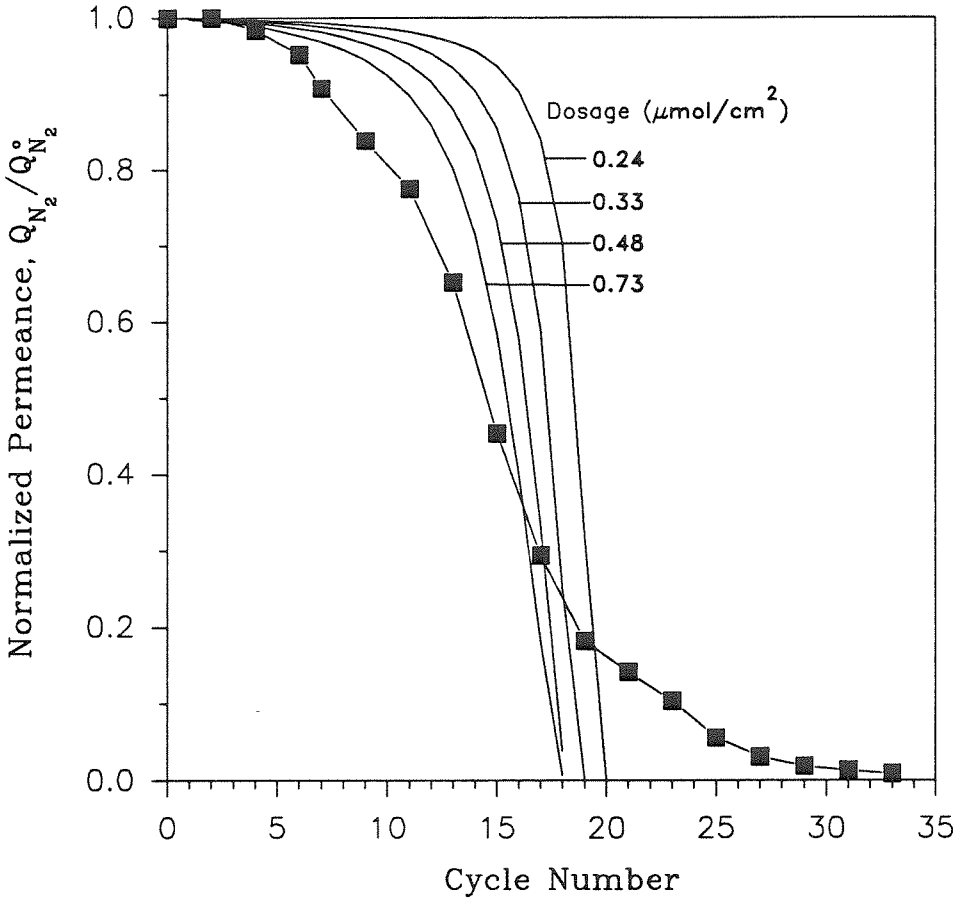

Figure 5.9 Calculated permeance versus cycle number for different $SiCl_4$ dosages (—). The full squares (▪) show the experimental permeance obtained using $SiCl_4$ dosage of 0.33 μmol/cm^2 per cycle.

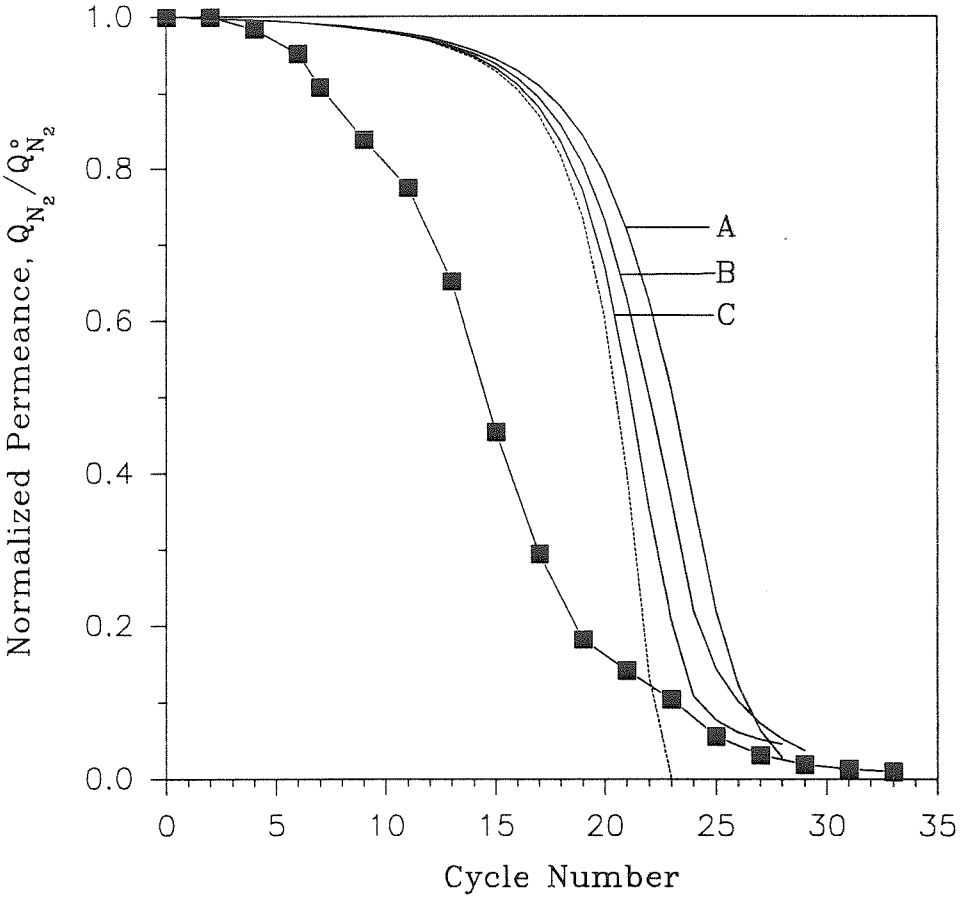

Figure 5.10 Calculated permeance versus cycle number for $SiCl_4$ dosage of 0.33 μmol/cm^2 and for different pore size distributions. (- - -) : single pore size (20Å in radius, void fraction 0.3); Curves A, B, and C : pore size distributions with radii 25Å, 20Å, and 10Å and void fractions 0.083, 0.20, 0.017 (A), 0.042, 0.25, 0.008 (B), and 0.017, 0.28, 0.003 (C). The full squares (■) show the experimental permeance obtained using $SiCl_4$ dosage of 0.33 μmol/cm^2 per cycle.

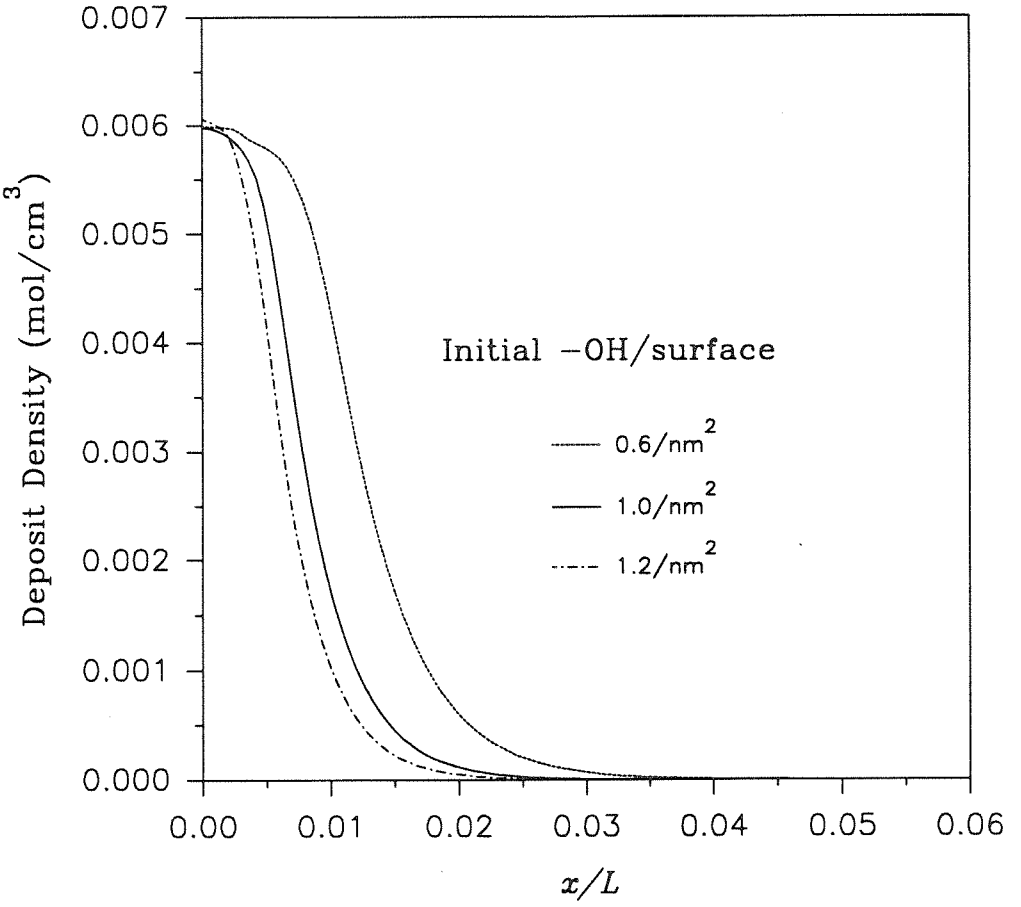

Figure 5.11 Calculated deposit density profiles for various initial surface concentrations of -OH groups.

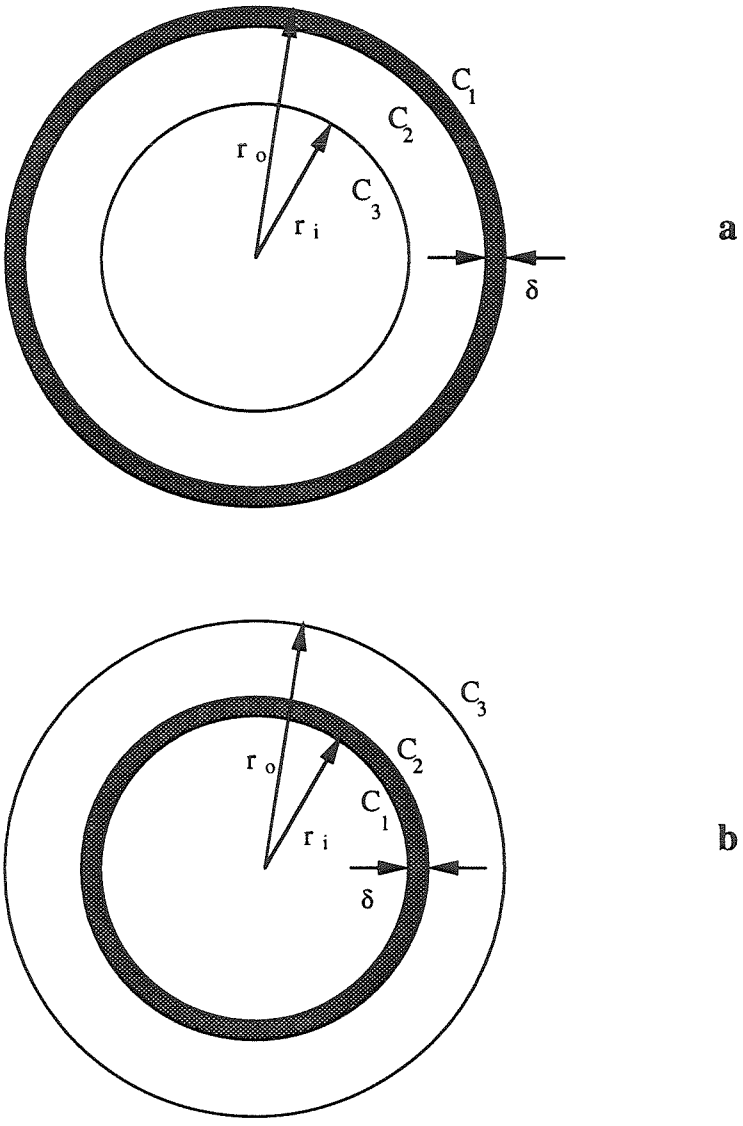

Figure 5.12 Cross section of Vycor tube wall containing a deposit layer (a) on the outside surface and (b) on the inside surface.

Chapter VI

Conclusions

Thin oxide layers supported on porous Vycor tubes can be prepared by chemical vapor deposition using the reactants $SiCl_4$ or $TiCl_4$ and H_2O. The reactants can be passed either through the bore of the support tube (one-sided geometry) or separately through the bore and around the outside surface of the support tube (opposing-reactants geometry). The oxide layer constricts the pores and forms a composite membrane permselective to hydrogen. The silica membranes can be prepared in both the one-sided and opposing-reactants geometry at 600–800°C, while TiO_2 membranes can be prepared only in the opposing-reactants geometry at 200–600°C.

The SiO_2membranes prepared in the one-sided geometry has thinner deposit layer, and thus higher H_2 permeance than other membranes prepared in the opposing-reactants geometry on account of a more favorable balance between reaction and diffusion. The H_2 permeance of the SiO_2 membranes is approximately 0.3 $cm^3(STP)/(min\cdot\ cm^2\cdot\ atm)$ at 450°C, and the H_2:N_2 selectivity is 500–5000.

Characterization of the TiO_2 membranes by electron microprobe analysis shows the deposit density profiles in the tube cross sections. The spatial density distribution of the TiO_2 layer deposited in the opposing-reactants geometry at 450°C and 600°C shows an asymmetric profile located close to the side of chloride flow. The profile has a thin region (in the order of 1 μm in thickness) of maximum density with a gradual decrease to the chloride side and a sharp decrease to the water side. The TiO_2 layer produced at 200°C has more symmetric feature of the density profile. The membrane selectivity is obtained only in the thin region of totally plugged pores. The broad region of partially filled pores does not contribute to the selectivity but reduces the permeance somewhat. The activation energy for H_2 permeance is greater for the membrane prepared at higher temperature due to

the denser deposit layer. Upon prolonged hydrothermal treatment the membrane permeance and selectivity decrease due to densification of the TiO_2 deposit. Annealing of the membranes at 800°C drastically decreases the H_2 permeance and selectivity because of the phase transformation of amorphous TiO_2 to anatase.

The oxide deposition takes place by a heterogeneous mechanism involving reaction of gaseous chloride and surface hydroxyl groups and reaction of water molecules with surface chloride groups on the growing deposit layer. In silica deposition, the reaction between $SiCl_4$ and surface -OH groups occurs very rapidly. In addition to the silylation of surface hydroxyl groups and subsequent hydrolysis of chloride groups, condensations between a surface chloride and a hydroxyl group and between two hydroxyl groups, proceeding more slowly, contribute to the overall deposition process. The surface hydroxyl groups can be approximately classified as isolated or paired. A kinetic model postulating two types of silanols and incorporating the silylation, hydrolysis and condensation steps gives good agreement with the TGA data. However, the classification of silanols into two groups is viewed as a drastic approximation appropriate to the limited data available.

Due to the rapid reaction of the chlorosilanes with surface hydroxyls at temperatures above 600°C the fast depletion of $SiCl_4$ causes significant axial concentration gradients in the one-sided flow deposition, resulting in nonuniform deposit layer along the length of the tube. The axial concentration gradients are eliminated using the atomic layer epitaxy method modified to control the reactant dosage. A series of alternating reactions with $SiCl_4$ and H_2O can be used to deposit thin silica layers on porous Vycor tubes. The membranes prepared by this technique have H_2 permeance of 0.3–0.4 $cm^3(STP)/(min \cdot cm^2 \cdot atm)$ and H_2:N_2 selectivity of 500–1000 at 600°C. As the $SiCl_4$ dosage in each cycle is decreased,

the number of cycles required for membrane formation increases, and the membrane permeance increases. The permeance improvement diminishes and becomes insignificant for $SiCl_4$ dosage below about 10 μmol/cm^2. The membranes are more stable to long hydrothermal treatments than those prepared by one-sided deposition; the membranes suffer much smaller decline in permeance and have better H_2:N_2 selectivity. The membranes prepared by alternating deposition seem to be thinner and initially denser. The smaller thickness of the membranes prepared by alternating deposition is mainly due to the elimination of axial reactant concentration gradients and gas-phase particle formation both of which result in thicker deposit layers. A simple model incorporating reactant diffusion and surface reaction kinetics is used to study the effect of various parameters on the formation of the deposit layer. The model provides a qualitative understanding of the effect of dosage and other parameters, however, due to the pore size distribution of Vycor glass, complicated pore geometry created by irregular mode of deposit growth, and inadequacy of standard diffusion models to predict diffusion coefficients in micropores, the model provides limited information about the evolution of membrane permeance.